# Narrowband photon pairs for atoms: High resolution spectral engineering and characterisation

DISSERTATION

Submitted for the degree of
Doctor of Philosophy
by
Vindhiya Prakash

Thesis Advisor: Prof. Dr. Morgan W. Mitchell

ICFO - The Institute of Photonic Sciences
UPC - Universitat Politècnica de Catalunya

November, 2021

Thesis Examiners:

Prof. Dr. Christian Kurtsiefer, Centre for Quantum Technologies, Singapore.

Prof. Dr. Hugues de Riedmatten, ICFO - The Institute of Photonic Sciences, Castelldefels.

Dr. Fabian Steinlechner, Abbe Center of Photonics, Jena.

*To*

*Amma & Appa*
*The "Lalithalaya siblings"*
*Ammamma, Mama & Mami*

ज्योतिषामपि तज्ज्योतिस्तमसः परमुच्यते।
ज्ञानं ज्ञेयं ज्ञानगम्यं हृदि सर्वस्य विष्ठितम्॥

***It is the source of light in all luminous objects.***
***It is beyond the material darkness and is unmanifested.***
***It is knowledge, It is the object of knowledge,***
***and It is the goal of knowledge.***
***It is situated at the heart of everything.***

– Bhagavad Gita 13.18, 1st M. BCE

# ABSTRACT

This thesis describes experimental work to generate and characterise single photons and photon pairs, with frequency content suitable for controlled interaction with cold rubidium atoms. We describe a photon-pair source, consisting of a cavity-enhanced spontaneous parametric down-conversion (CE-SPDC) system, followed by Fabry-Perot interferometer (FPI) filters, that produces narrowband photon pairs that have a bandwidth of $\approx 5$ MHz. Both photons from the photon-pair source are matched to the $D_1$ line in atomic rubidium. Type-II phase matching, a tuneable-birefringence resonator and MHz-resolution pump tuning are used to achieve independent frequency control over each photon in the pair with MHz precision, enabling them to excite different hyperfine transitions in rubidium. We have designed and implemented tuneable FPI, also with $\sim$ MHz control over their resonance frequencies, to isolate a single frequency mode-pair from the CE-SPDC source. The filters have $\sim 90\%$ on-resonance transmission and extinguish unwanted frequency components by over 20 dB. The thesis includes predictions of the two-photon spectra at the output of the CE-SPDC source, and also after the filters, based on existing theoretical models of CE-SPDC. We measure the two-photon linewidth, the number of modes in an emission cluster and the spacing between clusters, the second-order cross-correlation and heralded autocorrelation functions, and find good agreement with predictions. We demonstrate independent tuneability of the signal and idler frequencies by atomic absorption spectroscopy with the filtered CE-SPDC output as the light source.

We also report a technique to resolve narrow frequency differences between photons with a high frequency resolution. The technique, which we call autoheterodyne characterisation, can measure the photon-pair joint spectra by detecting the time-correlation beat-note when nondegenerate photon-pairs interfere at a beamsplitter. It implements a temporal analog of the Ghosh-Mandel effect with one photon counter and a time-resolved Hong-Ou-Mandel interference with two. We provide a complete theoretical description of the process and show how the distribution of sum and difference frequencies in the photon-pair spectrum can be obtained from measured correlation functions. Through a power spectral analysis of the correlation measurements, the strengths,

linewidths and relative frequencies of the spectral content in the two-photon state is obtained. With this, it is possible to quantify the contribution of undesired frequency modes when a single mode output is required. We analyse the application of this technique to photon-pairs that are produced by narrowband pumping and are strongly anti-correlated in frequency, and to pairs with reduced frequency correlations produced by broadband pumping. Experimentally, we demonstrate this technique using photon-pairs from the filtered CE-SPDC source described in the previous paragraph, that have a frequency separation of $\sim 200\,\mathrm{MHz}$. From the results, we quantify the performance of the filters and verify the accuracy of our model for the two-photon joint spectra from this source.

# RESUMEN

Esta tesis describe trabajos de laboratorio, que tienen como objetivo generar y caracterizar fotones individuales y pares de fotones, aptos para interactuar con átomos fríos. Para este fin, el espectro conjunto o contenido en frecuencia de los fotones pares es de particular interés. El átomo considerado en la tesis es rubidio. Primero describimos una fuente de pares de fotones, basada en el proceso de conversión paramétrica descendente espontánea (spontaneous parametric down-conversion, SPDC por sus siglas en inglés), aumentada por un resonador óptico (cavity-enhanced SPDC, o CE-SPDC). Este proceso genera pares de fotones de banda estrecha, con un ancho de banda de $\approx 5$ MHz. Ambos fotones producidos por la fuente concuerdan en frecuencia con la línea D1 del rubidio atómico. La coincidencia de fases (phase matching) de tipo dos, un resonador de birrefringencia ajustable, y una bomba de frecuencia ajustable con resolución de unos MHz, son usados para conseguir control independiente sobre la frecuencia de cada fotón del par, con precisión de MHz, permitiendo que exciten diferentes transiciones hiperfinas del rubidio. Diseñamos e implementamos filtros Fabry-Perot sintonizables, también con una precisión de control de $\sim$ MHz en su frecuencia de resonancia. Con dichos filtros, demostramos la selección de pares de fotones que provienen, cada uno, de un solo modo del resonador, y por lo tanto con un ancho de banda definido por dicho modo. Los filtros tienen una transmisión del $\sim 90\%$ en resonancia y extinguen componentes fuera de banda en 20 dB. Calculamos el espectro conjunto de los pares de fotones producidos, tanto a la salida de la fuente, como después de lo filtros, a base de modelos teóricos de CE-SPDC. Medimos el ancho de banda de ambos fotones, el número de modos de emisión en un cúmulo, el espaciado espectral entre grupos de modos cuasi-resonantes, y las funciones de correlación cruzada de segundo orden y de autocorrelación anunciada, y resultan estar en buen acuerdo con las predicciones. Demostramos un ajuste independiente de la frecuencia del fotón signal y del fotón idler mediante espectroscopía de absorción con la salida del CE-SPDC como fuente de luz.

También presentamos una técnica para distinguir diferencias estrechas de frecuencia entre fotones con una gran resolución en frecuencia. Esta técnica, a la que llamamos caracterización autoheterodina, permite medir el espectro conjunto de un par de fotones

mediante la detección de la correlación en tiempo de su batido (beat-note) cuando el par de fotones no-degenerados interfiere en un divisor de haz. Esta técnica implementa un análogo temporal al efecto Ghosh-Mandel con un contador de fotones y una interferencia Hong-Ou-Mandel con resolución temporal con dos. Proporcionamos una descripción teórica completa del proceso y mostramos como la distribución de la suma y diferencia de frecuencias en el espectro del par de fotones puede obtenerse a partir de las medidas de las funciones de correlación. Mediante el análisis del espectro de las medidas de correlación, se obtienen las amplitudes, anchos de línea y frecuencias relativas del contenido espectral del estado conjunto de los dos fotones. Con esto, es posible cuantificar la presencia de modos indeseados de frecuencia cuando se requiere una salida monomodo. Analizamos la aplicación de esta técnica a pares de fotones producidos por bombeo de banda estrecha y fuertemente anti-correlacionados en frecuencia, y a pares con correlaciones de frecuencia reducidas producidos por bombeo de banda ancha. Experimentalmente, demostramos esta técnica usando pares de fotones generados por la fuente descrita en el párrafo anterior, con una separación en frecuencia de $\sim 200$ MHz. A partir de los resultados, cuantificamos el desempeño de los filtros y verificamos la exactitud de nuestro modelo para el espectro conjunto de los dos fotones provenientes de la fuente CE-SPDC con filtros.

# ACKNOWLEDGEMENTS


காலத்தி னாற்செய்த நன்றி சிறிதெனினும்
ஞாலத்தின் மாணப் பெரிது.

***A timely favour, however trivial,***
***its material value, is akin to the whole world.***

– Thirukkural, 1st c. BCE

It has been a long journey; the consequence of several events, circumstances and people that conspired in unison to make “me” reach this point in time. “Me" is in quotes because while I may be the one ultimately acquiring a certain respected title, this is a collective success of everyone and everything that contributed to the journey. Although the results in this thesis are not solely mine to take credit for and then thank others for helping, the journey as experienced by me is exclusively mine. It has been a wonderful journey to get here, and this is my opportunity to thank everyone who was involved in making my pursuit of a Ph.D. a rewarding and stimulating experience.

This journey would have been impossible to begin or complete without my parents and their financial, psychological and physical support. They created a safe haven I could return to during times of crisis and gave me the philosophical moorings to remain equanimous and motivated through challenges. They have always encouraged all meaningful and creative pursuits. They are forever my heroes.

I genuinely feel fortunate to have had Morgan as my thesis advisor. It is impressive that a professor with four labs and leading a team of over fifteen people is **always** available for his students. A fantastic teacher with a knack for demystifying complicated concepts with just a pen and the white board, he leaves his door always open for students to barge right in with their questions. It is also impressive that the feedback he gives for written content, be it a manuscript, a conference abstract, a thesis chapter or even a poster, is almost instantaneous in addition to being tremendously detailed! If this thesis is written well, a huge part of the credit goes to him for revising each chapter on average

five times. Working with him has been highly stimulating intellectually and genuinely fun. Thank you Morgan for tolerating my insolence, never micromanaging, giving me opportunities to debate or express disagreement, being an eager teacher, a fantastic mentor and a genuinely caring person. Thank you for being as involved in my project as a post-doc would have been. I hope I have imbibed at least a fraction of your scientific rigour, critical analysis, ability to assimilate concepts, clarity in communicating science, keen eye for detail, lateral thinking, ability to be broadly informed, persuasion skills, ability to suffer fools (like me :P) and wisdom.

Anne, you are truly a superwoman. I am confident that I would have suffered at least a 20% reduction in productivity if not for your pro-activeness in helping me with the most serious and silliest of tasks I had difficulties with, as a foreigner who didn't speak Spanish. Thanks is too small a word to say for all the times you went beyond the call of duty to help me. I'm sincerely indebted to you.

I would like to thank all members of the single ruby lab for their roles in this journey and my personal growth. Thank you Natalia Bruno for being a friendly post-doc, Nan for making my first years in the lab enjoyable, Lorena for being a source of inspiration through the indomitable strength you've shown in facing repeated crises, Nat A. for being such a sweet office and lab buddy and Laura for being a patient student and for translating the thesis abstract into Spanish. Thanks Pau and Simon for always being ready to answer my tech-n00b questions with a smiling face. Ola - the three months I worked with you in the lab were undoubtedly the best months of my Ph.D. Teaming up with you sparked a drive and purpose that were unparalleled during my Ph.D. I am so grateful you showed up at ICFO one day!

I would like to thank ICFO as an institution for the efficient organisation of research and providing resources like the HR, purchasing department, logistics, IT and electronic and mechanical workshops. This helped me dedicate time exclusively to research. Thanks Ingrid, Santi, Magda, José Carlos and team, Xavi and team, Carlos Dengra and team and Oriol and team for all your help. I doubt I will get as much support in other institutes.

My friends have added meaning and colour to my life outside of work. They have made my life in Barcelona truly cherishable and memorable. They have exposed me to diverse cultures, ideologies, philosophies, pursuits and experiences that have made me richer in the course of these years. Thank you Anuja, Prem, Saoni, Arun, Nata, Rinu, Anna, Ipsu and Jules for being my family away from home. You've been my pillars of

support here and I could surely write pages about how awesome each of you is! Thank you Slaven, Lukas & Kora, Samyo, Sukku, Raghu, Hara, Chiara, KKG, Pamina, Barbara, Alba, Jessica, Patrick & Helena, Daniel, Marcos, René, Aamir, Varun, Manu, Swapan and Chris for all the laughs, trips, food and countless memories. The last years would have been lacklustre without you.

Some relationships transcend thank yous. I am lucky to have Lalu, Ani and Achu in my life adding to the core of my strength and Ammamma, Ammuma, Thathuji, Athais, Perips, Mami and Mama nurturing a deeply rooted, caring and affectionate family tree that watches over me always. This thesis is dedicated to my family.

# PUBLICATIONS

- **V. Prakash**, A. Sierant, and M. W. Mitchell,
  *Autoheterodyne characterization of narrow-band photon pairs,*
  Phys. Rev. Lett. 127, 043601 (2021).

- **V. Prakash**, L. C. Bianchet, M. T. Cuairan, P. Gomez, N. Bruno, and M. W. Mitchell,
  *Narrowband photon pairs with independent frequency tuning for quantum light-matter interactions,*
  Opt. Express 27, 38463 (2019).

- N. Bruno, L. C. Bianchet, **V. Prakash**, N. Li, N. Alves, and M. W. Mitchell,
  *Maltese cross coupling to individual cold atoms in free space,*
  Opt. Express 27, 31042 (2019).

# CONTENTS

# 1

# INTRODUCTION

## 1.1 BACKGROUND AND MOTIVATION

States containing one or a few photons have been used to elucidate many aspects of quantum mechanics such as quantum interference effects [1], entanglement [2] and violation of Bell's inequalities [3]. They have been used to study light-matter interactions and find applications in quantum computing [4] and quantum sensing [5]. However, since photons hardly interact with each other, most of the phenomena studied so far with nonclassical light as the input to an optical process, concern linear optics. In such cases, the phenomenon studied is revealed through light-matter interactions in which the response of the material to the input photons is the same for every photon irrespective of the number of photons. There is far less work on quantum light-matter interactions built upon the coherent interaction of nonclassical light with a single isolated quantum system, or an isolated small ensemble of such systems, where the response of the material to few-photon fields is no longer linear. For example, fundamental processes like stimulated emission, critical to lasers and other essential technologies, have to date not been studied at the level of a single quantum emitter in free space coupled to single photons. There are theoretical studies that predict modifications to the statistics of exotic quantum states of light (such as chaotic, bunched/antibunched, squeezed photons) when they interact with a single quantum emitter [6]. The signatures of quantum interference effects such as the Hong-Ou-Mandel effect are expected to be modified in the regime of quantum light-matter interactions due to the nonlinearity in the response of quanta of matter to photons [7–9]. The experimental investigation of such predictions remains to be explored. Exploring light-matter interactions at the level of individual quanta may further our understanding of basic processes in light-

matter interaction, and help to translate this knowledge to advancements in quantum technologies. Such studies are important for applications of quantum nonlinear optics, where photon-photon interactions are mediated by a few atoms or in hybrid quantum networks where atoms/ions/molecules serve as memories, repeaters or processing units of the quantum information encoded in photons.

Since its first demonstration in the 1970s, spontaneous parametric down-conversion (SPDC) has become a ubiquitous technique to produce nonclassical states of light for photonic quantum technology [10]. Although the art of production and manipulation of quanta of light had a head start with SPDC, the trapping and manipulation of single-quanta of matter has matured in parallel since the 80s. Starting with the resonance fluorescence experiment of Kimble and Mandel in 1977 [11], and continuing with cavity QED experiments from the 1980s forward [12, 13] signatures of the interaction of light with individual atoms inside cavities began to emerge from physics laboratories. The first single neutral atom was isolated in a cavity in 1999 [14]. Advancements in ion trapping [15, 16] greatly increased the capacity for atomic control and increased the interaction time available between light and atoms. Beginning with the work of Schlosser et al. in 2001 [17], individual trapped single neutral atoms became readily available, held in far-off-resonance traps (FORTs), a.k.a. "optical tweezers," in which a trapping beam is strongly focused to create a wavelength-dimension conservative potential well. The same high-NA optics can be used for efficient collection of atomic fluorescence, making the individual atoms detectable. Starting with the pioneering work of Tey et al. in 2009 [18, 19], it became possible to strongly couple travelling-wave photons to individual atoms, using the same high-NA focusing optics. This opened the possibility to study many physical processes that were masked by the artificial boundary conditions of cavity QED, including transmission phase shifts by an atom on light [20], and time-reversal of the emission process [21]. These works were performed with weak coherent states from lasers. Over the years, individual quanta of several other types of material systems, such as molecules [22] and impurities in solids [23] have been successfully isolated and probed with classical light [24]. With the present technological advancements in preparing single quanta of both light and matter, we are progressing into the era of exploring quantum light-matter interactions.

The coherent interaction of nonclassical light with a material quantum systems requires a resonant or near-resonant optical response of the material, to achieve a strong interaction with propagating [19] or cavity-bound [25] photons. Recently, it has been

shown that the optical response achieved is stronger when the input photons are spectrally [26] and temporally [27] tailored to match the targeted transition. This requires narrowband photons, as strong transitions in atoms and molecules typically have a narrow bandwidth, in the order of MHz. Light-matter quantum interface technologies with applications in quantum information processing and networking, e.g. entanglement-swapping with memory-compatible photons, will require photons or photon pairs that, in addition to being narrowband, are pure, indistinguishable [28] or entangled [29, 30]. This requires control over the spatial mode, frequency, correlations and bandwidth of photons with minimal contamination by photons of unwanted frequencies.

## 1.2 CE-SPDC FOR SPECTRALLY TAILORED PHOTONS

In SPDC, high-frequency "pump" photons from a laser spontaneously decay to produce time-correlated pairs of lower-frequency "signal" and "idler" photons in a nonlinear crystal. The photons from SPDC are typically broadband. They can be made suitable for interaction with atoms after bandwidth reduction through spectral filtering, at the cost of brightness [31]. However, this loss in brightness can be avoided through cavity enhanced spontaneous parametric down-conversion (CE-SPDC). Since CE-SPDC was first demonstrated [32], it has become the workhorse method for producing narrowband photon-pairs with tailored properties to match a material system [33]. In CE-SPDC, the process of SPDC occurs inside an optical resonator that resonates the down-converted fields. The resonator both enhances the spectral brightness of the resonant signal-idler frequencies via the Purcell effect [34], and influences the spatial modes, frequencies and bandwidths of the down-converted photons. CE-SPDC has proven to be a reliable technique to generate bright [35] and narrowband photons for interaction with matter [36–42]. Photons with linewidths on the order of MHz and even 100s of kHz [41] have been produced with his technique. Several works have used heralded single photons from CE-SPDC to excite single trapped atoms, quantum dots and solid state quantum memories [43–51]. Heralded photons from two separate sources have been used to entangle two remote solid-state memories [52]. However, few studies so far have interfaced both photons from a down-converted pair with a single material system [5].

Previously reported narrowband, material-resonant sources could tune one of the output photons, sometimes over a large range [49], with a consequent effect on the

other photon's frequency. That is, the signal and idler photon could not be tuned independently. Such sources are not well suited for several tasks in quantum-light matter interactions that require independent tuning of the CE-SPDC signal and idler. Driving multi-photon processes in a single material system, or direct interaction with distinct systems are examples of such tasks. Most material systems of interest have multiple, closely-spaced internal levels due to hyperfine splitting. Multi-photon processes among these internal levels, e.g. stimulated Raman transitions, involve photons of different frequencies. In most cases, the isolated material quanta experience environment-induced energy shifts, e.g. crystal field shifts in impurities in solids or trap-induced level shifts in atoms. To address specific transitions in these, a general-purpose CE-SPDC source should have independent tuning of the frequencies of signal and idler, derived from an absolute frequency reference, e.g. an atomic or molecular spectroscopic feature. Such a source opens the way to studies of resonant multi-photon effects at the most fundamental, individual-quantum level. One major motivation for such studies are the many proposals for strong photon-photon interactions [53–59], of interest to quantum information processing. For example, sub-wavelength arrays of neutral atoms support sub-radiant states [60] that can exhibit topological protection [59] and unprecedented optical properties [61]. Strong photon-photon interactions [62] that could be harnessed for photonic quantum-information processing, and photonic bound states [63, 64] are predicted in such arrays. To date these mechanisms have only been tested with classical light [65–67]. Exploring this physics motivates nonclassical light sources in which both photons are resonant to an atomic transition and are independently tuneable. This thesis describes the development of such a light source [68] and its characterisation.

## 1.3 INTRODUCTION TO THESIS WORK

The primary goal of this thesis has been to prepare a photon-pair source based on CE-SPDC, for resonant excitation of a single rubidium ($^{87}$Rb) atom trapped at the focus of four high-NA lenses [69, 70]. To restate the requirements for interfacing multiple photons with a single atom, the photon source used would have to be sufficiently bright and supply single-mode (in frequency), narrowband photons resonant with the atom. Additionally, the frequency of the photons would need to be tuneable to address light-shifted transitions (which could have an order of magnitude comparable to the transition bandwidth) or to excite various hyperfine levels (which may have frequency spacings

$2-3$ orders of magnitude greater than the light induced shifts). This requirement motivates us to ensure our source produces single-mode, narrowband, atom-resonant photon-pairs with independent control over the frequency of each photon in the pair. Specifically the source is designed to produce photons resonant to the $5^2S_{1/2} \rightarrow 5^2P_{1/2}$ line, a.k.a the $D_1$ line in neutral atomic rubidium, which has resonance at $\sim 794.7\,nm$ and a natural linewidth of $5.7\,MHz$. Rubidium is a well-developed system for strong light-matter interactions in free space [17, 19, 71–74] and the geometry of the atom trap is sufficiently versatile to change the trap configuration to an array or cloud of atoms [70]. Thus, the source has also been developed to be versatile, to enable a range of possible experiments on light-matter interactions at the $D_1$ line. The photons from a down-converted pair are polarised perpendicular to each other and can be easily entangled if needed. While both photons from the source are resonant to the $D_1$ line, their individual frequencies can be adjusted with MHz resolution and a over range in the order of GHz, to address different transitions or compensate for transition frequency shifts. The signal-idler photons delivered are single-mode, in the sense that signal and idler each come from a respective single cavity mode, with a consequent restriction of the frequency content of these photons. Light not resonant to the atom is thus suppressed, which will reduce background noise in atom-photon experiments. Using a combination of time-correlated photon counting and atomic spectroscopic methods, we demonstrate a single mode output and independent tuneability over the $D_1$ line.

The frequency correlations of SPDC photon-pairs, including time-frequency entanglement, are of particular importance. In some applications these correlations are used to encode quantum information [75, 76]. In others, the frequency correlations are an undesired side-channel that reduces nonclassical interference [77]. These correlations are revealed through analysis of the joint spectral amplitude (JSA) or joint spectral intensity (JSI) of the down-converted photon-pair. In broadband SPDC applications, it is possible to directly measure the JSI using monochromators or other passive filters [78, 79]. Techniques such as Fourier transform spectroscopy using Mach-Zehnder interferometers [80] and temporal magnification of photons where a "time lens" is used to compress the photons' bandwidth and elongate the temporal spread [81] have also been used to measure the JSI of broadband photons. Nonclassical interference can also be a tool to characterise nonclassical frequency correlations; the Hong-Ou-Mandel (HOM) [1] interference visibility has been used to characterise broadband photon-pairs from a single source [77, 79, 82] and from different sources [83, 84]. However, there are hardly

any techniques to characterise the JSI of narrowband photons, which require MHz precision in frequency resolution. On developing a narrowband source with fine frequency control over the produced photons, we were faced with the need to progressively develop methods to characterise these photons, measure their spectrum and verify their quality, i.e., the extent to which the frequency content is limited to a single cavity mode. We thus developed *autoheterodyne characterisation* (AHC), a high-resolution technique to measure photon-pair joint spectra through time-resolved coincidence detection after interference on a beamsplitter.

## 1.4 STRUCTURE OF THE THESIS

The thesis is broadly divided into two parts. Part-I is focussed on the system that delivers tuneable, single-mode photon-pairs matched in frequency and bandwidth to the Rb $D_1$ line. It comprises chapters that detail the construction of the CE-SPDC source, the design of resonance-tuneable Fabry-Perot filters that select a single frequency mode from the CE-SPDC output and the design implemented to achieve independent control over the signal-idler frequencies from the source. Analysis of the signal/idler spectrum through spectroscopy measurements is included here. While the CE-SPDC apparatus is designed to produce photon-pairs that can interact with this single system, our techniques can be readily applied to other wavelengths for interaction with other material systems or combinations of them. Part-II of the thesis is focussed on correlation measurements for characterising photons from the source. We first analyse the statistics of the photons from our source using established measurement methods. We use time-correlated photon counting to obtain the intensity cross- and autocorrelation functions, which can be compared against model predictions. We then perform a more complete characterisation of the two-photon JSI using AHC. We provide a thorough mathematical analysis of AHC. We model the JSA and JSI from our source with varying levels of detail and simulate the results from AHC for the various models. We also show the usefulness of AHC to characterisation of frequency correlations in two-photon states from SPDC.

The thesis is organised as follows:

***Part-I***

- **Chapter 2** is dedicated to the core of the system - the CE-SPDC source. The chapter begins with a brief theoretical introduction to the two-photon state from

SPDC and to how the two-photon joint spectrum is modified in cavity-enhanced SPDC. The specifics of the design of our CE-SPDC source are provided. Attributes of cavities and CE-SPDC such as the clustering effect, two-photon linewidth etc., are defined and values specified for our design. Simulations of the spectral structure from the source and experimental measurements of the down-converted spectrum through difference frequency generation (DFG) are presented.

- **Chapter 3** describes the design and construction of tunable filters capable of efficiently transmitting a single CE-SPDC mode while blocking all other modes. First the modification to the two-photon JSA from CE-SPDC on filtering is analysed. The filter parameters required to ensure a single frequency mode pair output are discussed. The details of the filter design provided and the signal spectrum after the filtering is simulated. Experimentally, the tuneable-filter is used to map and adjust the spectrum of the signal from CE-SPDC.
- **Chapter 4** deals with the lasers and control-systems around the core CE-SPDC source that enable frequency tuning of the produced photons. This is achieved through an interconnected frequency stabilisation scheme that controls the pump, CE-SPDC cavity length and crystal temperatures based on an atomic reference. We experimentally demonstrate the independent tuneability by rubidium vapour absorption spectroscopy.

***Part-II***

- **Chapter 5** introduces the second order cross- and autocorrelation measurements, which are established methods to characterise SPDC photons. We apply these tests to the CE-SPDC output photons. We report figures of merit important for an atom-photon experiment such as brightness, heralding efficiency, correlation time and suppression of multi-photon emission.
- **Chapter 6** presents AHC as a tool to characterise narrow frequency features in pair source outputs. It contains the theoretical framework that provides an interpretation of the physics involved in AHC. It presents simulations and experimental demonstrations of AHC results from our source. We also simulate the results for broadband pumping to show how the technique may be used to characterise two-photon states with reduced frequency correlations between the photons in the state.

- **Chapter 7** summarises the important results in the thesis, suggests improvements that can be made to the experimental set-up and outlines the topics for investigation immediately following this thesis work.

# Part I

# NARROWBAND, SINGLE-MODE, INDEPENDENTLY TUNEABLE & ATOM-RESONANT PHOTON-PAIRS

# 2

# CAVITY-ENHANCED SOURCE OF PHOTON PAIRS

As mentioned in the introduction, a large part of this thesis work was dedicated to preparing a source of correlated photon-pairs that are in a single frequency-mode, resonant to the $D_1$ line in rubidium and with a linewidth comparable to the same. This chapter is focussed on the photon-pair source and the theory relevant to that. The photons are produced by a process of cavity-enhanced spontaneous parametric down-conversion (CE-SPDC) where only the down-converted fields are resonant in the cavity. For completeness, a brief theoretical description of the most important phenomena that influence the spectrum from the source is presented first, following which a detailed description of the set-up is given. We then present calculations and experiments to characterise the spectrum.

## 2.1 INTRODUCTORY THEORY

### 2.1.1 Nonlinear frequency conversion and SPDC

As light passes through a material medium, it induces polarisation. Depending on the medium, the polarisation density $\widetilde{\mathbf{P}}(\mathbf{r}, t)$, at a position $\mathbf{r}$ and at a time $t$, induced in it by the optical electric field $\widetilde{\mathbf{E}}(\mathbf{r}, t)$ may or may not be linearly dependent on the electric field. The polarisation density is related to the electric field through the electric susceptibility of the medium ($\chi$). Media in which the polarisation density has a nonlinear relationship with the incident electric field(s) are called nonlinear media and their susceptibilities $\chi^{(n)}$ are described by rank- (n+1) tensors. Such media are used for parametric nonlinear frequency conversion of light, where electro-magnetic waves of different frequencies exchange energy with each other through the nonlinear response of a medium, with their

total energy conserved. In this thesis we are concerned with processes that involve a $\chi^{(2)}$ medium. In such second-order frequency convertion processes, the Fourier amplitude of the nonlinear polarisation $P(\omega_n + \omega_m)$ at a frequency $\omega_n + \omega_m$ is related to the Fourier amplitudes of the input electric fields $E(\omega_n)$ and $E(\omega_m)$ at frequencies $\omega_n$ and $\omega_m$ according to [85]

$$P_a(\omega_n + \omega_m) = \sum_{bc} \sum_{(nm)} \chi^{(2)}_{abc}(\omega_n + \omega_m; \omega_n, \omega_m) E_b(\omega_n) E_c(\omega_m). \tag{2.1}$$

Here the indices $abc$ refer to the Cartesian components of the field and $(nm)$ indicates that $\omega_n + \omega_m$ is fixed although $\omega_m$ and $\omega_n$ vary in the summation.

From the 1960s, several quantum mechanical theories for parametric processes have been developed [86–88]. Spontaneous parametric down-conversion (SPDC) is one such process where a high energy "pump" photon spontaneously decays into two photons of lower energy ("signal" and "idler"), within a medium that shows $\chi^{(2)}$ nonlinearity. SPDC was first suggested as a source of photon pairs in 1970, both in the USSR by D. N. Klyshko [89] and in the US by Burnham and Weinberg [90]. Burnham and Weinberg also experimentally demonstrated photon-pair production in an ammonium dihydrogen phosphate crystal and analysed the energy and momentum conservation among the fields involved. A full quantum theory of SPDC was derived by Hong and Mandel in the 1980s [91]. They used this to predict and explain several nonclassical phenomena such as violation of Bell's inequalities [92] and quantum interference effects [1, 93, 94], thereby proving the intrinsic quantum character of the light from the SPDC process.

It is beyond the scope of this thesis to restate these SPDC theories. There are several papers and theses that discuss this in detail. Here we restate the results found in the PhD thesis of Andreas Ahlrichs [95], which is particularly thorough.

### *Joint Spectral Amplitude and Intensity*

We consider the signal (subscript-s) - idler (subscript-i) two-photon state from SPDC of a pump photon (subscript-p) with a spectral distribution $s(\omega'_p)$, in a crystal of length $l$. We restrict the discussion to collinear propagation of all the fields involved. When the signal and idler are initially described by the vacuum state ($|0_s\rangle\,|0_i\rangle \equiv |0,0\rangle$), the nonvacuum part of the time-evolved two-photon state, after a long interaction time and to the first order in $\chi^{(2)}$ is [95],

$$|\psi\rangle = \pi l\kappa \int d\omega_i \int d\omega_s \int d\omega'_p \, s(\omega'_p) \times \delta(\omega'_p - \omega_s - \omega_i)\mathrm{sinc}\,(\Delta k\, l/2) \;\; \hat{a}^\dagger_s(\omega_s)\hat{a}^\dagger_i(\omega_i)\,|0,0\rangle\,. \tag{2.2}$$

Here $\hat{a}^\dagger_s(\omega_s)$ and $\hat{a}^\dagger_i(\omega_i)$ signify the creation of a signal photon of frequency $\omega_s$ and an idler photon of frequency $\omega_i$ respectively, $\delta(\omega'_p - \omega_s - \omega_i)$ is the energy conservation condition between the produced signal-idler photons and the annihilated pump photon with frequency $\omega'_p$. $\mathrm{sinc}\,(\Delta k\, l/2)$ is the phase matching function which depends on the momentum mismatch $\Delta k = k_p - k_s - k_i$ among the fields along the direction of propagation. Here,

$$\kappa = \frac{i}{\hbar}\frac{\chi^{(2)}_{\mathrm{eff}}}{2} E_p \, \mathcal{E}_s \, \mathcal{E}_i \tag{2.3}$$

is a constant, $\hbar$ is Planck's constant, and $E_p$ is the pump amplitude [1]. $\mathcal{E}_\epsilon$ (where $\epsilon \in \{s, i\}$) is a factor in the Fourier amplitude of the quantised signal/idler optical electric field [2], specified at a frequency $\omega^0_\epsilon$,

$$\mathcal{E}_\epsilon \equiv \sqrt{\frac{\hbar\omega^0_\epsilon}{2\epsilon_0 n(\omega^0_\epsilon)cA}}\sqrt{\frac{1}{2\pi}}\,, \tag{2.4}$$

where $\epsilon_0$ is the permittivity of free space, $n(\omega^0_\epsilon)$ is the refractive index in the medium at the frequency $\omega^0_\epsilon$, $c$ is the vacuum speed of light and $A$ is the quantisation area. $\mathcal{E}_\epsilon$ is related to the quantised field operator $\hat{E}^{(+)}_\epsilon(t)$ [3] for $\epsilon \in \{s, i\}$ according to,

$$\hat{E}^{(+)}_\epsilon(t) = \mathcal{E}_\epsilon \int_{-\infty}^{\infty} d\tilde{\omega}_\epsilon \; \hat{a}_\epsilon(\tilde{\omega}_\epsilon)\; e^{-i\tilde{\omega}_\epsilon t} \tag{2.5}$$

where $t$ is time and $\hat{a}_\epsilon(\tilde{\omega}_\epsilon)$ is the creation operator $\hat{a}$ creating a photon in mode $\epsilon$ with a frequency $\tilde{\omega}$.

The expression for the two-photon state can be further simplified to,

$$\begin{aligned} |\psi\rangle &= \pi l\kappa \int d\omega_i \int d\omega_s \, s(\omega_s + \omega_i)\mathrm{sinc}\,(\Delta k\, l/2) \;\; \hat{a}^\dagger_s(\omega_s)\hat{a}^\dagger_i(\omega_i)\,|\psi_0\rangle \\ &\equiv \kappa \int d\omega_i \int d\omega_s \, f(\omega_s, \omega_i)\hat{a}^\dagger_s(\omega_s)\hat{a}^\dagger_i(\omega_i)\,|0,0\rangle\,. \end{aligned} \tag{2.6}$$

1 The pump is treated as a classical wave.

2 $\mathcal{E}_\epsilon$ is slowly varying over the range of frequencies that have a significant amplitude in the down-converted state, which is why it has been pulled out of the integral in Equation 2.5.

3 Here we have neglected the position dependence of the electric field since we are only interested in a single spatial mode of the fields involved.

As can be seen from Equation 2.6, the signal and the idler photons' frequencies are jointly described by $f(\omega_s, \omega_i)$- the **Joint Spectral Amplitude (JSA)**. The JSA of the state from SPDC in a free-space crystal is proportional to the product of the pump spectral shape $s(\omega_s + \omega_i)$ and the phase matching function $l\,\mathrm{sinc}\,(\Delta k\, l/2)$. More specifically, for a monochromatic pump with central frequency $\omega_p$, $s(\omega_p') \to \delta(\omega_p - \omega_p')$ and the two-photon state is,

$$\begin{aligned} |\psi\rangle_{NB} &= \pi l \kappa \int d\omega_i \int d\omega_s \\ &\quad \times \delta(\omega_p - \omega_s - \omega_i)\mathrm{sinc}\,(\Delta k\, l/2) \;\; \hat{a}_s^\dagger(\omega_s)\hat{a}_i^\dagger(\omega_i)\,|0,0\rangle \\ &\equiv \kappa \int d\omega_i \int d\omega_s\, f_{NB}(\omega_s, \omega_i)\hat{a}_s^\dagger(\omega_s)\hat{a}_i^\dagger(\omega_i)\,|0,0\rangle\,, \end{aligned} \tag{2.7}$$

where $f_{NB}$ is the two-photon JSA for narrowband pumping.

The rate of production of down-converted photon pairs is proportional to the square magnitude of the two-photon state.

$$\begin{aligned} \langle\psi|\psi\rangle &= |\kappa|^2 \int d\omega_i' \int d\omega_s' \int d\omega_i \int d\omega_s \\ &\quad \times f^*(\omega_s', \omega_i') f(\omega_s, \omega_i)\,\langle 0,0|\,\hat{a}_s(\omega_s')\hat{a}_i(\omega_i')\hat{a}_s^\dagger(\omega_s)\hat{a}_i^\dagger(\omega_i)\,|0,0\rangle \\ &= |\kappa|^2 \int d\omega_i \int d\omega_s |f(\omega_s, \omega_i)|^2, \end{aligned} \tag{2.8}$$

on applying the commutation relations $[\hat{a}_\epsilon(\omega_\epsilon), \hat{a}_\nu^\dagger(\omega_\nu')] = \delta_{\epsilon,\nu}\delta(\omega_\epsilon - \omega_\nu')$ for Kronecker delta function $\delta_{\epsilon,\nu}$ and Dirac delta function $\delta(\omega_\epsilon - \omega_\nu')$ when $\nu, \epsilon \in \{s, i\}$,to simplify the first line to the next. The population of pairs produced is distributed with a probability density that is proportional to $|f(\omega_s, \omega_i)|^2$ which is the **Joint Spectral Intensity (JSI)**. From Equation 2.6 we find,

$$|f(\omega_s, \omega_i)|^2 \propto l^2 \mathrm{sinc}^2\,(\Delta k\, l/2)\,. \tag{2.9}$$

### 2.1.2 Phase matching

From Equation 2.9, the efficiency of the SPDC process is dependent on the length of the crystal ($l$) and on the mismatch of wave-vectors ($\Delta k$) among the fields. For a collinear process, where all the involved fields propagate in the same direction, $\Delta k = k_p - k_s - k_i$ is the mismatch of the field momenta along the direction of propagation. The momenta

are related to the respective frequencies $\omega$, frequency dependent refractive indices $n(\omega)$ and the vacuum speed of light $c$, according to the dispersion relation $k(\omega) = \omega\, n(\omega)/c$. The produced two-photon state has maximum amplitude for perfect phase matching, i.e. when $\Delta k = 0$. Perfect momentum conservation or phase matching is achieved when

$$\begin{aligned} k_p &= k_i + k_s, \\ \omega_p n_p &= \omega_i n_i + \omega_s n_s. \end{aligned} \tag{2.10}$$

Simultaneously, energy conservation mandates

$$\omega_p = \omega_i + \omega_s \tag{2.11}$$

to be satisfied for SPDC to produce photons of frequency $\omega_s$ and $\omega_i$. Most transparent nonlinear media are dispersive and the refractive index increases with frequency, which makes it difficult for both energy and momentum conservation to be satisfied. However, it is possible to satisfy these conditions in birefringent media, where the refractive index is additionally dependent on the polarisation of light. The refractive index of light in any given birefringent medium is determined by the direction of propagation and field polarisation with respect to the optic axis. If the electric field is polarised perpendicular to the plane formed by the propagation direction and the optic axis, it is called ordinary (o) polarisation and has a refractive index $n_o(\omega)$. If the field is polarised along the plane formed by the propagation direction and the optic axis, it is called extraordinary (e) polarisation and its refractive index $n_e(\theta, \omega)$ depends on the angle between the direction of propagation and the optic axis ($\theta$). If phase matching (for any second order nonlinear process) is achieved when the lower frequency fields (signal-idler fields in SPDC) are polarised along the same direction and are perpendicularly polarised w.r.t. the highest frequency field (the pump in SPDC), the process is said to be **type-I phase matched**. If phase matching is achieved when the lower frequency fields are perpendicularly polarised w.r.t. each other but one of them is polarised parallel to the highest frequency field, then the frequency conversion process is said to be **type-II phase matched** [96].

### *Phase matching bandwidth*

Equation 2.6 shows that the two-photon state will have maximum amplitude at signal-idler frequencies $\omega_s^0$ and $\omega_i^0$, for which perfect phase matching is achieved. Nonetheless,

there is a nonzero contribution to the two-photon state even at signal-idler frequencies $\omega_s$ and $\omega_i$, for which there is imperfect phase matching, i.e., for which $\Delta k \neq 0$. This "tolerance" of the phase mismatch by the frequency conversion process implies that the state will contain a range of of signal and idler frequencies that conserve energy with the pump and have momenta such that $\mathrm{sinc}\,(\Delta k\, l/2)$ is not zero.

Taylor expanding $k_s(\omega_s)$ and $k_i(\omega_i)$ around $k_s(\omega_s^0)$ and $k_i(\omega_i^0)$, corresponding to signal-idler momenta that satisfy perfect phase matching $(k_s(\omega_s^0) + k_i(\omega_i^0) = k_p)$ for frequencies $\omega_s^0$ and $\omega_i^0$ that satisfy energy conservation $(\omega_s^0 + \omega_i^0 = \omega_p)$, the phase mismatch becomes

$$\begin{aligned}\Delta k &\approx k_p - k_s(\omega_s^0) - k_i(\omega_i^0) \\ &\quad -\frac{\partial k_s(\omega_s)}{\partial \omega_s}\bigg|_{\omega_s=\omega_s^0}(\omega_s-\omega_s^0) - \frac{\partial k_i(\omega_i)}{\partial \omega_i}\bigg|_{\omega_i=\omega_i^0}(\omega_i-\omega_i^0) \\ &= (\omega_s^0-\omega_s)\left(\frac{\partial k_s(\omega_s)}{\partial \omega_s}\bigg|_{\omega_s=\omega_s^0} - \frac{\partial k_i(\omega_i)}{\partial \omega_i}\bigg|_{\omega_i=\omega_i^0}\right), \end{aligned} \tag{2.12}$$

where we have used the strict energy conservation condition that leads to $(\omega_s^0 - \omega_s) = -(\omega_i^0 - \omega_i)$. Since $k(\omega) = \omega n(\omega)/c$,

$$\frac{\partial k(\omega)}{\partial \omega}|_{\omega=\omega^0} = \frac{1}{c}\left[n(\omega^0) + \omega^0 \frac{\partial n(\omega)}{\partial \omega}|_{\omega=\omega^0}\right] \equiv \frac{n^{(g)}}{c} \equiv \frac{1}{v^{(g)}}, \tag{2.13}$$

where $n^{(g)}$ is the group index in the medium and $v^{(g)}$ the group velocity. Thus,

$$\begin{aligned}\Delta k &\approx \left(\frac{\omega_s^0-\omega_s}{c}\right)\left(n_s^{(g)} - n_i^{(g)}\right) \\ &= (\omega_s^0-\omega_s)\left(\frac{1}{v_s^{(g)}} - \frac{1}{v_i^{(g)}}\right). \end{aligned} \tag{2.14}$$

The propagation delay between the signal and idler photon within the down-conversion crystal is

$$\tau_o = \frac{l}{c}\left(n_s^{(g)} - n_i^{(g)}\right) = l\left(\frac{1}{v_s^{(g)}} - \frac{1}{v_i^{(g)}}\right). \tag{2.15}$$

The phase matching function can be written in terms of the propagation delay as

$$l\,\mathrm{sinc}\left(\frac{\Delta k\, l}{2}\right) = l\,\mathrm{sinc}\left[(\omega_s^0-\omega_s)\left(\frac{\tau_o}{2}\right)\right]. \tag{2.16}$$

The JSI (Equation 2.9) is then,

$$|f(\omega_s, \omega_p - \omega_s)|^2 \propto l^2 \operatorname{sinc}^2 \left[ (\omega_s^0 - \omega_s) \left( \frac{\tau_o}{2} \right) \right]. \tag{2.17}$$

Thus the group delay between the generated signal and idler frequencies in the crystal determines the bandwidth of the SPDC process. $\operatorname{sinc}^2(2\pi x) = 0.5$ when $x \approx 0.22$. Thus the range of frequencies $(\omega_s^0 - \omega_s)$ generated within the full width half maximum (FWHM) of the SPDC intensity is

$$\Delta\omega_{spdc} \approx 2\pi \frac{4 \times 0.22}{\tau_o} = 2\pi \frac{0.88}{\tau_o}. \tag{2.18}$$

This is henceforth referred to as **the SPDC-bandwidth** or **phase matching bandwidth**. This is typically in the order of 100s of GHz to THz.

### *JSI and crystal length*

If perfect phase matching is achieved, the JSI scales quadratically with the length of the crystal (Equation 2.9) and longer crystals can be used for brighter two-photon states. However, for a nonzero $\Delta k$, arbitrarily long crystals are not useful since there is a critical crystal length[4] $l_c = 2\pi/|\Delta k|$ for which the phase matching function is zero. SPDC occurs at every point within the crystal and at $l_c$ the contributions of all the generated fields interfere destructively leading to a zero intensity of down-converted fields.

For degenerate SPDC (i.e $\omega_s = \omega_i = \omega_p/2 = 2\pi c/\lambda_s$) [96],

$$l_c = \frac{2\pi}{|\Delta k|} = \frac{\lambda_s}{2n_p - n_s - n_i}, \tag{2.19}$$

where $\lambda$ is the wavelength, with subscript s indicating that of the signal, $n_j$ is the refractive index of $j \in \{p, s, i\}$ at the corresponding polarisation and frequency.

### *Quasi-phase-matching*

This section is adapted from [96]. Techniques such as quasi-phase-matching (QPM) have been developed to achieve perfect phase matching at any required signal-idler

4 This is prevanlently called "coherence" length [85, 96] although it is not related to a statistical measure of the correlations of a wave.

frequencies. In a crystal with QPM, the nonlinear coefficient is made to vary with a periodocity $\Lambda$ along the length of the crystal such that at a position $z$ in the crystal,

$$\chi^{(2)}(z) = \chi_0^{(2)} \begin{cases} 1 & \sin(2\pi m z/\Lambda) \geqslant 0 \\ -1 & \sin(2\pi m z/\Lambda) < 0. \end{cases} \tag{2.20}$$

Physically, this is achieved by reversing the polarity of the dipoles in the material periodically. The periodically varying nonlinear susceptibility can be expressed as a Fourier series,

$$\chi^{(2)}(z) = \sum_m \chi_m^{(2)} e^{-i\,2\pi m z/\Lambda} \tag{2.21}$$

where $\chi_m^{(2)}$ are the Fourier coefficients. For fixed pump, signal and idler frequencies and fixed directions of propagations w.r.t the crystal axis, the $m^{th}$ Fourier component can be used to achieve perfect phase matching by making $\Lambda = m\, l_c$. Considering only this component of $\chi^{(2)}$, the product $\hat{E}_p^{(+)}\hat{E}_s^{(-)}\hat{E}_i^{(-)}\exp[-i2\pi m/\Lambda]$ is proportional to $\exp[i\Delta k^{(m)} z]$, where

$$\begin{aligned} \Delta k^{(m)} &= k_p(\omega_p, T) - k_s(\omega_s, T) - k_i(\omega_i, T) - \frac{2\pi m}{\Lambda(T)} \\ &= \Delta k - \frac{2\pi}{l_c} = 0. \end{aligned} \tag{2.22}$$

where the last line follows from Equation 2.19. $\Delta k^{(m)}$ can be made 0 at the required energy-conserving signal, idler and pump frequencies by tuning the temperature of the crystal. For the simplest case of $m = 1, \Lambda = l_c$ and in half the period, i.e., half the critical length, the polarity of the medium is flipped once.

### 2.1.3 Cavity-Enhanced SPDC

The first experiments on enhanced parametric frequency conversion processes within a resonator were reported in the 1960s [97] and theory descriptions were developed around the same time [98]. However, these dealt with resonators that were operated close to or above threshold, where the pump power was large enough for the gain from the parametric process to be greater than the losses in the resonator. The earliest works on describing the theory of photon-pair production from SPDC within a resonator, in the far-below threshold regime, were reported in the early 2000s by Lu and Ou [32, 99]. They calculate the reduction in bandwidth, the output mode structure for type-I and type-II

down-conversion and the enhancement in brightness per cavity mode in comparison to the broadband single-pass process. They also experimentally demonstrated SPDC within a cavity and performed time interval distribution measurements of the output photons. Towards the end of that same decade, more complete quantum mechanical models deriving expressions for the JSA and JSI of the two-photon state from SPDC were developed by M. Scholz et al. [100–102] and by Jeronimo-Moreno et al. [103]. Jeronimo-Moreno et al. used an "unfolded cavity" picture to get an expression for the JSA and JSI, in which the light passes through an infinite sequence of crystals whose outputs coherently sum to give the net CE-SPDC output state [103, equation 4]. They do not include losses in their model. They provide a closed-form expression for the JSI, whereas they give the JSA in the form of an infinite sum, the convergence of which is not evident. However, their expression for the JSI is more intuitively appealing as it is in terms of Airy functions that describe cavity resonances. Scholz et al. based their calculations on quantized field operators within the cavity for the down-converted fields and used these in the interaction Hamiltonian to obtain the time-evolved two-photon state. Their expressions for the JSA and JSI are in terms of repeating Lorentzian resonances. They went further and used this to analyse the statistics of the photons from CE-SPDC. They developed analytical expressions for correlations functions based on experimentally accessible parameters.

### *The two-photon state from CE-SPDC*

Due to its more comprehensive nature, we use the model developed by Scholz et al. in this thesis. We alter the notation by introducing new variables to draw a parallel with the results from Jeronimo-Moreno et al. We begin by restating the results from [102]. Scholz et al. consider a type-II CE-SPDC process for a narrowband pump of frequency $\omega_p$, in a cavity which is resonant to the down-converted fields but is transparent to the pump. The cavity has a linewidth ($\gamma$) and Free Spectral Range (FSR) that may be different for the signal and idler fields (indicated with subscript $s$ and $i$ respectively) due to the birefringence and frequency dependent losses in the cavity (see Equation 2.36).

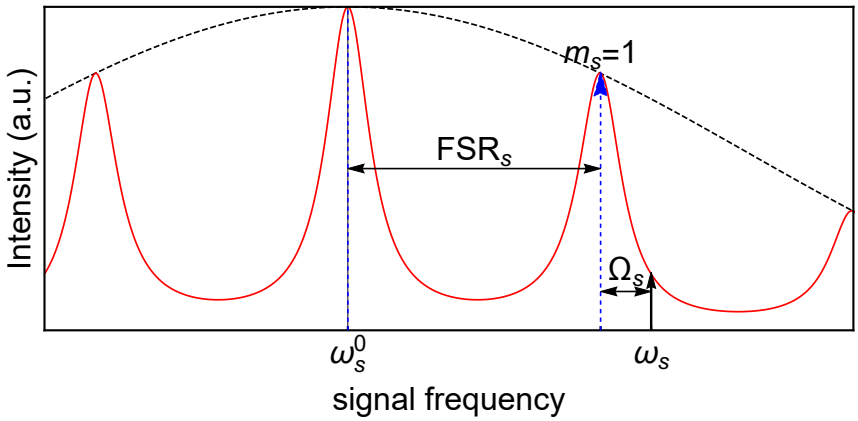


Figure 2.1: Variables describing the frequency of the signal photon from the CE-SPDC two-photon state. Black dashed line: phase matching efficiency for a free-space crystal, with maximum efficiency at $\omega_s^0$ and the corresponding partner idler frequency. Red solid line: CE-SPDC cavity resonances for the signal, weighted by the SPDC efficiency at that frequency. The amplitude/intensity for generating a photon at frequency $\omega_s$ in our notation is the same as that for generating a photon at frequency $\omega_s^0 + m_s \mathrm{FSR}_s + \Omega_s$ in the notation of Scholz et al.

The two-photon state from CE-SPDC, after a long interaction time is (equation 7 from [102])

$$
\begin{aligned}
|\psi_C\rangle \;=\; & \sum_{m_s=-\infty}^{\infty} \sum_{m_i=-\infty}^{\infty} \int_{-\infty}^{\infty} d\Omega_s \int_{-\infty}^{\infty} d\Omega_i \, \frac{\pi\alpha\sqrt{\gamma_s\gamma_i}\, F_{m_s,m_i}(\Omega_s,\Omega_i)}{(\frac{\gamma_s}{2} - i\Omega_s)(\frac{\gamma_i}{2} - i\Omega_i)} \\
& \times \delta(\omega_p - \omega_s^0 - \omega_i^0 - m_s \mathrm{FSR}_s - \Omega_s - m_i \mathrm{FSR}_i - \Omega_i) \\
& \times \hat{a}_s^\dagger(\omega_s^0 + m_s \mathrm{FSR}_s + \Omega_s)\, \hat{a}_i^\dagger(\omega_i^0 + m_i \mathrm{FSR}_i + \Omega_i)\, |0,0\rangle\,, \qquad (2.23)
\end{aligned}
$$

where $\omega_s^0$ and $\omega_i^0$ are the centre frequencies of two cavity modes for signal and idler, respectively. $\omega_p$, $\omega_s^0$ and $\omega_i^0$ satisfy energy conservation and perfect phase matching in the crystal. $m_s$ and $m_i$ are mode indices of the resonator modes for the signal and idler fields respectively. $\Omega_s$ and $\Omega_i$ are signal idler frequency detunings relative to the centres of the lines at $\omega_s^0 + m_s$ FSR$_s$ and $\omega_i^0 + m_i$ FSR$_i$ respectively (see Figure 2.1).

In Equation 2.23, $F_{m_s,m_i}$ is the phase matching function for the crystal in free space,

$$\begin{aligned} F_{m_s,m_i}(\Omega_s,\Omega_i) \quad = \quad & \operatorname{sinc}\left[\frac{l}{2c}\left\{(m_s FSR_s+\Omega_s)\left(n_s(\omega_s^0)+\omega_s^0\frac{\partial n_s(\omega_s)}{\partial\omega_s}\bigg|_{\omega_s=\omega_s^0}\right)\right.\right. \\ & \left.\left.+(m_i FSR_i+\Omega_i)\times\left(n_i(\omega_i^0)+\omega_i^0\frac{\partial n_i(\omega_i)}{\partial\omega_i}\bigg|_{\omega_i=\omega_i^0}\right)\right\}\right] \\ & \times\exp\left[\frac{il}{2c}\left\{(m_s FSR_s+\Omega_s)\right.\right. \\ & \times\left(n_s(\omega_s^0)+\omega_s^0\frac{\partial n_s(\omega_s)}{\partial\omega_s}\bigg|_{\omega_s=\omega_s^0}\right)+(m_i FSR_i+\Omega_i) \\ & \left.\left.\times\left(n_i(\omega_i^0)+\omega_i^0\frac{\partial n_i(\omega_i)}{\partial\omega_i}\bigg|_{\omega_i=\omega_i^0}\right)\right\}\right]. \end{aligned} \tag{2.24}$$

$\alpha$ is related to $\chi^{(2)}(\omega_p;\omega_i^0,\omega_i^0)$- the crystal efficiency for the nonlinear conversion of $\omega_p$ to $\omega_s^0$ and $\omega_i^0$ and to the maximum amplitude of the pump $E_p$ according to

$$\alpha=\frac{-iE_p}{16\pi^2\epsilon_0 cA}\chi^{(2)}(\omega_p;\omega_s^0,\omega_i^0)\sqrt{\frac{\omega_s^0\,\omega_i^0\,FSR_s FSR_i}{n_s(\omega_s)\,n_i(\omega_i)}}. \tag{2.25}$$

Here $A$ is the transverse quantisation area in the material, $\epsilon_0$ is the permittivity of free space and other variable definitions remain unchanged.

We simplify these expressions. The time evolved two-photon state is calculated using the time evolution operator, which is a function of the interaction Hamiltonian describing the nonlinear process. Since the SPDC can occur at any point within the nonlinear crystal, the Hamiltonian involves an integral along the length of the crystal to integrate over all the contributions. Scholz et al. set the end of the crystal as the origin an set the limits of the integral to go from $-l$ to $0$. In addition, they normalise it by $l$ ( section 3. in [102]). However, setting the origin to be in the middle of the crystal by changing the integration limits to $-l/2$ to $l/2$, and removing the normalisation will lead to the phase term $\exp[\cdots]$ in Equation 2.24 to be replaced by $l$. Since $\omega_p=\omega_s^0+\omega_i^0$ by definition, the $\delta$ function in Equation 2.23 implies $m_s\,FSR_s+\Omega_s=-(m_i\,FSR_i+\Omega_i)$. Applying this to (2.24) and using the results of subsubsection 2.1.2, Equation 2.24 can be simplified to

$$F'_{m_s,m_i}(\Omega_s,\Omega_i)=l\operatorname{sinc}\left[(m_s FSR_s+\Omega_s)\frac{\tau_o}{2}\right]. \tag{2.26}$$

Although Equation 2.23 can be used to obtain the amplitude for the production of a signal-idler photon-pair at some frequencies $\omega_s$ and $\omega_i$ respectively, the notation used by Scholz et al. requires $\omega_s$ and $\omega_i$ to be expressed in terms of the deviations ($\Omega_s$ and $\Omega_i$) from some cavity resonance ($m_s\mathrm{FSR}_s$ and $m_i\mathrm{FSR}_i$) Figure 2.1. In order to express the JSA directly as a function of some absolute frequencies of signal-idler emission $\omega_s$ and $\omega_i$, we simplify their results and change the notation. We define

$$\omega_\epsilon \equiv \omega_\epsilon^0 + m_\epsilon\,\mathrm{FSR}_\epsilon + \Omega_\epsilon \tag{2.27}$$

where $\epsilon \in \{s, i\}$. Applying Equation 2.27 to the two-photon state in Equation 2.23 and to the phase matching function in Equation 2.26, the two-photon state from CE-SPDC can be expressed as

$$\begin{aligned}|\psi_C\rangle = \alpha' \int_{-\infty}^{\infty} d\omega_s \int_{-\infty}^{\infty} d\omega_i\; f_{NB}(\omega_s, \omega_i) \\ \times \Gamma(\omega_s, \gamma_s, \omega_s^0, \mathrm{FSR}_s)\;\Gamma(\omega_i, \gamma_i, \omega_i^0, \mathrm{FSR}_i)\;\hat{a}_s^\dagger(\omega_s)\,\hat{a}_i^\dagger(\omega_i)\,|0,0\rangle\,.\end{aligned} \tag{2.28}$$

Here $f_{NB}$ is the JSA for SPDC from the crystal in free space, when pumped by a monochromatic pump,

$$f_{NB}(\omega_s, \omega_i) = \pi l\,\delta(\omega_p - \omega_s - \omega_i)\;\mathrm{sinc}\left[\left(\omega_s^0 - \omega_s\right)\frac{\tau_o}{2}\right]. \tag{2.29}$$

This expression, given in terms of the propagation delay, is equivalent to the one in Equation 2.7. $\Gamma$ is a sum of unit-amplitude complex Lorentzian functions and describes the frequency dependent transmission of an optical electric field through a cavity [104]

$$\Gamma(\omega_\epsilon, \gamma_\epsilon, \omega_\epsilon^0, \mathrm{FSR}_\epsilon) \equiv \sum_{m_\epsilon=-\infty}^{\infty} \frac{\gamma_\epsilon/2}{\frac{\gamma_\epsilon}{2} + i\left(\omega_\epsilon^0 + m_\epsilon\,\mathrm{FSR}_\epsilon - \omega_\epsilon\right)} \tag{2.30}$$

for $\epsilon \in \{s, i\}$. The constant $\alpha'$ is

$$\alpha' \equiv \alpha \frac{2}{\sqrt{\gamma_s}} \frac{2}{\sqrt{\gamma_i}}, \tag{2.31}$$

and has been brought out of the integral since it varies slowly over the range of signal-idler frequencies that are within the phase matching bandwidth.

Thus, the JSA for a two-photon state from CE-SPDC is a product of the JSA for single-pass SPDC in a free-space crystal and cavity resonances for the signal and idler,

$$f_C(\omega_s, \omega_i) \equiv f_{NB}(\omega_s, \omega_i)\;\Gamma(\omega_s, \gamma_s, \omega_s^0, \mathrm{FSR}_s)\;\Gamma(\omega_i, \gamma_i, \omega_i^0, \mathrm{FSR}_i). \tag{2.32}$$

### *JSI of photon pairs from CE-SPDC*

Similar to Equation 2.8, the square magnitude of the two-photon state is

$$\begin{aligned}
\langle\psi_C|\psi_C\rangle &= |\alpha'|^2 \int_{-\infty}^{\infty} d\omega_s \int_{-\infty}^{\infty} d\omega_i \, |f_{NB}(\omega_s,\omega_i)|^2 \\
&\quad \times \sum_{m_s=-\infty}^{\infty} \frac{\gamma_s^2/4}{\left(\frac{\gamma_s}{2}\right)^2 + (\omega_s^0 + m_s\,\mathrm{FSR}_s - \omega_s)^2} \\
&\quad \times \sum_{m_i=-\infty}^{\infty} \frac{\gamma_i^2/4}{\left(\frac{\gamma_i}{2}\right)^2 + (\omega_i^0 + m_i\,\mathrm{FSR}_i - \omega_i)^2} \\
&= |\alpha'|^2 \int_{-\infty}^{\infty} d\omega_s \int_{-\infty}^{\infty} d\omega_i \, |f_{NB}(\omega_s,\omega_i)|^2 \\
&\quad \times |\Gamma(\omega_s,\gamma_s,\omega_s^0,\mathrm{FSR}_s)|^2 \, |\Gamma(\omega_i,\gamma_i,\omega_i^0,\mathrm{FSR}_i)|^2 \\
&\equiv |\alpha'|^2 \int_{-\infty}^{\infty} d\omega_s \int_{-\infty}^{\infty} d\omega_i \, |f_C(\omega_s,\omega_i)|^2, \qquad (2.33)
\end{aligned}$$

which is an integral of the JSI from CE-SPDC $|f_C(\omega_s,\omega_i)|^2$ over all signal-idler frequencies. Thus $|f_C(\omega_s,\omega_i)|^2$, which is proportional to the probability density for the distribution of signal-idler frequencies from CE-SPDC, is a product of the phase-matching function (the $\mathrm{sinc}^2$ function), and the individual signal and idler cavity resonance functions. The cavity resonances are given by a Lorentzian for each centred at $\omega_\epsilon^0 + m_\epsilon \mathrm{FSR}_\epsilon$ and a FWHM in angular frequency $\gamma_\epsilon$ for $\epsilon \in \{s,i\}$. Thus the output spectrum consists of those signal-idler frequencies that are within the phase matching bandwidth for the crystal in free space and are simultaneously resonant in the CE-SPDC cavity.

The form of the cavity-modified JSI from Equation 2.33 is similar to the expression for the CE-SPDC JSI developed by Jeronimo-Moreno *et al.* in [103] (equation 10). The derivation in [103] holds for a lossless standing-wave cavity. When modified to be applicable to all types of cavities in general by including losses [95, section 1.3.2] and multiple mirror reflectivities, the pair JSI takes the form

$$|f'_C(\omega_s,\omega_i)|^2 = |f(\omega_s,\omega_i)|^2 \mathcal{A}_s(\omega_s)\mathcal{A}_i(\omega_i), \qquad (2.34)$$

where

$$\begin{aligned}
\mathcal{A}_\epsilon(\omega_\epsilon) &= \frac{T_{oc}}{(1-g_{rt})^2}\left[1 + \left(\frac{2\mathcal{F}}{\pi}\right)^2 \sin^2\left(\pi\frac{\omega_\epsilon}{\mathrm{FSR}_\epsilon}\right)\right]^{-1} \\
&\equiv T_{enh}\mathcal{A}_\epsilon^0(\omega_\epsilon), \qquad (2.35)
\end{aligned}$$

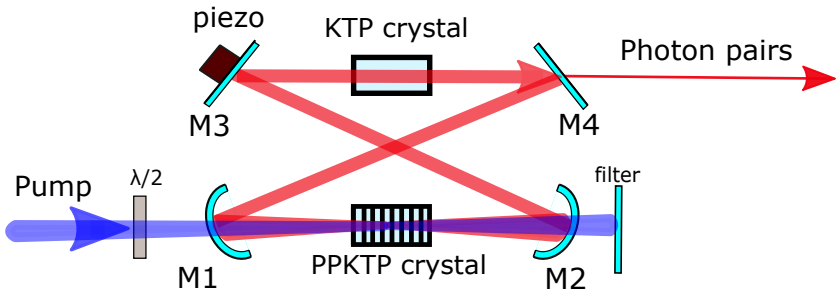


Figure 2.2: Schematic of CE-SPDC source. Pump at 397.5 nm (blue line) is focussed in the SPDC crystal (PPKTP) inside a bow-tie cavity. The down-converted light at 795 nm (red line) is resonant in the cavity, which also contains a tuning crystal (KTP), and the down-converted photons exit via mirror M4. The detectors PD1 and PD2 are used to probe the cavity resonances at idler and signal polarisations respectively, with the weak transmission of coherent light through M2 (dash-dotted line). The piezo on M3 stabilises the cavity length. PBS: polarising beamsplitter, PD: photodiode, λ/2: half-wave plate

for $\epsilon \in \{s, i\}$. Here $T_{oc}$ (transmittivity of the out-coupling mirror) = $1 - R_{oc}$ (reflectivity of the out-coupling mirror), $g_{rt}$ (the round trip gain) and $\mathcal{F}$ (cavity Finesse) are attributes of a cavity, details of which are given in subsection 2.2.2. $\mathcal{A}^0_\epsilon(\omega_\epsilon) \equiv \left[1 + \left(\frac{2\mathcal{F}}{\pi}\right)^2 \sin^2\left(\pi \frac{\omega_\epsilon}{\mathrm{FSR}_\epsilon}\right)\right]^{-1}$ is the unit-amplitude normalised Airy function and $T_{enh} \equiv T_{oc}/(1 - g_{rt})^2$ is the cavity enhancement factor.

## 2.2 DETAILS OF THE PHOTON-PAIR SOURCE

Having theoretically analysed the joint spectrum of the two-photon state from CE-SPDC we now describe the photon-pair source, which is based on the same process. First we describe the design of our CE-SPDC source. We then introduce essential attributes of cavities and state experimental measures of these attributes for our cavity. Parts of this section and subsequent sections appear in [68].

### 2.2.1 Design

The schematic of the CE-SPDC source is given in Figure 2.2. The CE-SPDC optical resonator is in a bow-tie configuration of four mirrors, with the two closest to the SPDC crystal being concave, to produce a cavity mode with a 45 µm beam waist inside the SPDC crystal. Mirrors M1 to M3 are coated for 99.9 % reflectivity at 795 nm ($R_1, R_2, R_3 = R_{HR} = 99.9\,\%$) whereas the outcoupling mirror M4 has nominal reflectivity of ($R_{oc}$) 93 % at this wavelength. Scattering losses from the super-polished, ion-beam sputtered mirrors are negligible, and the weak transmission of M1, M2 and M3 is useful for locking and probing the cavity resonances. The cavity length can be adjusted via a piezo-electric actuator on mirror M3. These four mirrors form a resonator for the 795 nm signal and idler photons. The 397 nm pump light is not resonated because the same mirror coatings are largely transparent for this wavelength with nominal reflectivities of $< 3\%$ at 397 nm. The effective cavity length is 610 mm. See F. Wolfgramm et al. [37], and [105] for more details of the cavity construction.

The SPDC occurs in a 20 mm long periodically-poled (or quasi-phase-matched) potassium titanyl phosphate (PPKTP) crystal (henceforth called SPDC crystal), with a poling period of 9.4 µm to enable type-II phase matching from vertically-polarised (V) pump to vertically-polarised signal and horizontally-polarised (H) idler beams. The crystal phase-matching bandwidth was calculated to be $\Delta\omega_{spdc} = 2\pi\times$ 148 GHz [105] at this wavelength.

The pump is focused into the SPDC crystal, enters the cavity via M1, exits through M2 and is blocked. The optimal pump waist was calculated to be 22.5 µm from the Boyd-Kleinman theory [105]. However, to reduce the effects of thermal lensing, a waist of 42 µm was chosen. The pump alignment is discussed in section 2.3.

The cavity also contains an unpoled KTP crystal (tuning crystal) with the same dimensions as the PPKTP crystal and with the optical axis aligned parallel to that of the PPKTP crystal. The birefringence of the tuning crystal alters the round-trip optical path length of the signal relative to the idler and thereby provides a degree of freedom for independently tuning the signal and idler cavity resonances. This is explained in detail in chapter 4 which is dedicated to tuneability.

Both the SPDC and tuning crystals are mounted in PTFE (Teflon) ovens with optical access. The crystals' temperatures are independently controlled using Peltier elements and 5 kΩ NTC thermistors, with the controllers being an analog PID (Wavelength

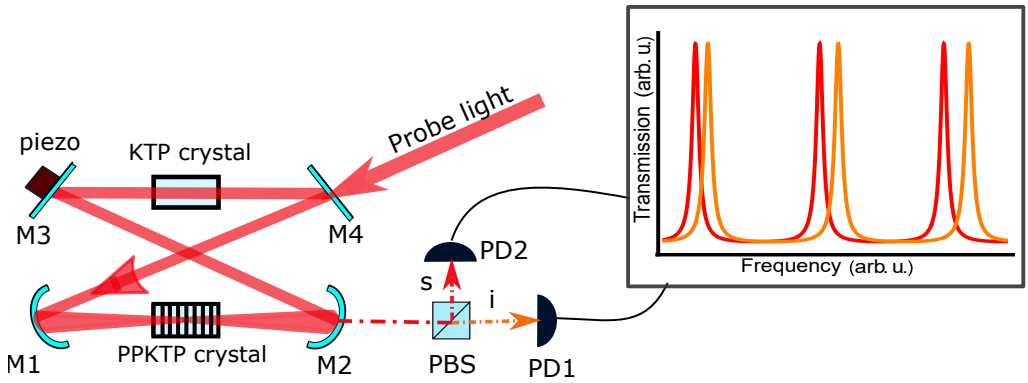


Figure 2.3: Schematic of set-up for measurements of cavity attributes. Frequency scanned diagonally polarised coherent light at 795 nm is incident through M4. The weak transmission of the coherent light through M2 (dash-dotted line), is split according to polarisation at the PBS. Detectors PD1 and PD2 are used to probe the cavity resonances at idler and signal polarisations respectively. Inset: Illustrative image of transmission seen on oscilloscope for V polarised (red curve) and H polarised (orange curve) probe light. PBS: polarising beamsplitter, PD: photodiode.

Electronics HTC1500) with its set point fixed by a microcontroller (Arduino Uno + Analog Shield). This technique allows us to control the temperature in steps of $\approx 5$ mK and a provides a long-term stability of of 1 mK in the crystal temperature.

### 2.2.2 Attributes of the bow-tie cavity

Here we define some parameters important to describe a cavity and provide measures of these values for our CE-SPDC cavity. Since we use a bow-tie cavity with a single out-coupling mirror for our CE-SPDC process, this discussion is made specific to such a cavity. As in the theory sections, we use subscripts p, s and i, to refer to physical quantities pertaining to the pump, signal and idler respectively. The definitions of the following attributes are taken from [106].

- **Free spectral range**
  The frequency spacing between adjacent frequencies that are perfectly resonant in the cavity. This depends on the effective path length experienced by light within the resonator. Since the cavity contains birefringent media, the free spectral range depends on the length ($l_j$) of each material within the resonator (indexed with

subscript - j) and the polarisation ($\hat{e}$) dependent group index in that medium $n^{(g)}_{l,\hat{e}}$ according to

$$\mathrm{FSR}_\epsilon = \frac{2\pi c}{\sum_j n^{(g)}_{j,\hat{e}}(\omega_\epsilon, T_j)\, l_j}. \tag{2.36}$$

where $\epsilon \in \{s, i\}$ and $\hat{e} \in \{V, H\}$[5]. $n^{(g)}_{j,\hat{e}}(\omega_\epsilon, T_j)$ is also dependent on the temperature $T_j$ of the material and so the FSR can be altered by adjusting the temperature of the crystals inside the cavity.

The FSRs of the signal and idler modes are slightly different due to the birefringence induced difference in optical path length between them. To make a classical measurement of the cavity FSR, we perform cavity transmission spectroscopy. We scan the frequency of a 795 nm distributed Bragg reflector (DBR) laser, which enters the cavity via M4 and is detected behind M2 in a photo detector. We simultaneously collect Rb $D_1$ saturated absorption spectra as an absolute frequency reference. We compare the spacing between adjacent cavity resonances and the features in the absolute reference to estimate the FSR (Figure 2.3). We match the polarisation of the light from the DBR laser to the signal/idler modes to obtain the corresponding FSR. From this we estimated a mean FSR,

$$\mathrm{FSR}_{\mathrm{mean}} \equiv \frac{\mathrm{FSR}_s + \mathrm{FSR}_i}{2} = 2\pi \times 496(8)\,\mathrm{MHz}. \tag{2.37}$$

The difference $\Delta\mathrm{FSR} \equiv \mathrm{FSR}_s - \mathrm{FSR}_i = 2\pi \times 3.5(1)\,\mathrm{MHz}$ can be more precisely estimated by analysing the spectral content at the output of the CE-SPDC source as will be shown later.

- **Round trip time**
  The time taken by light to complete one round trip through the cavity. The round trip time is related to the FSR according to

$$\tau_{rt} = \frac{2\pi}{\mathrm{FSR}}. \tag{2.38}$$

  $\tau_{rt} \approx 2\,\mathrm{ns}$ in our cavity.

- **Round trip gain and loss**
  The magnitude of the cavity (round trip) gain ($g_{rt}$) gives the change in the ampli-

5 Note: Throughout the thesis, the FSR is in units of angular frequency.

tude of the field within the cavity after one round trip. For a passive cavity $g_{rt} < 1$.

$$g_{rt} = \sqrt{R_1 R_2 R_3 R_{oc}}\, e^{-\sum_j \alpha_j l_j}, \tag{2.39}$$

where $e^{-\alpha_j l_j}$ is the amplitude reduction due to loss through each medium (indexed with j) of length $l_j$ and with a voltage absorption co-efficient $\alpha_j$ within the cavity. The probability that a photon is lost in one round trip through a loss channel other than the out-coupling mirror is

$$P_{loss} = 1 - \frac{g_{rt}^2}{R_{oc}}. \tag{2.40}$$

From the cavity transmission spectroscopy measurements, we fit the the gain $g_{rt}$ to be $0.95 \pm 0.01$ and $P_{loss}$ to be $0.023 \pm 0.009$.

- **Cavity escape efficiency**
  The probability that a photon is out-coupled via outcoupling mirror as opposed to being transmitted or scattered out of the cavity mode otherwise. It is defined as [107]

$$\eta = \frac{1 - R_{oc}}{1 - g_{rt}^2}. \tag{2.41}$$

  We estimate an escape efficiency of 72% for our cavity.

- **Finesse**
  The finesse is a measure of the quality of the cavity and gives an estimate of the resolving power of a cavity when it is used as a frequency filter. It also gives an estimate of the number of round trips light makes in a cavity before it leaks out of the cavity. It is defined as

$$\mathcal{F} = \frac{\pi\sqrt{g_{rt}}}{1 - g_{rt}}. \tag{2.42}$$

  Based on the $g_{rt}$ we expect a finesse of 61 for the CE-SPDC cavity. But from the measurement of the cavity linewidth (see below) we estimate a finesse of 65. Since the signal and idler have approximately the same wavelength, the finesse, gain and losses in the cavity are the same for both.

- **Cavity linewidth**
  The cavity damping rate $\gamma$, also called the cavity relaxation rate, is the rate at which power decays from the cavity. It gives the spectral width, more precisely the FWHM width in angular frequency, of individual resonator modes.

$$\gamma \approx \frac{\mathrm{FSR}}{\mathcal{F}}. \tag{2.43}$$

  We repeat the cavity transmission spectroscopy measurement with an atomic reference, outlined earlier, to experimentally measure the linewidth. We observe transmission resonances of linewidth $8.8(4)\,\mathrm{MHz}$, which, when adjusted for the $1.2(5)\,\mathrm{MHz}$ short-term linewidth of the DBR laser, implies $\gamma = 2\pi \times 7.6(6)\,\mathrm{MHz}$. The resolution of the technique was not sufficient to resolve a difference between the decay rates for the signal and idler modes.

- **Ring Down Time**
  The ring down time $\tau_d$ is the inverse of the linewidth and gives the time after which the energy in the cavity drops to $1/e$ of the original value. It can also be called the cavity decay time.

$$\tau_d = \frac{1}{\gamma}. \tag{2.44}$$

  It is $21\,\mathrm{ns}$ for our cavity.

## 2.3 PHASE-MATCHING TEMPERATURE IDENTIFICATION

We performed SHG of laser light at $795\,\mathrm{nm}$ within the CE-SPDC cavity to identify the temperature at which perfect phase matching is achieved at the required signal-idler frequencies. For this, a frequency stabilised, diagonally polarised, coherent light at $795\,\mathrm{nm}$ was injected into the down-conversion cavity through the outcoupling mirror as shown in Figure 2.4. The temperature of the tuning crystal was adjusted such that the cavity was resonant to both $H$ and $V$ polarisations at the the same frequency, thus the diagonally polarised input light could excite both modes in the cavity simultaneously. The cavity length was stabilised to maintain resonance. The temperature of the PPKTP crystal was changed and for each temperature value, a detector outside the cavity (PD4 in Figure 2.4) measured the power of the generated second-harmonic at $397.5\,\mathrm{nm}$. Since the SPDC crystal is quasi-phase-matched, the power of blue light generated from SHG

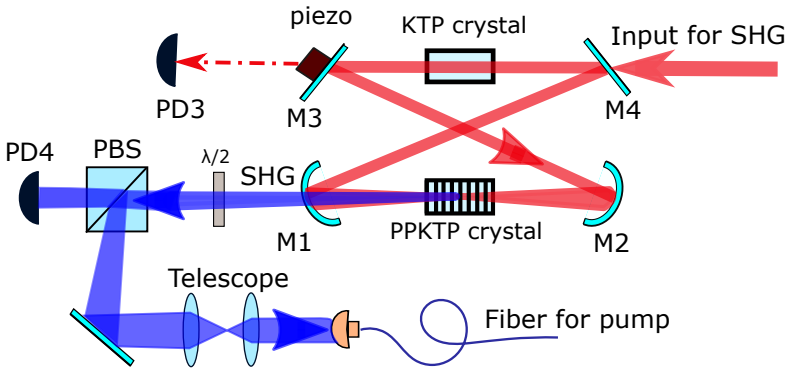


Figure 2.4: Schematic of set-up for SHG in cavity. Frequency stabilised, diagonally polarised coherent light at 795 nm is incident through M4. The weak transmission of the coherent light through M3 (dash-dotted line), is detected on PD3 and the piezo actively stabilises the cavity length to ensure maximum signal on PD3. The SHG generated is detected on PD4 and is used to align the optics for the pump.

follows a $\text{sinc}^2$ function of the SPDC crystal's temperature as shown in Figure 2.5. The measurements were performed with 7 $mW$ injected before the outcoupling mirror ($P_{in}$). The maximum power of blue light produced was 105 $\mu W$. Based on the measured cavity gain and loss values, we estimate the intra-cavity power to be $P_{cav} = 32 \pm 6 \times P_{in} \approx 224\ mW$ on resonance. The crystal's conversion efficiency is thus $\eta_{SHG} \equiv P_{SHG}/P_{cav}^2 = 0.21\ \%W^{-1}$.

Besides identifying the temperature for degenerate phase matching, we used the SHG process to align the pump to the SPDC crystal by optimising the coupling of the upconverted blue light into the fibre that later is used to direct pump light into the crystal for the CE-SPDC process.

## 2.4 ATTRIBUTES OF THE CE-SPDC OUTPUT

From the cavity-modified two-photon JSA (Equation 2.32) it is evident that multiple factors affect the spectrum of the down-converted photons. Only those signal-idler frequencies that 1) satisfy energy conservation with the pump, 2) fall within the phase matching function and 3) simultaneously satisfy their individual resonance conditions within the cavity, will have a non-negligible amplitude of generation. The consequences of this for the signal-idler joint spectrum are discussed here.

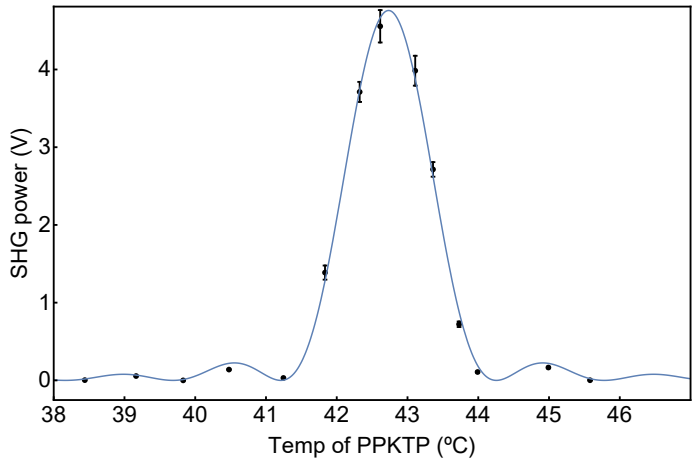


Figure 2.5: Second Harmonic Generation in CE-SPDC cavity. The PPKTP crystal temperature is scanned to identify the temperature for optimal phase-matching. Data agrees with the $\text{sinc}^2$ fit function

- **Two-photon linewidth**
  The condition of simultaneous signal-idler resonance implies that the spectrum of one of the down-converted photons is not just governed by its own damping within the cavity but also by the damping rate of its correlated partner. In [102] it has been shown that, for a monochromatic pump, the individual spectrum of the signal or idler from CE-SPDC is described by a comb of longitudinal modes with a FWHM that is smaller than the cavity damping rate at the frequency of the signal ($\gamma_s$) and the idler ($\gamma_i$). The linewidths of the signal and idler from CE-SPDC with a monochromatic pump, are equal and are called the two-photon linewidth. When $\gamma = \gamma_s \approx \gamma_i$ , the two-photon linewidth is [32, 102]

$$\gamma_{tp} = \gamma\sqrt{\sqrt{2}-1} \approx 0.64\,\gamma. \tag{2.45}$$

  Using the cavity damping rate from subsection 2.2.2 in Equation 2.45, a photon from our source is expected to have a linewidth of $2\pi\times 4.9(4)$ MHz. This is similar to the $2\pi\times$ 5.75 MHz natural linewidth of the $D_1$ transition in Rb. We verify this through correlation measurements discussed in chapter 5.

- **Photon-pair escape probability**
  The pair escape probability gives the probability that both photons in a pair exit

through the outcoupling mirror and are not lost through some other loss channel. The pair escape probability is the product of the individual escape probabilities for the signal and idler [107]. If the mirror reflectivities and round trip loses are the same for both down-converted photons,

$$\eta_{pair} = \eta_s \eta_i = \left( \frac{1 - R_{oc}}{1 - g_{rt}^2} \right)^2, \tag{2.46}$$

where $\eta_{s/i}$ is the cavity escape efficiency for the signal/idler given in Equation 2.41. In our case $\eta_{pair} = 52\%$.

- **Cavity enhancement of brightness**
  The brightness of the down-converted pairs that are resonant in the CE-SPDC cavity is enhanced by the Purcell effect [34]. In the earliest quantum description of CE-SPDC, Ou and Lu had calculated the brightness enhancement factor per mode in the CE-SPDC output, by comparing the brightness of all frequencies within the FWHM of a CE-SPDC tooth with the total brightness from a filtered single-pass SPDC process. They report an overal enhancement factor per mode of $\mathcal{F}^3/2\,\mathcal{F}^0$ in [32] and $\mathcal{F}^3/\pi\mathcal{F}^0$ [99]. These apply to both type-I and II down-conversion processes, provided the losses in the CE-SPDC cavity for the down-converted fields are the same. Here $\mathcal{F}_0$ is the finesse of the "loss-less cavity" i.e., the finesse for the same value of $R_{oc}$ but all other mirrors are perfectly reflective and there are no more losses, making $g_{rt} = \sqrt{R_{oc}}$ and $P_{loss} = 0$.

  The model developed by Jeronimo-Moreno et al. to describe CE-SPDC, gives the brightness-enhancement at signal-idler frequencies that are in the centre of the cavity-resonance. The factor $T_{enh}^2$ in equation 2.34 gives the amplification in brightness at signal-idler frequencies perfectly resonant in the cavity i.e., where the Airy functions $\mathcal{A}_s^0 = \mathcal{A}_i^0 = 1$. From the detailed analysis in [95, See section 1.3.2], for a cavity finesse $\gtrsim 10$,

$$\begin{aligned} T_{enh}^2 &= \left( \frac{T_{oc}}{(1 - g_{rt})^2} \right)^2 \\ &\approx \frac{4}{\pi^2} \left( \frac{\mathcal{F}^2}{\mathcal{F}_0} \right)^2. \end{aligned} \tag{2.47}$$

  While Scholz et al. did not provide an explicit expression for the brightness enhancement, this can be easily calculated from their expression for the two-photon state. For this, we compare the JSA for perfectly-resonant frequencies $\omega_s^0$,

$\omega_i^0$, assumed to satisfy energy conservation $\omega_s^0 + \omega_i^0 = \omega_p$, for the CE-SPDC and single-pass scenarios. The state produced by CE-SPDC is given in Equation 2.28, while that for single-pass generation is given in Equation 2.7. We note that at perfect resonance, the mode-shape factors appearing in Equation 2.28 are $|\Gamma(\omega_i^0, \gamma_i, \omega_i^0, \mathrm{FSR}_i)| \approx |\Gamma(\omega_s^0, \gamma_s, \omega_s^0, \mathrm{FSR}_i)| \approx 1$ in the high-finesse regime, so that in fact Equation 2.28 and Equation 2.7 differ only in that Equation 2.28 contains the global factor $\alpha'$, whereas Equation 2.28 contains the global factor $\kappa$. The ratio of brightnesses is thus $|\alpha'/\kappa|^2$.

$\kappa$ is given in Equation 2.3 and $\alpha'$ is given by Equation 2.31 and Equation 2.25. $\alpha'$ can also be expressed as

$$\begin{aligned} \alpha' &= i\frac{\chi^{(2)}}{2\hbar} E_p \mathcal{E}_s \mathcal{E}_i \sqrt{\frac{\mathrm{FSR}_s \mathrm{FSR}_i}{\gamma_s \gamma_i}} \frac{2}{\pi} \\ &\approx i\frac{\chi^{(2)}}{2\hbar} E_p \mathcal{E}_s \mathcal{E}_i \sqrt{\mathcal{F}_s \mathcal{F}_i} \frac{2}{\pi}, \end{aligned} \tag{2.48}$$

where the field amplitudes $\mathcal{E}_s$ and $\mathcal{E}_i$ are defined in Equation 2.4.

In our case $\mathcal{F}_s = \mathcal{F}_i = \mathcal{F}$. Taking the ratio of Equation 2.48 and Equation 2.3 we find

$$\left|\frac{\alpha'}{\kappa}\right| \approx \frac{2}{\pi}\mathcal{F}. \tag{2.49}$$

Thus the enhancement in intensity from the CE-SPDC process (for a signal-idler pair that is perfectly resonant in the cavity) scales as the square of the finesse according to

$$\left|\frac{\alpha'}{\kappa}\right|^2 \approx \frac{4}{\pi^2}\,\mathcal{F}^2 \tag{2.50}$$

We note that this is approximately equal to the enhancement from Jeronimo-Moreno et al. and gives the enhancement at the peak (the line centre) of the cavity resonances. From these we estimate a brightness enhancement of $\sim 1000$ for a signal-idler pair perfectly resonant in the cavity, as compared to the same pair of frequencies from a single pass SPDC process. We also note that Equation 2.50 describes the brightness enhancement at the specific frequency values $\omega_s = \omega_s^0$, $\omega_i = \omega_i^0$, while the two-photon linewidth decreases with increasing finesse so that the total brightness contained within a CE-SPDC mode pair increases with $\mathcal{F}$, but more slowly than $\mathcal{F}^2$.

## 2.5 THE CLUSTERING EFFECT

Unless specific compensation measures are taken [37], a type-II SPDC cavity will have $\mathrm{FSR}_s \neq \mathrm{FSR}_i$, due to birefringence of the nonlinear media. This FSR mismatch provides a means to restrict the modes into which photon pairs are generated. For example, if a signal frequency $\omega_s^{(0)}$ and its energy-conserving partner $\omega_i^{(0)} = \omega_p - \omega_s^{(0)}$ are both perfectly resonant, i.e., if $\omega_s^{(0)} = l\,\mathrm{FSR}_s$ and $\omega_i^{(0)} = m\,\mathrm{FSR}_i$ for some integers $l$ and $m$, then the frequency of the neighboring signal mode $\omega_s^{(1)} = \omega_s^{(0)} + \mathrm{FSR}_s$ will be resonant, but its energy-conserving partner $\omega_i^{(1)} = \omega_i^{(0)} - \mathrm{FSR}_s$ will not be perfectly resonant as the resonance will be centred at $\omega_i^{(0)} - \mathrm{FSR}_i$. While it is possible to avoid emission on neighboring modes by making the FSR mismatch, $\Delta\mathrm{FSR} \equiv \mathrm{FSR}_s - \mathrm{FSR}_i$, large compared to the linewidth [107, 108], if $|\Delta\mathrm{FSR}| \lesssim \gamma$, there will be significant emission into at least a few mode pairs close to any ideally-matched pair. This gives rise to the **"clustering effect"** [107–110]. The output of the CE-SPDC is in clusters of modes which repeat with a frequency spacing ($\Delta\omega_{\mathrm{cluster}}$) given by [109, see Eq. 25]

$$\Delta\omega_{\mathrm{cluster}} = \frac{\mathrm{FSR}_s\ \mathrm{FSR}_i}{|\Delta\mathrm{FSR}|}. \tag{2.51}$$

If there exists an energy-conserving mode pair $\omega_s^{(l)} = l\,\mathrm{FSR}_s$ and $\omega_i^{(m)} = m\,\mathrm{FSR}_i$ for some $l, n \in \mathbb{Z}$, it will be the brightest in the cluster. For an average signal-idler linewidth $\gamma_{\mathrm{avg}} = (\mathrm{FSR}_s + \mathrm{FSR}_i)/(2\mathcal{F}) \equiv \mathrm{FSR}_{\mathrm{mean}}/\mathcal{F}$, the modes $\nu_s^{(l+M)}$ and $\nu_i^{(m-M)}$, for $M \in \mathbb{Z}$, would have half the brightness of $\omega_s^{(l)}$ and $\omega_i^{(m)}$ if $M\,\Delta\mathrm{FSR} = \pm\gamma_{\mathrm{avg}}/(2)$. The same applies to the modes $\omega_i^{(l-M)}$and $\omega_i^{(m+M)}$. Thus we can expect the total number of modes within the FWHM of a cluster to be

$$N_m = 2M + 1 = \frac{\gamma}{2|\Delta\mathrm{FSR}|} = \frac{\mathrm{FSR}_{\mathrm{mean}}}{\mathcal{F}|\Delta\mathrm{FSR}|}. \tag{2.52}$$

In what follows, we theoretically estimate and experimentally verify the structure and spacing of clusters in the CE-SPDC output.

### 2.5.1 Theoretical modelling of CE-SPDC output

We use the Sellmeier coefficients for PPKTP from [111] and the cavity parameters to estimate the number of modes per cluster and cluster spacing. The Sellmeier's equations relate the refractive index $n$ at room temperature $T_r$ to the wavelength $\lambda$ according to

$$n_{\hat{e}}(\lambda, T_r) = \sqrt{1 + \sum_j \frac{B_{j,\hat{e}}\,\lambda^2}{\lambda^2 - C_{j,\hat{e}}}}. \tag{2.53}$$

Here $T$ is temperature and the coefficients $B_j, C_j$ take different values depending on the polarisation of the light ($\hat{e}$) w.r.t to the crystal axes. In our case, $\hat{e}$ refers to $V$ for signal and $H$ for idler. The rate of change in refractive index w.r.t temperature is reported in the following form as a polynomial fit to experimental data

$$\left.\frac{dn_{\hat{e}}(\lambda, T)}{dT}\right|_{T=T_r} = \sum_j \frac{D_{j,\hat{e}}}{\lambda^j}. \tag{2.54}$$

So that the temperature-dependent refractive index can be approximated as

$$n_{\hat{e}}(\lambda, T) = n_{\hat{e}}(\lambda, T_r) + \left.\frac{dn_{\hat{e}}(\lambda, T)}{dT}\right|_{T=T_r} (T - T_r). \tag{2.55}$$

The temperature and wavelength dependent group index is

$$n_{\hat{e}}^{(g)}(\lambda, T) = n_{\hat{e}}(\lambda_0, T) - \lambda \left[\left.\frac{\partial(n_{\hat{e}}(\lambda, T))}{\partial\lambda}\right|_{\lambda=\lambda_0}\right]. \tag{2.56}$$

The crystals in the nonlinear cavity are cut along the x- axis and the signal and idler photons are polarised along y and z axis respectively. We use the values of the coefficients in Equation 2.53 and Equation 2.54 from [111] and the expression for FSR from Equation 2.36 to theoretically calculate the signal-idler FSRs. We estimated a $|\Delta\text{FSR}| = 2\pi \times 3.5\,\text{MHz}$ from this. For modelling the JSI produced by the CE-SPDC, we used 148 GHz for the SPDC bandwidth, the classically measured $\text{FSR}_{\text{mean}} = 2\pi \times 496\,\text{MHz}$, $\gamma_i = \gamma_s = 2\pi \times 7\,\text{MHz}$ and the the estimated $\Delta\text{FSR}$ of $2\pi \times 3.5\,\text{MHz}$ in Equation 2.33 or equivalently in Equation 2.34, to plot the signal spectrum from the CE-SPDC source for a narrowband pump (i.e., setting $\omega_i = \omega_p - \omega_s$). The results are shown in figures Figure 2.6. From these calculations we estimated that there would be 3 clusters within the SPDC bandwidth, spaced by $\Delta\omega_{\text{cluster}} = 2\pi \times 68\,\text{GHz}$ from each other.

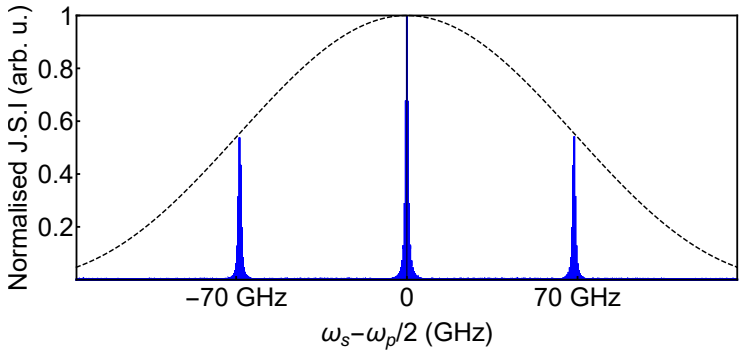


(a)

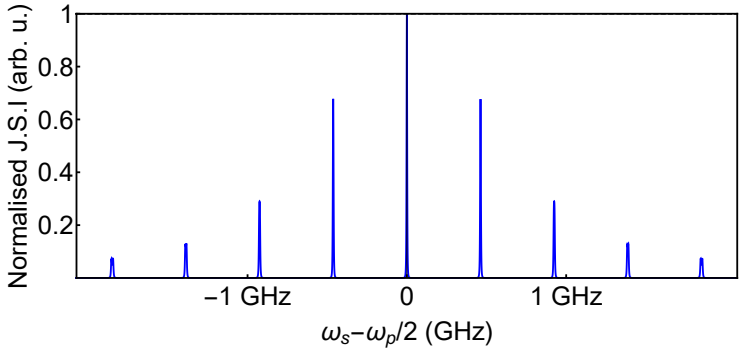


(b)

Figure 2.6: Theoretical two-photon JSI from CE-SPDC. The blue solid lines show the CE-SPDC JSI function $|f_C(\omega_s, \omega_p - \omega_s)|^2$ for a constant $\omega_p$. Black dashed line shows the crystal phase matching function with the crystal tuned such that the degenerate modes $\omega_i = \omega_s = \omega_p/2$, are brightest. See subsection 2.5.1 for the function parameters used for the plots. Top graph shows three clusters allowed within the phase matching bandwidth. Bottom graph shows closeup of the central cluster. Each cluster is expected to contain 3 modes within the FWHM.

### 2.5.2 Cluster analysis through DFG

It was important for us to know the exact structure of the clusters, in order to design a suitable filter for a single frequency-mode output. The theoretical predictions of the cluster structure are reasonably sensitive to the refractive index of the crystals, which may vary in function of the crystal growth methods. Rather than rely upon such

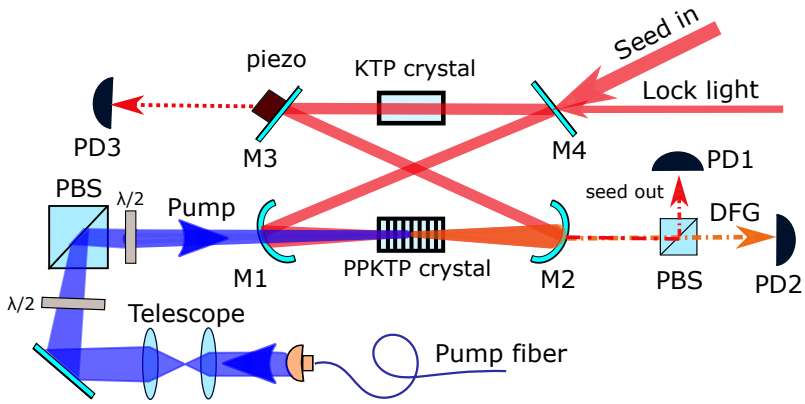


Figure 2.7: Schematic of set-up for DFG in cavity. Frequency stabilised, V polarised coherent light at 795 nm (lock light) is incident , counter-propagating to the pump, through M4. Its transmission (red dotted line) is detected in PD3, which is used to stabilise the cavity length. DFG occurs between a frequency-scanned high-power V polarised seed (also incident through M4) and the pump. The weak transmission of the H polarised DFG (orange dash-dotted line), is detected on PD2 and compared with the transmission of the seed (red dash-dotted line) seen in PD1.

predictions, we used the stimulated parametric down-conversion process, i.e. difference frequency generation (DFG), to measure the parametric gain of the CE-SPDC [112].

A schematic of the set-up is shown in Figure 2.7. A V polarised locking beam at frequency $\omega_{\text{lock}}$ (resonant to $F = 2$ to $F' = 1$ transition in $^{87}$Rb $D_1$ line) was made to enter the cavity in the reverse direction, i.e., opposite to the direction of the pump, signal and idler, and detected in transmission using PD3. The PPKTP crystal was pumped with about 19 mW of pump light with frequency $\omega_p = 2\omega_{\text{lock}} - 2\pi \times 120\,\text{MHz}$. About 28 mW of seed light at 795 nm, matched in spatial mode, polarisation and direction to the signal mode, was introduced through M4, as a seed for the DFG process. Light exiting the cavity through M2 was split by polarisation and detected at PD1 and PD2. The seed frequency ($\omega_{\text{seed}}$) was scanned, and DFG was observed as production of H-polarised idler light. Since the intensity of the seed changed with the frequency scan, we estimate the power of the DFG light generated based on the ratio of voltages recorded on PD2 (for the transmitted H-polarised DFG light) and PD1 (for the transmitted V polarised seed light). The ratio of DFG to seed powers was 0.044.

Figure 2.8 shows the detected idler power seen on PD2, as $\omega_{\text{seed}}$ was scanned by over a range of $\pm 2\pi \times 3$ GHz. The output shows a cluster of modes that contains about

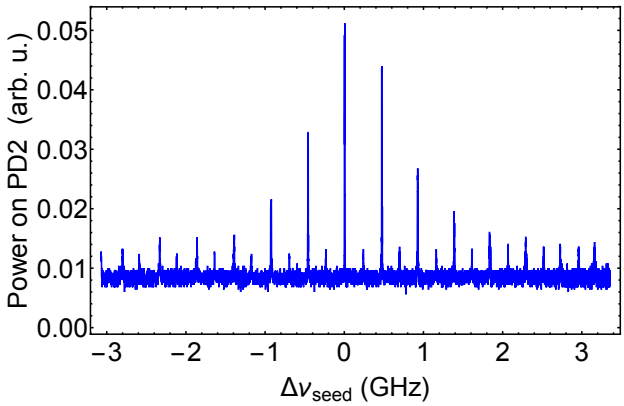


Figure 2.8: Measurement of one cluster of CE-SPDC emission by DFG. Graph shows idler power ($P_i$) generated by DFG, as a function of the change in the input seed frequency ($\Delta\nu_{seed}$), for fixed cavity length and pump frequency. Here, $2\pi \times \Delta\nu_{seed} \equiv \omega_{seed} - \omega^0_{seed}$, where $\omega^0_{seed}$ is the angular frequency of the seed that corresponds to the brightest peak in the idler cluster in graph. This is due to the simultaneous resonance of $\omega^0_{seed}$ and the idler mode at $\omega_p - \omega^0_{seed}$ in the CE-SPDC cavity. Other peaks from idler modes at $\pm\,FSR_i, \pm 2\,FSR_i, \ldots$ have decreasing brightness according to the mismatch in resonance with the corresponding seed modes $2\pi \times \Delta\nu_{seed} = \pm\,FSR_s, \pm 2\,FSR_s, \ldots$ perfectly resonant in the cavity as the cavity lock light has the same polarisation as the seed light. A second set of peaks, intermediate between DFG peaks and of roughly constant amplitude, appear to be due to a small coupling of the seed beam to a higher transverse mode, and are unrelated to DFG. Background level of $P_i \approx 0.008$ is due to imperfect blocking of the pump light.

3 to 4 modes within the FWHM of the cluster. The first cluster was observed when $\omega_{seed}$ was scanned around $2\pi\times$ 377 099.1(5) GHz, as measured with a wavemeter. The cluster repeated itself with a period of $2\pi\times$ 70.7(5) GHz in $\omega_{seed}$. From Equation 2.51 with $FSR_{mean} = 2\pi\times$ 496 MHz and $\omega_{cluster} = 2\pi\times$70.7 GHz, we find $\Delta FSR = FSR_s - FSR_i = 2\pi \times 3.5(1)$ MHz.

# 3

# TUNEABLE FP FILTERS FOR CE-SPDC OUTPUT

As described in the previous chapter, the output from the CE-SPDC source is in clusters of modes. To select a single (frequency) mode output from this, we employ a tuneable Fabry-Perot (FP) filter, one each in the signal and idler arm. The filter design aims for large transmission of a single SPDC cavity emission frequency, simultaneous with good rejection of other cavity emission frequencies, so that the filtered output has a bandwidth similar to the SPDC cavity linewidth. With careful attention to the cluster structure described in the preceding chapter, we identify parameters for the FP filter such that these two objectives can be achieved with a single filter. First, we theoretically discuss the modifications to the two-photon JSA from CE-SPDC due to the filters and analyse the filter parameters for which the output can be approximated to be in a single frequency mode. We then describe the design of the filters we employ, and also how the design enables the filter resonances to be tuned. We present measurements that characterise the filter performance and use the filter to perform an independent characterisation of the spectral structure of the CE-SPDC output. We show that through spectral analysis of the CE-SPDC output using the filter, the SPDC crystal temperature can be better optimised for phase matching as compared to performing SHG in the cavity (section 2.3). Parts of this chapter were adapted from [68].

## 3.1 THE FILTER MODIFIED TWO-PHOTON JSA

A spectral filter can be modelled as a frequency dependent beamsplitter that transmits a photon incident in spatial mode $a$ to mode $c$ with a frequency dependent amplitude transmission coefficient $\mathcal{T}(\omega)$, or reflects to mode $d$ with an amplitude reflection coef-

ficient $\mathcal{R}(\omega)$. This can be described with creation operators $\hat{a}^\dagger, \hat{c}^\dagger, \hat{d}^\dagger$ corresponding to modes $a, c, d$ according to [113],

$$\hat{a}^\dagger(\omega) = \mathcal{T}(\omega)\hat{c}^\dagger + \mathcal{R}(\omega)\hat{d}^\dagger. \tag{3.1}$$

For a FP filter with linewidth $\gamma_f$ and free spectral range $\mathrm{FSR}_f$, with its resonance centred at $\omega_f^0$, the transmission $\mathcal{T}(\omega) = \sqrt{T_0}\,\Gamma(\omega, \gamma_f, \omega_f^0, \mathrm{FSR}_f)$. Here $\sqrt{T_0}$ is the maximum on- resonance transmission amplitude and $\Gamma$ is an infinite sum of unit/amplitude complex Lorentzian functions, that describes cavity resonances (introduced in Equation 2.30),

$$\Gamma(\omega, \gamma, \omega^0, \mathrm{FSR}) \equiv \sum_{q=-\infty}^{\infty} \frac{\gamma/2}{\frac{\gamma}{2} + i\,(\omega^0 + q\,\mathrm{FSR} - \omega)}, \tag{3.2}$$

where $q \in \mathbb{Z}$. The transformation to the two-photon state from CE-SPDC (Equation 2.28) on being transmitted through a pair of filters with the same finesse and FSR, one each on the signal and idler arm, is,

$$|\psi_F\rangle \;=\; \alpha' \sqrt{T_0}\sqrt{T_0} \int_{-\infty}^{\infty} d\omega_s \int_{-\infty}^{\infty} d\omega_i\; f_F(\omega_s, \omega_i)\hat{c}_s^\dagger(\omega_s)\,\hat{c}_i^\dagger(\omega_i)\,|0,0\rangle\,, \tag{3.3}$$

where

$$\begin{aligned} f_F(\omega_s, \omega_i) \;&=\; f_{NB}(\omega_s, \omega_i) \prod_{\nu\in\{s,i\}} \Gamma(\omega_\nu, \gamma_\nu, \omega_\nu^0, \mathrm{FSR}_\nu) \\ &\quad\times \prod_{\nu\in\{s,i\}} \Gamma(\omega_\nu, \gamma_f, \omega_{f_\nu}^0, \mathrm{FSR}_f) \\ &=\; f_C(\omega_s, \omega_i) \prod_{\nu\in\{s,i\}} \Gamma(\omega_\nu, \gamma_f, \omega_{f_\nu}^0, \mathrm{FSR}_f). \end{aligned} \tag{3.4}$$

Here $f_{NB}(\omega_s, \omega_i)$ is the JSA from single-pass SPDC pumped by a monochromatic pump, given in Equation 2.29, $f_C(\omega_s, \omega_i)$ is the JSA from a CE-SPDC process, given in Equation 2.32. $\gamma_\nu$ and $\mathrm{FSR}_\nu$ for $\nu \in \{s, i\}$ are the CE-SPDC linewidth and FSR for the signal and idler respectively. $\gamma_f$ and $\mathrm{FSR}_f$ are the linewidth and FSR of the filters, respectively. The JSA after the filters is a product of the JSA from the CE-SPDC process and FP filter cavity resonances.

Similar to Equation 2.33, the rate of down-converted photon pairs available after filtering, is proportional to the square magnitude of the post-filter two-photon state

$$\langle\psi_F|\psi_F\rangle \;=\; |\alpha'|^2\, T_0^4 \int_{-\infty}^{\infty} d\omega_s \int_{-\infty}^{\infty} d\omega_i |f_F(\omega_s, \omega_i)|^2 \tag{3.5}$$

where $|f_F(\omega_s, \omega_i)|^2$ is the JSI from CE-SPDC after filtering.

$$|f_F(\omega_s, \omega_i)|^2 \propto l^2\pi^2 \operatorname{sinc}^2\left(\frac{\Delta k\, l}{2}\right) \prod_{\nu\in\{s,i\}} |\Gamma(\omega_\nu, \gamma_\nu, \omega_\nu^0, \mathrm{FSR}_\nu)|^2 \times \prod_{\nu\in\{s,i\}} |\Gamma(\omega_\nu, \gamma_f, \omega_{f_\nu}^0, \mathrm{FSR}_f)|^2 \tag{3.6}$$

### 3.1.1 Conditions for single mode output

The amplitude for the transmission of a signal-idler pair with frequencies $\omega_s^0$ and $\omega_i^0$ can be maximised by tuning the filters' index frequencies to coincide with those of the CE-SPDC cavity, i.e., $\omega_{f_\nu}^0 = \omega_\nu^0$ (where $\nu \in \{s, i\}$). Additionally, the transmission of unwanted frequency modes $\omega_s = \omega_s^0 + q_s \mathrm{FSR}_s$ and $\omega_i = \omega_s^0 + q_i \mathrm{FSR}_i$ can be reduced close to zero, by ensuring that the filter transmission function $\Gamma(\omega_\nu^0 + q_\nu \mathrm{FSR}_\nu, \gamma_f, \omega_\nu^0, \mathrm{FSR}_f) \approx 0$ (for $\nu \in \{s, i\}$) with the appropriate choice of filter parameters ($\mathrm{FSR}_f$ and $\gamma_f$). Mathematically, this means that for a given $\gamma_s, \gamma_i, \mathrm{FSR}_s$ and $\mathrm{FSR}_i$, appropriate $\gamma_f$ and $\mathrm{FSR}_f$ can be identified to minimize the integral of $|f_F|^2$ over frequencies not close to $\omega_s^0$ , $\omega_i^0$, given the constraint that $\omega_{f_\nu}^0 = \omega_\nu^0$ for $\nu \in \{s, i\}$. Here is a list of conditions that would ensure this, when the filters' index frequencies are made to coincide with those of the CE-SPDC cavity.

- $\gamma_f \gg \gamma_{s/i}$ : The linewidth of the filter cavity has to be larger than the linewidth of the CE-SPDC modes to ensure complete transmission of the full spectral width of the required CE-SPDC mode pair. The two-photon linewidth would be reduced if this is not satisfied.

- $\gamma_f \ll \mathrm{FSR}_{s/i}$: The FP linewidth has to be sufficiently smaller than the SPDC cavity's FSR to ensure adjacent CE-SPDC modes have a small transmission amplitude through the FP cavity. This will ensure $\Gamma(\omega_\nu^0 + q_\nu \mathrm{FSR}_\nu, \gamma_f, \omega_\nu^0, \mathrm{FSR}_f) \approx 0$ for $\nu \in \{s, i\}$.

- $\mathrm{FSR}_f \gg N_m\, \mathrm{FSR}_{mean}$: The filter FSR has to be significantly greater than the width of a cluster, to avoid adjacent filter resonances from transmitting CE-SPDC modes with frequencies $\omega_\nu^0 + q_\nu \mathrm{FSR}_\nu$. The cluster width in frequency is the product of the number of modes in a cluster ($N_m$, see Equation 2.52) and the mean FSR of the CE-SPDC cavity.

- Either $\mathrm{FSR}_f > \Delta\omega_{\mathrm{cluster}}$, or $\mathrm{FSR}_f \neq \frac{\Delta\omega_{\mathrm{cluster}}}{p}$ for $p \in \mathbb{Z}$: To avoid FP filter resonances from transmitting modes from other CE-SPDC clusters, the best solution would be to have a filter FSR that is greater than the cluster spacing $\Delta\omega_{\mathrm{cluster}}$ (refer Equation 2.51). However, if this is not possible, the cluster spacing should not be an integer multiple (nor approximately an integer multiple) of the filter FSR, since filter resonances repeat as integer multiples of the FSR.

If the FP filters employed are designed to satisfy these conditions, and if the filters' index frequencies are made to coincide with those of the CE-SPDC cavity, i.e., $\omega^0_{f_\nu} = \omega^0_\nu$, then the two-photon state after the filters, when pumped by a monochromatic pump, is well approximated by

$$|\psi_F\rangle \approx \int_{-\infty}^{\infty} d\omega_s \int_{-\infty}^{\infty} d\omega_i \; f'_F(\omega_s, \omega_i)\hat{c}^\dagger_s(\omega_s)\,\hat{c}^\dagger_i(\omega_i)\,|0,0\rangle\,, \tag{3.7}$$

where the JSA of two-photon state after the filters is,

$$f'_F(\omega_s, \omega_i) = \xi\,\delta(\omega_p - \omega_s - \omega_i) \prod_{\nu\in\{s,i\}} \frac{\gamma_\nu/2}{\frac{\gamma_\nu}{2} + i\,(\omega^0_\nu - \omega_\nu)}. \tag{3.8}$$

We call $f'_F$ the JSA for "perfect filtering" and consists of a single, i.e., nonrepeating, complex Lorentzian each for the signal and idler frequency, centred at $\omega^0_s$ and $\omega^0_i$ respectively, with a linewidth determined by the CE-SPDC linewidth, and the frequencies anti-correlated according to the energy conservation condition with the narrowband pump. The contribution from the crystal phase matching function has been reduced to a constant that is factored inside $\xi$, since the phase-matching bandwidth is much greater than the range of frequencies in the filtered two-photon state. When the central frequencies of the filtered signal and idler satisfy perfect momentum conservation with the pump, $\xi = \pi\alpha' l T_0$.

## 3.2 DESIGN OF TUNEABLE FABRY-PEROT FILTERS

Previous work on FP filters for CE-SPDC sources has taken a "monolithic" approach, in which a single piece lens is coated on either side to produce mirrors with desired reflectivity [114, 115]. Here, in contrast, we employ a three-element – rather than monolithic – design to more easily achieve the desired linewidth, FSR and tuning properties. Our design results in a FP cavity with a higher on resonance transmission

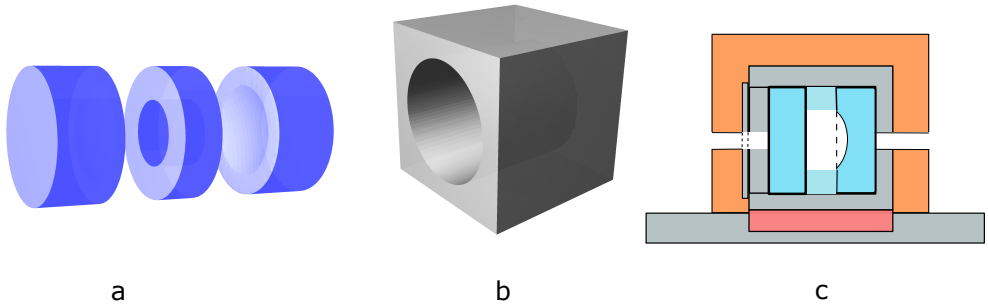


Figure 3.1: FP filter assembly. (a) The FP filter consisting of one concave mirror, an annular spacer, and a plano mirror in face-to-face contact cemented around the edges with epoxy and housed in an aluminium oven (image b). (c) Vertical cross section of the filter assembly: aluminium box and heat sink are shown in grey, the Peltier element in red, the mirrors and spacer in shades of blue and the insulator in orange.

than reported with the monolithic design. In comparison to the monolithic design, it is also less sensitive to mechanical stress from the mounting procedure, which can cause stress induced birefringence in the filter [115].

### 3.2.1 Components and assembly

The cavity is made by one plane mirror and one concave mirror (as shown in Figure 3.1) with a radius of curvature of $-1000\,\mathrm{mm}$ (LaserOptik mirror substrate part numbers S-00018 and S-00139). Both mirrors are of fused silica and have low loss ion-beam sputtered (IBS) multi-layer dielectric mirror coatings on the interior-facing surfaces, with nominal reflectivities ($R =$) $99.2(1)\%$ at $795\,\mathrm{nm}$. The mirrors are anti-reflection (AR) coated with IBS coatings and reflectivity $< 0.1\%$ on the exterior-facing surfaces. The absorption losses in the coatings are below 10 ppm and scattering losses from mirror surfaced below 20 ppm. A suitable separation of the two mirrors is achieved with a Borofloat annular spacer of $3.8(1)\,\mathrm{mm}$ thickness ($L_f$) with a $5.5\,\mathrm{mm}$ diameter hole, (custom made by LaserOptik).

To assemble the filter, the mirror-spacer-mirror stack is first held in face-to-face physical contact, and then a two-component epoxy (Varian Torr Seal) is applied around the edges to seal the trapped air space and provide structural rigidity. The resulting filter cavity resonance does not shift from sudden pressure changes in the laboratory from opening/closing the doors or movement of people. Neither does it shift due to

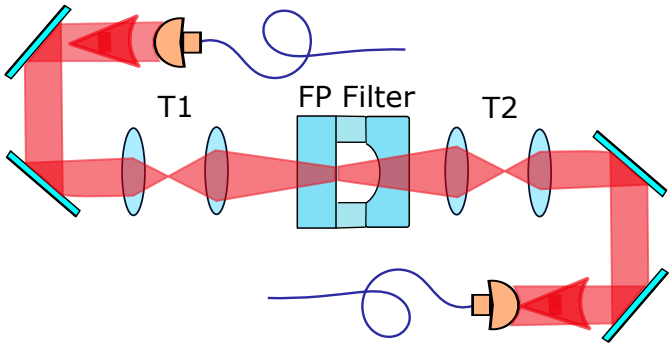


Figure 3.2: Schematic of optics for FP alignment. The beam waist is made to fall on the plain mirror of the FP assembly and beam curvature at the concave mirror matches that of the mirror using T1. T2 re-collimates the beam for fiber coupling. T1 and T2: Telescope 1 and 2.

any impact on the optical table. Thus the filter cavity is highly insensitive to vibration and pressure fluctuations and does not need to be stabilised by any active feedback mechanism.

### 3.2.2 Alignment

The TEM00 mode in the cavity has a beam waist at the plane mirror, with a spot size of 125 µm. To couple to the TEM00 mode, collimated light of diameter 1.8 mm is incident on a telescope which consists of an acromatic convex lens of focal length f=60 mm (AC254-060-B-ML Thorlabs) and a biconvex lens of focal length f= 25.4 mm (LB1761-B-ML Thorlabs). The telescope (T1) is used to focus the beam with a 125 µm waist, and the beam has a divergence such that its curvature matches the curvature of the concave mirror after the length fixed by the spacer (refer Figure 3.2). The filter is mounted on a translational stage along the beam direction, to ensure that the waist falls on the plane mirror. Another telescope (T2) with the same lenses is used to re-collimate the beam for coupling into fibre.

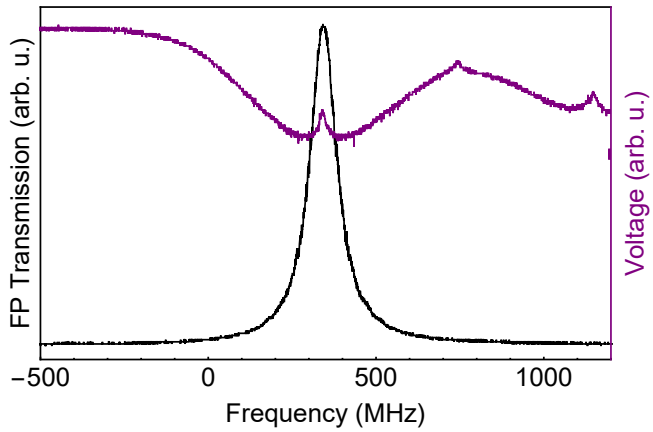


Figure 3.3: Transmission spectroscopy of FP filter. Black curve: Intensity transmission of frequency scanned laser through FP filter (left axis). Violet curve: Saturated absorption reference spectrum (right axis), obtained using light from the same laser, split off before the filter. Features in absorption used as a reference to calibrate linewidth and finesse of FP filter. Image shows filter tuned to be resonant to the $^5S_{1/2}\,F = 2 \rightarrow {}^5S_{1/2}\,F' = 1$ transition in $^{87}$Rb.

### 3.2.3 Attributes

The cavity FSR and linewidth were measured through transmission spectroscopy with an atomic reference (similar to the procedure in the previous chapter subsection 2.2.2). The 3.8 mm space between the FP mirrors gives the cavity an FSR of $FSR_f = 2\pi\times$ 39.4 GHz. The linewidth was measured to be $\gamma_f = 2\pi\times$ 96.6(9) MHz (see Figure 3.3). This gives a finesse of 410. We made two copies of the filter, one each for the signal and idler arms. Their maximum on resonance transmissions are 87% and 90%. Finesse and transmission measurements after two years of use show no signs of degradation.

### 3.2.4 Resonance tuneability

The FP filter resonance-frequency, or the signal-idler frequencies at which the maximum on resonance transmission through the filters is achieved, is altered by microscopic changes in the length of the FP cavity ($L_f$). This is controlled by changing the temperature of the FP filter. The change in length ($\Delta L$) of a material, initially with length

L, is related to its temperature change ($\Delta T$) through the coefficient of linear thermal expansion $\alpha_L$ according to,

$$\frac{\Delta L}{L} = \alpha_L \, \Delta T. \tag{3.9}$$

The filter cavity elements were chosen such that the mirrors have a low thermal expansion coefficient of $5.1 \times 10^{-7}\,K^{-1}$ (fused silica) and the spacer has a higher expansion coefficient of $3.2 \times 10^{-6}\,K^{-1}$ (Borofloat) so that the FP resonance is primarily influenced by the spacer's temperature. The resonance of the filter can be shifted by 1 $FSR_f/2\pi$ by changing its temperature by 31.7 K, while a 5 mK change corresponds to a shift in resonance of approximately 6 MHz, based on the values for the coefficients of thermal expansion.

The filter cavity is housed in a custom-built oven, constructed of an aluminium block with a circular bore to accept the glued mirror assembly, lined with a thermal interface pad (part number : EYG-S091210DP, from Panasonic electronic components), and with threaded aluminium end caps to hold the assembly in place. The aluminium block is insulated with a covering of 3 cm thick polystyrene foam and glued with thermally conducting epoxy to a Peltier element which in turn is glued to an aluminium heat dissipater (Figure 3.1 (c)). A 10 kΩ NTC thermistor embedded in the aluminium block and the Peltier element, are used to control the oven temperature, which is stabilised the same way as the crystals in the CE-SPDC . The temperature controller is again a HTC1500 controlled by an Arduino Uno + Analog Shield. The Arduino output voltage resolution of 150 μV corresponds to minimum resolvable steps of 5 mK change in temperature of the sensor at room temperature. The nonlinearity of the NTC response results in higher resolution at lower temperatures. The resolution is 2.5 mK at 15 °C, 5 mK at room temperature and 9 mK at 40 °C. Even in the worst case scenario of having a 10 mK temperature resolution, the filter's line-center can be tuned to within 6 MHz of a desired signal or idler frequency from the CE-SPDC. This worst-case mismatch implies $< 1\%$ loss of transmission relative to exact resonance.

## 3.3 CALCULATED OUTPUT AFTER FILTERS

We use expressions for the two-photon JSI from CE-SPDC Equation 2.33 and the FP intensity transmission function $|\Gamma(\omega_s, \gamma_{f_s}, \omega^0_{f_s}, FSR_f)|^2$ to model the overlap between the CE-SPDC spectrum for the signal and the resonances of a filter in the signal mode. As shown in Figure 3.4, our filter complies with the conditions stated in subsection 3.1.1,

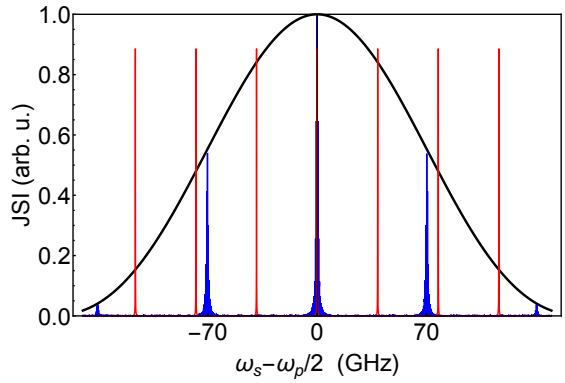


(a)

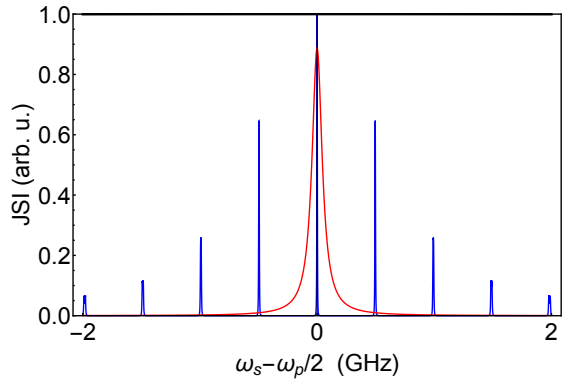


(b)

Figure 3.4: Calculated two-photon JSI from CE-SPDC with filter resonances. Black line shows $\text{sinc}^2$ crystal phase-matching function with the crystal tuned such that the degenerate modes, i.e., $\omega_i = \omega_s = \omega_p/2$, are brightest. Blue lines show CE-SPDC JSI $|f_C(\omega_s, \omega_p - \omega_s)|^2$ and red lines show FP cavity intensity transmission function $T_0\,|\Gamma(\omega_s, \gamma_{f_s}, \omega_s^0, \text{FSR}_f)|^2$. Graphs are plotted for the measured parameters of the bow-tie cavity, FP cavity and phase-matching bandwidth described in the text. The CE-SPDC resonances are organised into clusters spaced by 68 GHz, with the central cluster shown in (b). When the index frequency of the filter is matched with a mode from CE-SPDC (here the brightest-mode as shown in (b)), none of the other CE-SPDC modes fall within a filter resonance.

to obtain a single mode output. We use the two-photon JSI after the filters (Equation 3.6) when the filter's index frequencies coincide with those of the CE-SPDC ($\omega_{f_s}^0 = \omega_s^0$), to model the extinction of unwanted modes (Figure 3.5). From Figure 3.5, the discrimination

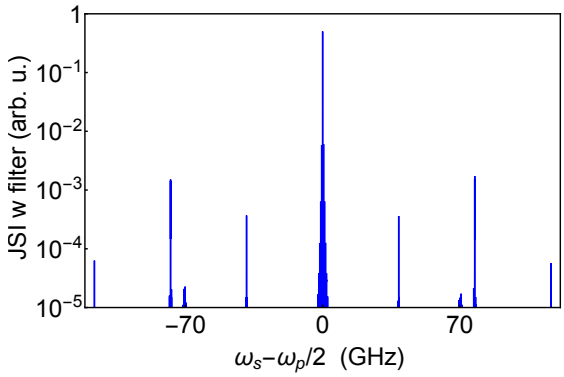


(a)

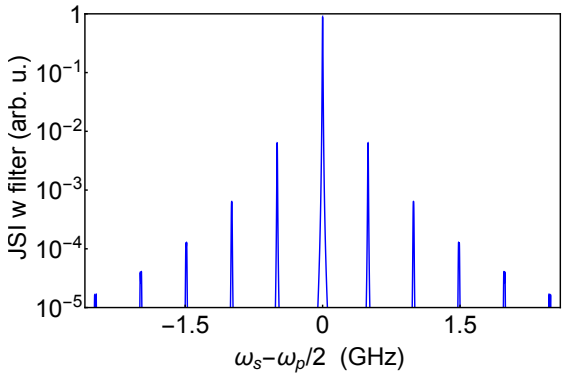


(b)

Figure 3.5: Calculated two-photon JSI from CE-SPDC after the FP filter. Graph shows $|f_F(\omega_s, \omega_p - \omega_s)|^2$ on the vertical axis and the detuning of the signal frequency from the degenerate mode ( centred at $\omega_s^0 = \omega_p/2$), on the horizontal axis. As in Figure 3.4, this shows the JSI for measured parameters of the CE-SPDC and filter cavities, when the crystal is tuned such that the degenerate signal-idler mode pair is brightest and when the signal-arm filter, described in section 3.2, is tuned such that $\omega_{f_s}^0 = \omega_s^0$. No filter is present in the idler arm, so that $T_0|\Gamma(\omega_i, \gamma_{f_i}, \omega_i^0, FSR_f)|^2 = 1$. If we define "unwanted" signal photons as those with frequencies $|\omega_s - \omega_s^0| > 2\gamma_s$, the contribution of unwanted photons is 2.3% within a window $2\pi c/\omega_s^0 \pm 1\,nm$ when the filter is set to transmit $\omega_s^0$. To calculate this, we take the ratio of $\int d\omega_s \ |f_F(\omega_s, \omega_p - \omega_s)|^2$ with limits $\omega_s^0 + 2\gamma_s$ to $\omega_s^0 + 2\pi\ 500\,GHz$, to the same integral performed with limits $\omega_s^0$ to $\omega_s^0 + 2\pi\ 500\,GHz$.

achieved by the filter would be greater than 20 dB for all nonselected modes. This is verified experimentally in chapter 4 and chapter 6.

## 3.4 CE-SPDC SPECTRUM ANALYSIS WITH FILTER

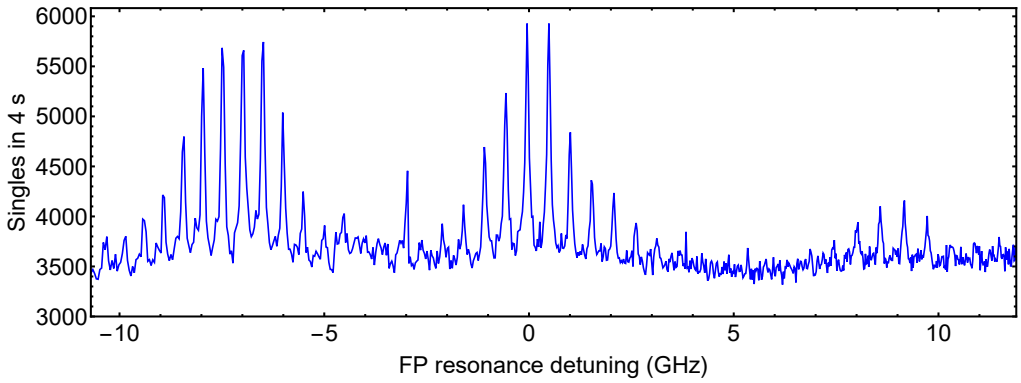


Figure 3.6: Analysis of signal photons' spectrum by scanning FP filter resonance. Plot shows signal singles detected after filtering when CE-SPDC was pumped with 4 $mW$. x-axis shows frequency detuning of modes from the $F = 2$ to $F' = 1$ transition in $^{87}$Rb. The filter resonance is scanned in steps and the singles measured for 4 s in each step. The output is in clusters of modes as seen from the DFG measurements. Additionally, due to the 39.4 GHz FSR of the filter cavity, the three clusters within the SPDC bandwidth are visible in this scan of width $\approx 20$ GHz (see text). The power asymmetry, between the cluster at $\sim -7$ GHz and that at $\sim 7$ GHz is due to the different phase-matching efficiency in the SPDC crystal. With temperature tuning of the SPDC crystal to maximize power in the central cluster (something we did not do), the powers of the clusters that are red and blue detuned would be more symmetric. Since the cluster centred on $\sim -7$ GHz, and that centred on $\sim 0$ GHz are of similar brightness, here perfect phase matching is achieved approximately midway between these two clusters. Thus the optimal phase matching, for data plotted here, is at a signal frequency about 35 GHz red-detuned from the frequency of the $F = 2$ to $F' = 1$ transition.

From Figure 3.4, and from Equation 3.6, it is evident that the brightest mode in the CE-SPDC emission spectrum corresponds to the signal-idler frequency pair for which perfect phase matching is achieved, since the sinc function gives the maximum amplitude at this combination of frequencies. Ensuring that the cavity is simultaneously

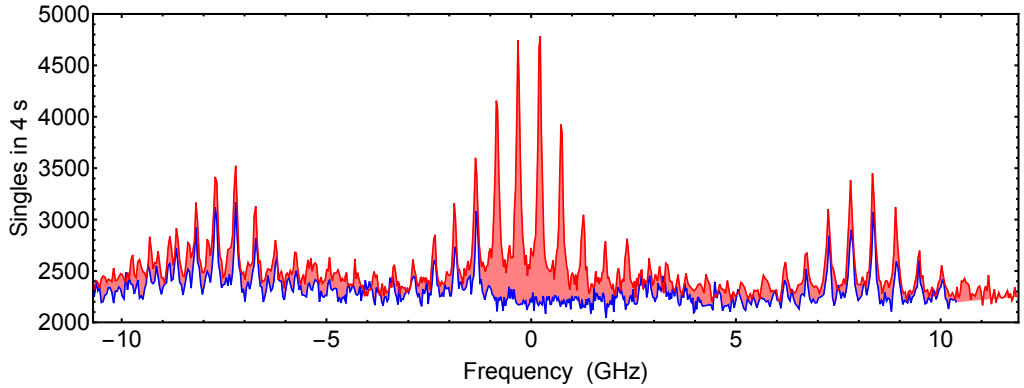


Figure 3.7: Analysis of CE-SPDC cluster frequencies using FP filter and vapour cell. The CE-SPDC is pumped with 4 $mW$ and tuned such that, in the brightest cluster, signal photons are resonant to the $F = 2$ to $F' = 1$ transition of $^{87}$Rb. The signal photons are passed through the FP filter and a Rb vapour cell and detected with an APD. Filter temperature is scanned in steps with 4 s acquisition at each temperature. Red filled region shows observed singles with the vapour cell at room temperature. Blue curve shows singles with the vapour cell at 90 °C. The modes from the brightest cluster are blocked by atomic absorption, with the singles count dropping to the background level. In contrast, the other two clusters are unaffected. The blue curve is uniformly weaker and has a lower background level due to a change in alignment.

resonant to the signal-idler modes at frequencies $\omega_s^0$ and $\omega_i^0$, automatically makes them the central and brightest modes of their respective clusters. However, in order for these frequencies to contain the maximum photon density, perfect phase matching has to be achieved at these frequencies. In section 2.3, we described how the phase-matching temperature is identified by SHG of cavity-resonant light. However, this method to identify the temperature works only when the required signal and idler are degenerate. To identify an optimal crystal temperature to produce nondegenerate photon-pairs where each mode in the pair is resonant to a different atomic transition, sum frequency generation of coherent light at these frequencies would have to be performed in the CE-SPDC cavity. We instead identified a simpler alternative to optimise the crystal temperature by analysing the output spectrum using the filter as a "spectrometer".

As described in section 3.2 the resonance of the FP filter can be adjusted by tuning its temperature. This feature can be exploited to analyse the signal/ idler spectrum from the CE-SPDC. For this, the CE-SPDC cavity is made resonant to the signal and idler

fields at the respective frequencies required using coherent light. The SPDC process is pumped with light at the sum of the signal and idler frequencies (described in the next chapter). The photon pairs produced are split and one of them detected in an APD after passing through the filter. As the filter temperature is scanned and its resonance shifts, the brightness of the singles detected in the APD varies, thereby revealing the frequencies and brightnesses of the modes produced by the CE-SPDC process. This is illustrated in Figure 3.6. The scan of the cavity, which covers about 11 GHz on either side of the $F = 2$ to $F' = 1$ transition, nonetheless shows the three clusters, predicted by theory to be found $-70$ GHz, 0 GHz and 70 GHz relative to this atomic line (see Figure 3.4a). The clusters are aliased into the range of the scan by multiples of the 39.4 GHz FP free spectral range. In this way, the cluster at 70 GHz, e.g., is expected to appear at $70 - 2 \times 39.4 = -8.8$ GHz, and indeed a cluster is seen at this detuning. By analysing the brightness of the modes, the discrepancy between the centre of the SPDC phase-matching envelope (or the frequency for which maximum phase matching is achieved) and the frequency of the required CE-SPDC cavity mode is determined. This is then corrected for by changing the temperature of the PPKTP crystal.

This "spectrometer" cannot estimate the absolute frequency of the photons. To verify that after correcting the SPDC crystal temperature, the brightest mode is indeed resonant to the atoms, we measure the attenuation of photons on transmission through a hot vapour cell. The filtered signal photons are passed through a natural abundance Rb vapour cell (internal length 10 cm) before they are detected in the APD. We heat the cell to 90 °C and thereby induce an atomic density sufficient to completely block light resonant to the $F = 2 \rightarrow F' = 1$ and 2 transitions in $^{87}$Rb, and $F = 3 \rightarrow F' = 2$ and 3 transitions in $^{85}$Rb. This was verified by measuring the transmission of coherent light of $\sim 1\,mW$. These transitions, spaced apart by 816, 702 and 361 MHz, with their individual Doppler broadened linewidths of $\approx 550$ MHz, effectively block light within a 3 GHz window. The filter frequency was scanned and the singles measurement repeated. Results are shown in Figure 3.7. The central cluster is strongly absorbed, as can be seen by comparison with data collected when the cell is at room temperature. This indicates that the modes are within the Doppler broadened transition lines. The transmission of the other clusters remains unaffected due to the large frequency spacing between clusters. It is also noteworthy that the attenuated portion of the spectrum drops to the background level. This shows that even if there are any "junk photons" i.e., those not

from the desired cavity mode, that pass the filter, they must be only within the spectral range blocked by the vapour.

# 4

# INDEPENDENT SIGNAL-IDLER TUNEABILITY

In addition to developing a narrowband photon-pair source where both photons are resonant to an atomic species, the introduction also presented a clear motivation for developing a photon-pair source that is versatile; where the frequency of each photon in the down-converted pair can be changed on demand based on the experiment planned and the atomic transitions involved. Having described in detail the heart of the system, the filtered CE-SPDC source for narrowband, single-mode photon pairs, we proceed to describe how frequency tuneability with $\sim$ MHz resolution is achieved. This chapter deals with the extended system of lasers and control systems surrounding the source with which we can independently tune the frequency of each photon in the down-converted pair. For this, we have implemented an interconnected frequency stabilisation scheme that fixes the frequencies of the pump, signal and idler photons in relation to one another. Furthermore, the system also enables independent control over each of the three abovementioned frequencies. Parts of this chapter were reported in [68].

## 4.1 INTERCONNECTED FREQUENCY STABILISATION

Figure 4.1 gives an overview of the interconnected frequency stabilisation scheme and the following subsections give the specific details. Figure 4.5 illustrates how the interconnected frequency stabilising scheme enables the production of signal and idler photons resonant to two different transitions in the $^{87}$Rb $D_1$ line separated by 816 MHz.

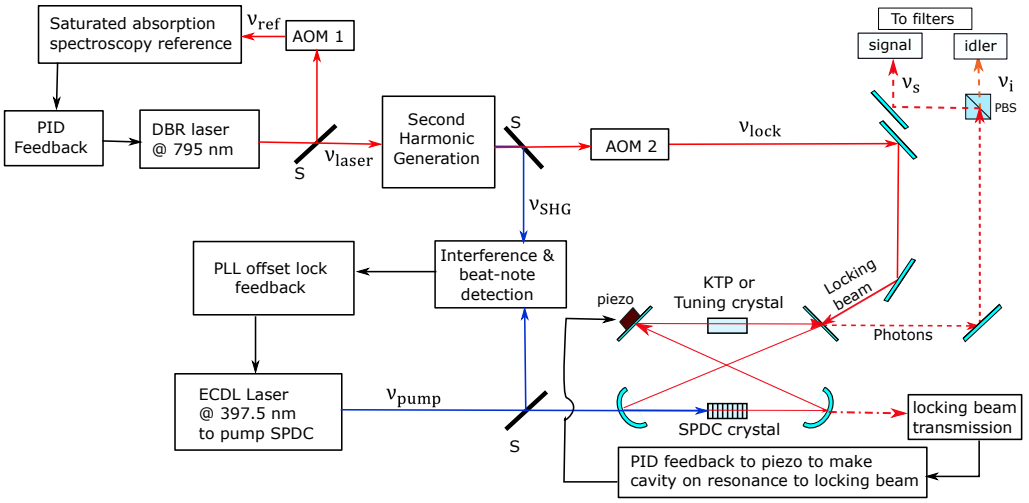


Figure 4.1: Overview of the interconnected frequency stabilising scheme to control pump, signal and idler frequencies. As described in the text, the cavity length and pump frequencies are stabilised with reference to light from a DBR laser which is stabilised to an atomic transition. Acousto-optic modulators AOM1 and AOM2 allow the cavity to be detuned from the transition, and the PLL offset lock allows the pump frequency to be independently controlled. The temperature of the tuning crystal controls the frequency difference between the signal and idler photons. Elements marked S indicate splitting of beams and do not represent any particular optical element. DBR: distributed Bragg reflector, PLL: phase-locked loop.

### 4.1.1 The reference laser at the $D_1$ line

To ensure that the down-converted photons are resonant to or detuned from a certain transition in Rb, their frequencies are set in relation to a reference laser stabilised to the same transition using spectroscopy techniques. Light from a 795 nm distributed Bragg reflector (DBR) laser, stabilised to the required transition frequency, serves as the reference. The laser diode is from Photodigm technologies (Photodigm Spectroscopy Series part number: PH795DBR080T8) and the laser housing is home-built. Thorlabs temperature and current controllers (TDC200C and LDC202C) are used to control the laser's temperature and current. A schematic of the optics and electronics to stabilise the laser is shown in Figure 4.2. Post beam-shaping, light from the laser is split into two arms, A and B. Beam A is coupled into fiber. Beam B is double passed through an acousto-optic modulator (AOM) driven by an amplified voltage-controlled oscillator

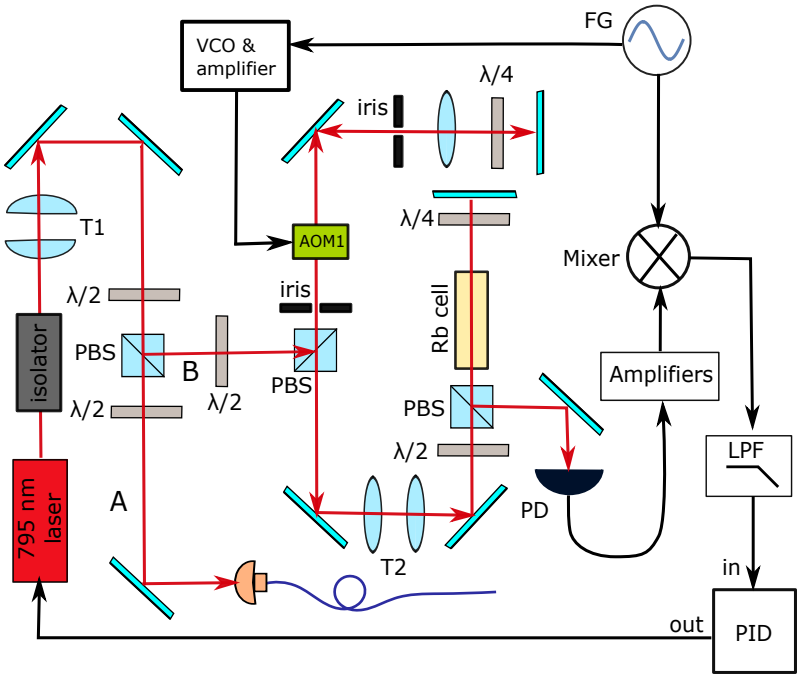


Figure 4.2: Frequency stabilisation scheme for reference laser. Light from a DBR laser at 795 nm is beam shaped at telescope T1 and split into paths A and B. Light in path B is double passed through an acousto-optic modulator (AOM1), where its frequency is shifted by $\nu_{\mathrm{AOM1}}$ and frequency side-bands are added from a function generator (FG), via a voltage-controlled oscillator (VCO) and RF amplifier. The beam diameter is increased at telescope T2 and it is double-passed through a hot Rb vapour cell. The signal, from a transition at $\nu_{\mathrm{ref}}$, is detected at photo-diode (PD). It is amplified and mixed with the modulation from the FG to generate the error signal. The error signal is passed through a low-pass filter (LPF) and is fed back to the laser current to stabilise the laser frequency though a PID controller. On being stabilised, the light in arm A has frequency $\nu_{\mathrm{ref}} - \nu_{\mathrm{AOM1}}$. PBS: Polarising beamsplitter, $\lambda/2$: half-wave plate, $\lambda/4$ quarter-wave plate.

(VCO) which shifts the frequency of the light by $\nu_{\mathrm{AOM1}} \in [150 - 170]$ MHz. The AOM also adds a modulation to the light at a depth of 6 MHz peak to peak (2 V peak to peak at control VCO's input) and a frequency of 2.89 MHz. The light is then used for saturated absorption spectroscopy [116]. The frequency of the laser is scanned by scanning its current. The saturated absorption spectroscopy signal, detected in a Thorlabs fixed-gain amplified detector (PDA10A-EC) is amplified, and mixed with a reference signal at

the 2.89 MHz modulation frequency to generate an error signal. This is then sent to a digital proportional integral derivative (PID) controller which is implemented in a FPGA-based data acquisition board (National Instruments PCIe-7842R). The feedback from the PID controller controls the laser current. Using this, the laser can be locked at the zero-crossing of the error signal corresponding to any transition in the rubidium $D_1$ line ($\nu_{ref}$). A diagrammatic representation of the electronic components for generating the error signal is also shown in Figure 4.2.

We use the error signal to also estimate the RMS linewidth of the laser on lock. The error signal generated for the PID lock is, in the regime used here, in which the modulation frequency is significantly less than the resonance linewidth, well approximated by the derivative of the signal from saturated-absorption spectroscopy. Since saturated-absorption spectroscopy is a Doppler-free spectroscopy technique, the line shape of the spectral features obtained from this technique is Lorentzian. So, the error signal is the derivative of a Lorentzian, and is,

$$\mathcal{X}(\Delta\mathcal{I}) = -V_0 \frac{\Delta\mathcal{I}\beta_e^2}{2\left(\Delta\mathcal{I}^2 + \frac{\beta_e^2}{4}\right)^2}, \tag{4.1}$$

where $\Delta\mathcal{I}$ is the change in laser current relative to the line centre, $\beta_e$ is the linewidth of the Lorentzian spectroscopy feature (which is broader than the natural linewidth due to other broadening mechanisms [116]) and $V_0$ is a constant with units of voltage. The error signal has an inflection point at $\Delta\mathcal{I} = 0$, a maximum at $\Delta\mathcal{I} = \frac{-\beta_e}{2\sqrt{3}} \equiv \Delta\mathcal{I}_{max}$ and a minimum at $\Delta\mathcal{I} = \frac{\beta_e}{2\sqrt{3}} \equiv \Delta\mathcal{I}_{min}$. Since we can measure $\Delta\mathcal{I}$ at the maxima or minima of the error signal, we can infer $\beta_e$ from this. Using an oscilloscope, we can measure the peak to peak voltage of the error signal, which is $\mathcal{X}(\Delta\mathcal{I}_{max}) - \mathcal{X}(\Delta\mathcal{I}_{min})$ and use Equation 4.1 to get the value of the contant $V_0$.

The error signal is approximately linear close to the inflection point, and the laser frequency fluctuations on lock are expected to be within this regime. The error signal close to the inflection point is ,

$$\mathcal{X}_{lin}(\Delta\mathcal{I}) \approx -7.8\,\frac{V_0}{\beta_e^2}\,\Delta\mathcal{I}. \tag{4.2}$$

We calculate the RMS laser current fluctuations $\Delta\mathcal{I}_{rms}$ using Equation 4.2 and the measured RMS fluctuations $\mathcal{X}_{rms}$. Due to the linearity of Equation 4.2, this is simply $\Delta\mathcal{I}_{rms} \approx \frac{\beta_e^2}{7.8V_0}\mathcal{X}_{rms}$.

The RMS current fluctuations on lock can then be translated to laser frequency fluctuations by calibrating the change in laser frequency to the change in laser current. This calibration factor $\rho$ is the ratio of the frequency spacing between any two transitions found in literature [117] to the change in laser current needed to observe these transitions in the saturated absorption spectroscopy signal. The RMS linewidth of the laser on lock is $\nu_{rms} = \rho\ \Delta J_{rms}$ and is $0.9\,\mathrm{MHz}$ for our laser on lock.

### 4.1.2 Pump stabilisation

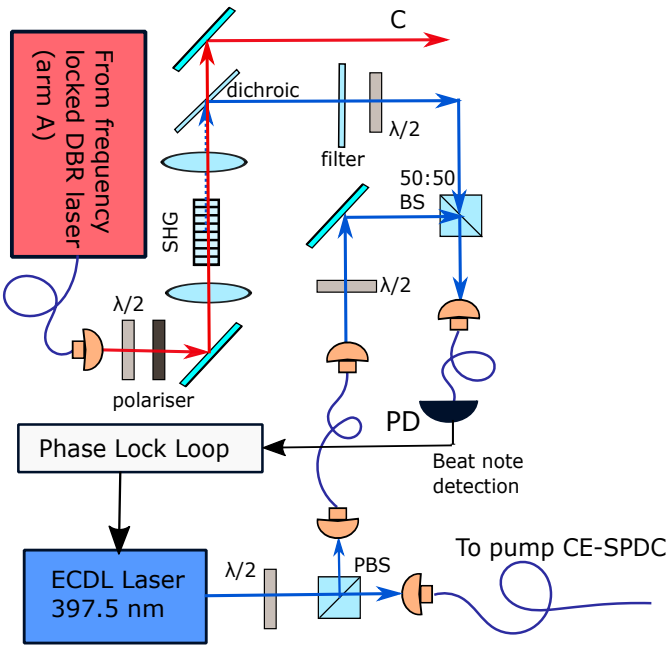


Figure 4.3: Frequency stabilisation scheme for pump laser. SHG of the 795 nm reference laser is used to stabilise pump using a beat-note lock as described in text. The undepleted red light in arm C is used to stabilise the cavity as illustrated in Figure 4.4.

A grating stabilised external-cavity diode laser (ECDL) with a central wavelength at 397.5 nm (DLC DL PRO HP from TOPTICA Photonics) is used as the SPDC pump with frequency $\nu_p$. The down-conversion process to signal-idler pairs at specific frequencies ($\nu_s$ and $\nu_i$ respectively), requires the the pump to be stabilised to $\nu_p = \nu_s + \nu_i$. For

this, the pump is stabilised in relation with the light from the reference laser at 795 nm, which was described previously and which also determines $\nu_s$ and $\nu_i$.

The frequency locked 795 nm laser beam from arm A (at $\nu_{laser} = \nu_{ref} - \nu_{AOM1}$) in Figure 4.2, is upconverted to $\nu_{SHG} = 2\nu_{laser}$, through second harmonic generation (SHG) as shown in Figure 4.3. The SHG occurs in a collinear type-I phase matched PPKTP crystal of length 20 mm in a single-pass configuration. The crystal is enclosed in a Teflon oven and its temperature stabilised using a temperature stabiliser from Wavelength Electronics (HTC3000) and NTC sensors. Teflon was chosen as an insulator since it is easily machinable into a required form. The conversion efficiency to blue is $\approx 4\,\%W^{-1}$. The upconverted light is separated using a dichroic mirror and mode matched to light from the pump laser, by mixing on a 50:50 beamsplitter and coupling into a single mode fiber. The beat note produced at $\nu_{beat} = |\nu_p - \nu_{SHG}|$ is detected using an amplified silicon detector with a bandwidth of 1.5 GHz (FPD310-V from Menlo Systems). A beat-note signal with sufficient signal-to-noise ratio is obtained when $7\,\mu W$ of light at $\nu_{SHG}$ and $200\,\mu W$ of light at $\nu_p$ are coupled in fiber. The beat-note (and consequently $\nu_p$) is stabilised using a software controlled digital phase-locked loop (PLL) (frequency synthesizer ADF4111 from Analog Devices, in an evaluation board EV-ADF411XSD1Z). The evaluation board, manufactured to stabilise the RF frequency from a VCO, is slightly altered to suit our purposes. The PLL generates a train of charged pulses that vary in voltage and polarity depending on the difference between the detected beat frequency $\nu_{beat}$ and the required beat frequency $\nu^0_{beat}$ (set via the software). This is extracted from the evaluation board and sent to an integrator which converts the charge pulse train to a voltage $V_{beat} \propto \nu^0_{beat} - \nu_{beat} \equiv \nu^0_{beat} - |\nu_p - \nu_{SHG}|$. $|V_{beat}|$ increases as the difference between the desired and actual beat signals increases on either side of the zero-crossing at $\nu^0_{beat} = |\nu_p - \nu_{SHG}|$. The DLC-pro digital controller for the pump laser uses this signal in an inbuilt side-of-fringe lock to stabilise the laser frequency at the zero-crossing. The resulting frequency lock allows us to lock the pump laser frequency within the range $80\,\text{MHz} \leqslant |\,\nu_p - 2\nu_{laser}\,| \leqslant 1.5\,\text{GHz}$. The pump frequency is chosen to achieve the energy conservation condition $\nu_s + \nu_i = \nu_p$. With this scheme, we can generate degenerate or nondegenerate photons at 795 nm up to a maximum frequency difference between signal and idler photons that is limited by the speed of the beat-note detector for the blue light.

The short-term linewidth of the pump laser is ~ 100 kHz, which is small relative to other linewidths in the system. The (frequency-doubled) light it is referenced to has

a linewidth of twice 0.9 MHz, including both fast and slow fluctuations. We expect the bandwidth of the PLL loop to be at most ~ 10 kHz, and thus only a fraction of the reference laser's fluctuations will be copied onto the pump laser through the beat-note lock. As a result, we can say that the pump laser linewidth is between 0.1 MHz and 2 MHz.

### 4.1.3 Control of signal and idler frequencies

For signal and idler photons at frequencies $\nu_s$ and $\nu_i$ respectively, the down-conversion cavity must be simultaneously resonant to light at each of these frequencies at the corresponding polarisation. This section describes how this is achieved.

The 795 nm reference light at $\nu_{laser} = \nu_{ref} - \nu_{AOM1}$, that remains unconverted after SHG (arm C in Figure 4.3), is double-passed through a second AOM as shown in Figure 4.4. The AOM shifts the frequency to $\nu_{lock} = \nu_{laser} + \nu_{AOM2}$ and adds a modulation at a depth of 6.5 MHz peak to peak and a frequency of 2.7 MHz to enable a dither lock of the SPDC cavity. The tuning range of the AOMs allows $\nu_{AOM1}$ and $\nu_{AOM2}$ to be independently set in the range from 150 MHz to 170 MHz. Thus $\nu_{lock}$ can be detuned from the atomic transition frequency at $\nu_{ref}$ by $\nu_{AOM2} - \nu_{AOM1}$, to account for ac Stark shifts, a.k.a. "light shifts" in the trapped cold atom(s). This "locking light" passes through a spinning-blade mechanical chopper, as shown in Figure 4.4, enters the CE-SPDC cavity via M4 and is matched in spatial mode and polarisation to the $V$ polarised signal mode of the cavity. A small fraction of this light exits the cavity by transmission through M2 and is collected on PD2. This signal is demodulated to obtain an error signal which is fed to a PID mechanism controlling the piezo on M3. By controlling the piezo, the cavity length is actively adjusted to ensure that the signal mode of the SPDC cavity is always resonant to $\nu_{lock}$. The electronics and PID controller for stabilising the piezo length are similar to the system used to stabilise the DBR laser.

With the cavity length actively stabilised such that the signal mode at $\nu_s = \nu_{lock} \equiv l\,FSR_s/2\pi$ is resonant in the cavity, the idler mode can be stabilised at a frequency $\nu_i = \nu_s + \Delta\nu \equiv m\,FSR_i/2\pi$ for some integers $l$ and $m$. The frequency offset $\Delta\nu = (m\,FSR_i - l\,FSR_s)/2\pi$, is fixed by controlling the net birefringence in the cavity. While the SPDC crystal's temperature is maintained at a value that gives efficient phase-matching, the net birefringence is altered by changing the temperature of the tuning

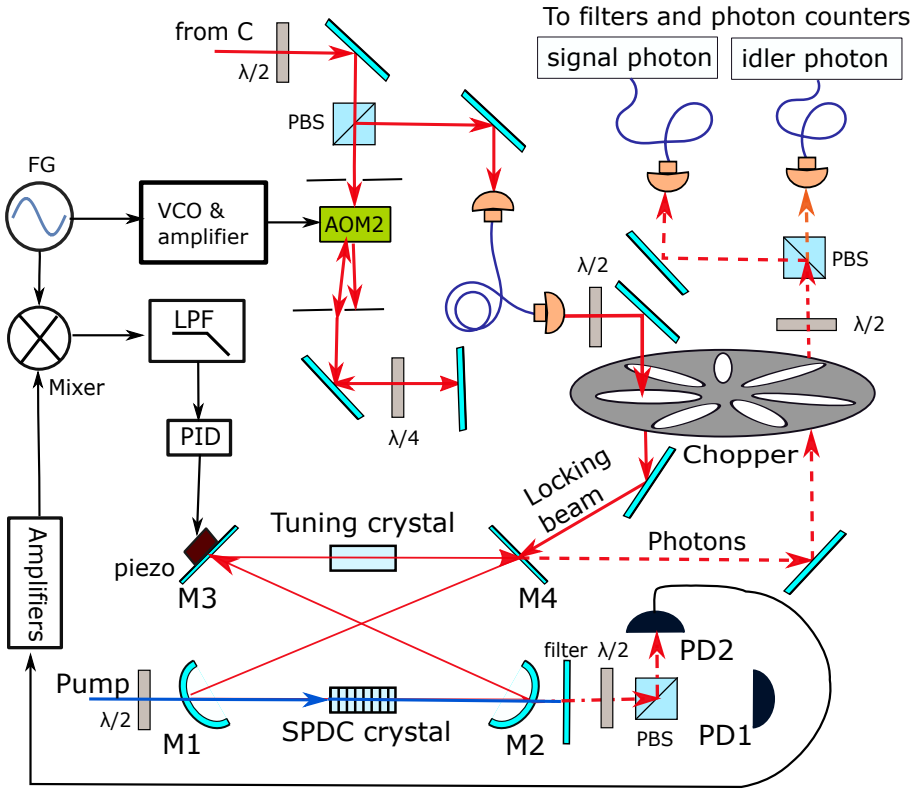


Figure 4.4: Schematic of stabilised CE-SPDC cavity. Light in arm C is frequency shifted at AOM2 to $\nu_{lock} = \nu_{ref} - \nu_{AOM1} + \nu_{AOM2}$ with frequency side-bands introduced from a FG via a VCO. Its polarisation is matched to the signal mode in CE-SPDC cavity, and its transmission through the cavity, detected on PD2, is used to generate an error signal for the PID controller. The electronic components function similar to the description in Figure 4.2. The chopper blocks the cavity-detector path taken by the down-converted photons (dashed line) whenever the laser-cavity path is open, preventing locking light from reaching the detectors.

(KTP) crystal. Transmission of coherent H polarised light at $\nu_i$ injected via M4 and measured through any of the HR mirrors, verifies the resonance of the idler mode.

Since $| \nu_p - 2\nu_{laser} | \leqslant 1.5\,\text{GHz}$, $\nu_p = \nu_s + \nu_i$ and $\nu_s = \nu_{lock} = \nu_{laser} + \nu_{AOM2}$, the maximum possible value by which the signal can be blue detuned from the idler is $\nu_s - \nu_i = 1.82\,\text{GHz}$ and the maximum possible value by which the signal can be red detuned from the idler photon is $\nu_i - \nu_s = 1.18\,\text{GHz}$, when $\nu_{AOM2} = 160\,\text{MHz}$.

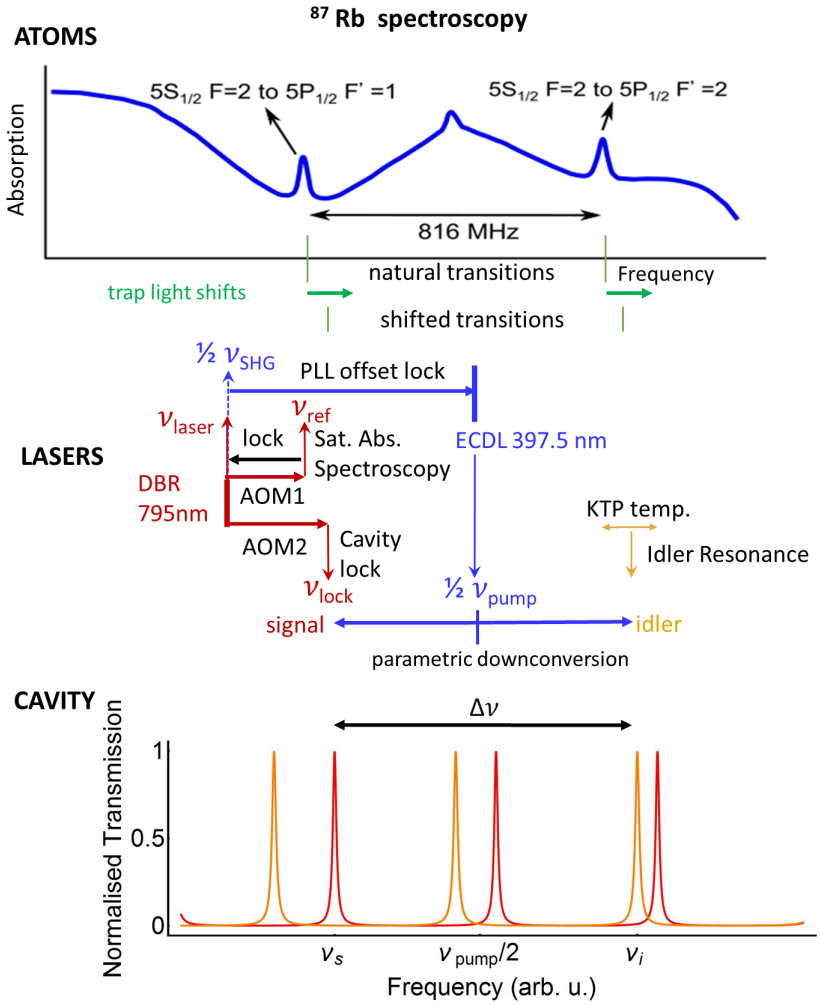


Figure 4.5: Illustration of frequencies employed in the CE-SPDC source. Scenario shown achieves the configuration: $\nu_s$ tuned to the (light-shifted) $F = 2 \rightarrow F' = 1$ transition and $\nu_i$ tuned to the (light-shifted) $F = 2 \rightarrow F' = 2$ transition of the $^{87}$Rb $D_1$ line. Top graph ("atoms") shows the saturated absorption spectrum (in blue) with light-shifted transitions shown below the horizontal axis in green. Middle section ("lasers") shows frequency relationships among frequencies described in the text. Frequency separations are not to scale. Lower section ("cavity") shows cavity spectrum including signal (red) and idler (orange) modes. The $\Delta$FSR and $\gamma$ are exaggerated for clarity.

## 4.2 RESULTS: VERIFICATION OF INDEPENDENT TUNEABILITY

### 4.2.1 Atomic spectroscopy with CE-SPDC photons

To test the independent tuneability of the CE-SPDC signal and idler, we performed single-photon spectroscopy on a Rb vapour cell of 10 cm length. The cell was heated to 40 °C, a temperature at which the absorption at different transitions can be clearly distinguished. For reference, a spectrum under the same conditions was taken with 6 μW of laser light. This low power was chosen to avoid saturation of the spectrum by optical pumping.

For each measurement, we tuned the signal, idler and pump frequencies using the techniques described in section 4.1: $\nu_{lock}$, and thus $\nu_s$, was set to a feature of the $D_1$ saturated absorption spectrum of either one of the rubidium isotopes. $\nu_i$ was set to $\nu_s + \Delta\nu$ with $\Delta\nu = 250\,\text{MHz}$ or $-170\,\text{MHz}$ by temperature tuning of the tuning crystal. The pump was locked to $2\nu_s + \Delta\nu$ to satisfy energy conservation. Either signal or idler, filtered with a tuneable filter tuned to pass the corresponding frequency, was passed through the vapour cell and detected with an APD. A beamsplitter before the cell split a portion of the intensity to an auxiliary APD for a simultaneous measurement of fluctuations in the source brightness. The measured background, i.e. APD counts with the SPDC turned off by blocking the pump, was subtracted. The singles rate was normalised by the measured brightness in the auxiliary APD to obtain the cell transmission. The cell transmission, thus defined, was calibrated by tuning the CE-SPDC source far from resonance, where the absorption is negligible. As shown in Figure 4.6, we measured the transmission for signal photons, and for their corresponding idlers, at seven different frequencies for each of the two different values of $\Delta\nu$. Each data point corresponds to an acquisition time of 12 s at 4 mW pump power, which yielded roughly 20,000 detections in transparent regions of the spectrum. The results show good quantitative agreement with the absorption spectrum as measured by a laser. The signal-idler frequency separations were chosen to provide good coverage of the atomic absorption spectrum. This demonstrates both the ability to generate correlated, independently-tuneable photon pairs with MHz precision, and single-mode operation even as these photons are tuned over a wide range.

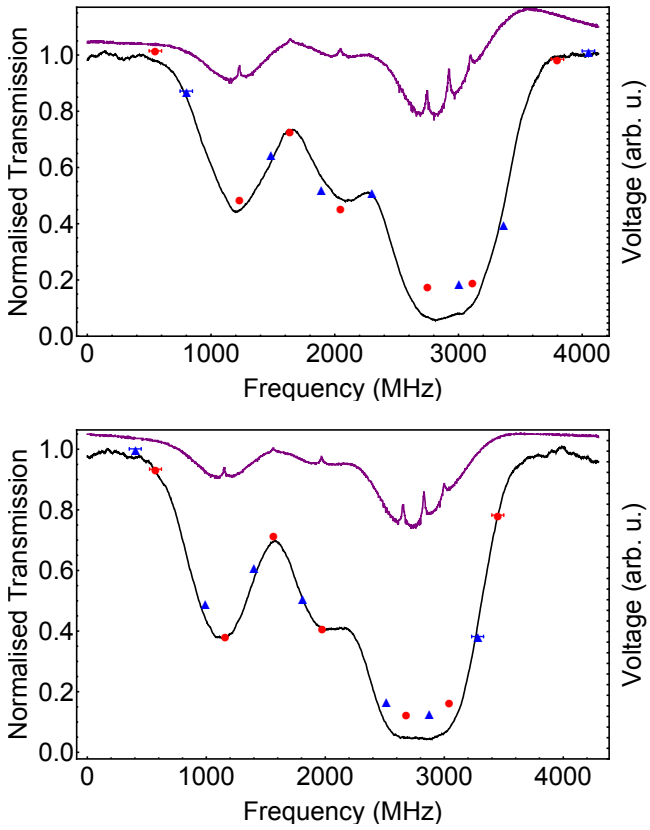


Figure 4.6: Atomic vapour spectra acquired with CE-SPDC photons. Black curves: measured transmission of a frequency-scanned weak-laser through a heated, natural-abundance Rb vapour cell. Violet curves: saturated absorption spectrum (right axes) with another cell and copy of frequency-scanned light, for reference. Red disks and blue triangles: signal and idler transmission, respectively, through the heated cell. The CE-SPDC photons were tuned as described in section 4.1 and filtered to a single-mode as described in section 3.2. When possible, $\nu_s$ was stabilised to a feature of the saturated absorption spectrum, while $\nu_i$ was stabilised to (top) $\nu_s + 250\,\mathrm{MHz}$ or (bottom) $\nu_s - 170\,\mathrm{MHz}$. At the edges of the spectrum $\nu_s$ was not actively stabilised, and horizontal error bars indicate the uncertainty in the estimated frequency of the lock light and consequently the signal/idler photons. Poisson distributed noise in the detected photons would contribute vertical error bars smaller than the symbols and are not shown.

### 4.2.2 Experimental quantification of single mode output

As seen in Figure 4.6, the minimum transmission of the laser is $\approx$ 10%, whereas the minimum transmission of filtered CE-SPDC light is $\approx$ 20%, due to contamination by photons outside the desired spectral mode. To precisely quantify this content, we repeated the measurement in subsection 4.2.1 with a higher cell temperature of 75 °C and with the laser and CE-SPDC source (including the FP filter) tuned to generate photons at $^{87}$Rb $F = 2 \rightarrow F' = 2$ transition. We observed a transmission of 7.7% for the CE-SPDC photons versus 0.04% for the laser, whereas the prediction from Equation 3.6 for the CE-SPDC photons would be 2.3% (see caption of Figure 3.5). Thus 92.3% of photons at the output of the CE-SPDC and FP filter system are in a single mode. Possible explanations for the mismatch with the theoretical estimate include coupling of down-converted photons to higher order transverse modes in the CE-SPDC or FP cavities and distortion of the phase-matching profile due to imperfect poling of the nonlinear crystal. We note that the percentage of contamination seen using atoms as a frequency filter is much higher than the contamination seen from correlation measurements reported in chapter 6. Since they appear only in singles measurements but disappear in coincidence measurements, these "junk" photons may possibly not be a result of the SPDC process, but rather an outcome of some other process like ordinary fluorescence.

Part II

# SPECTRAL CHARACTERISATION THROUGH INTENSITY CORRELATION MEASUREMENTS & TIME-RESOLVED QUANTUM INTERFERENCE

# 5

# PHOTON CORRELATION MEASUREMENTS

Temporal correlation functions have always been an important tool to characterise the statistics of a light source. Since Glauber's pioneering work on introducing a quantum mechanical formalism to quantify the degree of coherence in sources [118], temporal correlation functions have become indispensable for investigating nonclassical sources of light. Today, correlation functions are used for applications ranging from spectral measurements to quantifying the indistinguishability and spectral purity of photon states.

In this chapter, we apply measurements of correlation functions, specifically second-order correlation functions, to characterise the photons from our source. While photons from SPDC are bunched in time since they are produced simultaneously, measuring their temporal correlations also reveals information about the spectral correlations between the photon pairs. We discuss and demonstrate how changing the two-photon spectrum through cavity enhancement and filtering affects the correlation measurements. We also apply correlation functions to verify that at any given instant, we have a negligible presence of multiple down-converted pairs in the output from our source. Many of the results reported in this chapter were also published in [68].

This chapter is structured such that each section is dedicated to a measurement and is complete with the relevant theory and experimental results. We first introduce the mathematical formalism for a correlation function and then translate it to experimental measures. We analyse the relation between the second-order temporal statistics of the photon pairs and their joint-spectrum. We then present and discuss the results from applying various correlation measurements to our source.

For completeness we begin by recalling some fundamental concepts from [118] on correlation functions. From the Glauber theory of photodetection, the detection rate

for joint detection of $n$ photons at times $t_1, t_2, \ldots, t_n$, for a given input state $|\psi_i\rangle$, is proportional to the $n^{th}$ order correlation function $G^{(n)}$,

$$\begin{aligned} G^{(n)}(t_1, t_2, \ldots, t_n) &= \sum_f |\langle \psi_f | \hat{E}^{(+)}(t_n), \ldots, \hat{E}^{(+)}(t_2)\hat{E}^{(+)}(t_1) | \psi_i \rangle|^2 \\ &= \langle \psi_i | \hat{E}^{(-)}(t_1), \hat{E}^{(-)}(t_2), \ldots, \hat{E}^{(-)}(t_n) \\ &\quad \times \hat{E}^{(+)}(t_n), \ldots, \hat{E}^{(+)}(t_1) | \psi_i \rangle , \end{aligned} \tag{5.1}$$

which is proportional to the probability density for such an event. Here $\hat{E}^{(-)}$ and $\hat{E}^{(+)}$ are the negative and positive parts of the quantised electro-magnetic field and $\sum_f$ is the sum over all possible final states $|\psi_f\rangle$ the field may be in after the detection process and we use the completeness relation, $\sum_f |\psi_f\rangle \langle \psi_f| = 1$, in the last line. The normalised $n^{th}$ order correlation function is,

$$g^{(n)}(t_1, t_2, \ldots, t_n) = \frac{G^{(n)}(t_1, t_2, \ldots, t_n)}{\prod_{j=1}^{n} G^{(1)}(t_j)}. \tag{5.2}$$

## 5.1 SECOND-ORDER INTENSITY CROSS-CORRELATION FUNCTION

The temporal correlations between the signal (s) and idler (i) in a down-converted pair are analysed through the second-order cross-correlation function $G^{(2)}_{s,i}$, which gives the correlation between intensities of the signal and idler fields [119]. For the signal detected at $t_s$ and the idler at $t_i$,

$$G^{(2)}_{s,i}(t_s, t_i) = \langle \psi | \hat{E}^{(-)}_s(t_s)\hat{E}^{(-)}_i(t_i)\hat{E}^{(+)}_i(t_i)\hat{E}^{(+)}_s(t_s) | \psi \rangle . \tag{5.3}$$

Often we deal with statistically stationary fields i.e., where the correlation functions of the fields are invariant under displacements of the time variable [119]. The correlation function $G^{(2)}$, then depends only on the delay between the detections $\tau = t_i - t_s$. For $t_s = t$ and $t_i = t + \tau$, $G^{(2)}_{s,i}(t_s, t_i) = G^{(2)}_{s,i}(t, t + \tau) \equiv G^{(2)}_{s,i}(\tau)$, gives the distribution of detecting an idler photon with a delay $\tau$ relative to the detection of a signal photon. The

normalised second order intensity cross-correlation function as a function of the delay is,

$$\begin{aligned} g^{(2)}_{s,i}(\tau) &= \frac{\left\langle \hat{E}^{(-)}_s(t)\hat{E}^{(-)}_i(t+\tau)\hat{E}^{(+)}_i(t+\tau)\hat{E}^{(+)}_s(t)\right\rangle}{\left\langle \hat{E}^{(-)}_i(t+\tau)\hat{E}^{(+)}_i(t+\tau)\right\rangle \left\langle \hat{E}^{(-)}_s(t)\hat{E}^{(+)}_s(t)\right\rangle}, \\ &= \frac{G^{(2)}_{s,i}(\tau)}{G^{(1)}_i(t+\tau)G^{(1)}_s(t)}, \end{aligned} \tag{5.4}$$

where $\langle . \rangle$ is the expectation value over the input state. This can be further simplified when the fields are stationary, because $G^{(1)}(t+\tau) = G^{(1)}(t)$, to

$$g^{(2)}_{s,i}(\tau) = \frac{G^{(2)}_{s,i}(\tau)}{G^{(1)}_i(t)G^{(1)}_s(t)}. \tag{5.5}$$

## 5.2 MEASURING FIELD CORRELATION FUNCTIONS

From Glauber's theory of photo-detection, the expected rate of detecting photons $R^{(1)}(t)$ from a field $\hat{E}$ for the state $|\psi\rangle$ is proportional to $\left\langle \hat{E}^{(-)}(t)\hat{E}^{(+)}(t)\right\rangle = G^{(1)}(t)$, where $\langle . \rangle$ is the expectation value over the state $|\psi\rangle$. Similarly, the expected "joint counting rate" [1] $R^{(2)}_{1,2}(t_1, t_2)$ of detecting two photons, one from a field $\hat{E}_1$ at time $t_1$ and another from $\hat{E}_2$ at time $t_2$ is proportional to $G^{(2)}_{1,2}(t_1, t_2)$ [119]. In the experiment, photons are detected and marked in time with a finite resolution. The measurement of the field correlations and detection rates do not have an infinite resolution but are rather "coarse grained" in time. The precision in the time assigned to a detection, which is also the smallest resolvable time difference between two detections, is called a "bin" and is indicated with the symbol $t_b$. For an integer $k$, the statistical average of the number of photons from field $\hat{E}_1$, detected in the $k^{\text{th}}$ bin, i.e., the average number of photons in the interval $[kt_b, (k+1)t_b)$, is

$$\bar{n}^{(k)}_1 = \int_{k\,t_b}^{(k+1)t_b} R^{(1)}_1(t_1)\,dt_1 \propto \int_{k\,t_b}^{(k+1)t_b} G^{(1)}_1(t_1)\,dt_1. \tag{5.6}$$

1 Note that the joint counting rate has units of $s^{-2}$.

In a measurement run, $n_1^{(k)}$ is the measured number of photon detection events from field $\hat{E}_1$ in the $k^{th}$ bin [2]. For stationary fields, $G^{(1)}(t)$ is the same at all times, and so the photon counting rate is also the same at all times. Thus the sample mean, which is an unbiased estimator for the average number of photons detected from a field $\hat{E}_1$, is

$$\tilde{n}_1 = \sum_k^N \frac{n_1^{(k)}}{N}, \tag{5.7}$$

where $N$ is the largest bin number in the measurement. Similarly, the average number of simultaneous detections of two photons, one from $\hat{E}_1$ in the $k^{th}$ bin and another from $\hat{E}_2$ in the $l^{th}$ bin, is

$$\bar{n}_{coin}(t^{(k)}, t^{(l)}) \propto \int_{k\,t_b}^{(k+1)t_b} dt_2 \int_{l\,t_b}^{(l+1)t_b} dt_1\, G_{1,2}^{(2)}(t_1, t_2), \tag{5.8}$$

and can be called the expected number of coincidences detected between fields 1 and 2 at bins $k$ and $l$, respectively. Experimentally, the number of coincidence detection events of this kind in a measurement run is $n_1^{(k)} n_2^{(l)}$. For stationary fields, we are interested in the total number of coincidences $n_{coin}$ at a certain delay $\tau = t_b\,\Delta$ where $\Delta = l - k$, because only the delay between the detections matters for the $G^{(2)}$ and not the absolute values of $k\,t_b$ and $l\,t_b$ as explained previously. Thus the experimental sample mean, an estimator of the average coincidences at a delay $\tau = t_b\,\Delta$, at positive delays ($0 \leqslant \Delta < N$) is

$$\tilde{n}_{coin}(t_b\,\Delta) = \frac{1}{N-\Delta} \sum_{k=1}^{N-\Delta} n_1^{(k)} n_2^{(k+\Delta)}. \tag{5.9}$$

Usually the total coincidences, $n_{coin}(\Delta t_b) = \sum_{k=1}^{N} n_1^{(k)} n_2^{(k+\Delta)}$, are reported for measurements of the un-normalised second-order correlation function. To compute the normalised second-order correlation function, we use Equation 5.8 and Equation 5.6 in Equation 5.5 to get,

$$g_{1,2}^{(2)}(t_b\,\Delta) \quad \propto \quad \frac{\bar{n}_{coin}(t^{(k)}, t^{(k+\Delta)})}{\bar{n}_1^{(k)} \bar{n}_2^{(k+\Delta)}} \tag{5.10}$$

2 Note that in a single interval of data acquisition, $n_1^{(k)}$ can only be either 0 or 1 in our case, since the photon detectors we use cannot resolve more than one photon arriving within a bin.

Experimentally, the estimate of this can be calculated using Equation 5.9 and Equation 5.7 as,

$$\frac{N^2 \sum_k^{N-\Delta} n_1^{(k)} n_2^{(k+\Delta)}}{N - \Delta \sum_k^N n_1^{(k)} \sum_l^N n_2^{(l)}}. \tag{5.11}$$

The expressions given so far are applicable to any two fields indexed 1 and 2. For the second-order cross-correlation between the down-converted signal and idler fields, the indices 1 and 2 become $s$ and $i$ to indicate the signal and idler fields respectively.

For all measurements described in this thesis, we detect signal and/or idler photons with avalanche photodiodes (APDs- Perkin Elmer SPDC-AQ4C) that have a quantum efficiency of $\approx 50\%$. The detection events are time tagged using a field programmable gate array (FPGA- Arty A7-35T: Artix-7, XC7A35TICSG324-1L from Xilinx, programmed using the Xilinx Software Development Kit version 2018.3), programmed as a time-to-digital converter (TDC) with 625 ps resolution. Thus, $t_b = 625\,\mathrm{ps}$ for our experiments. The detectors have a dark count rate of $\sim 500\,\mathrm{counts\,s^{-1}}$. The chopper present in the CE-SPDC system is always on for reasons explained in the previous chapter. For each measurement, data was acquired for a total integration time $T_i$, which is related to the maximum number of bins $N$, according to $N = T_i/t_b$. The chopper has a duty cycle of 32%. This means that out of the total integration time reported in measurements here, photons were collected only for 32% of the time. All correlation measurements reported in this thesis were performed with the chopper on at a frequency of $\sim$ 100 Hz and reported rates of singles or coincidences are always the rates averaged over the chopper cycle. The values of coincidences $n_{coinc}(t_b\,\Delta)$ are reported for a range of delays $(t_b\,\Delta)$ within a coincidence interval $T_{coinc}$ such that $t_b\,\Delta \in [-\frac{T_{coinc}}{2}, \frac{T_{coinc}}{2}]$.

Assuming independent arrival times for the signal and idler, the rate of accidental coincidence between the signal and idler, within a certain coincidence interval is

$$n_{acc} = \frac{\sum_k n_i^{(k)}}{T_i} \frac{\sum_l n_s^{(l)}}{T_i} T_{coin}. \tag{5.12}$$

Coincidences from background was measured to be around $0.1\,\mathrm{counts\,s^{-1}}$ over a 200 ns coincidence window.

### 5.2.1 Heralding efficiency

SPDC is not a deterministic source of single photons. However, since the down-converted photons are produced in pairs, the detection of one down-converted photon "heralds"

the presence of the other. The heralding efficiency of a source, $\eta_H$ is the probability that a single photon is delivered given the detection of a herald photon [120]. It is independent of the detection of the *heralded* photon. To avoid confusion, the heralding photon can also be called the trigger photon. The heralding efficiency is calculated as the ratio of the total coincidences over all delays[3] to the total number of trigger photons detected. If we take the idler as the trigger and the signal as the heralded photon, the probability of having a signal available given the detection of the idler $P_{s|i}$ is [120],

$$P_{s|i} = \eta_H = \frac{\sum_\Delta n_{coin}(t_b\,\Delta)}{\eta_{D_s}\sum_k n_i^{(k)}} = \frac{P_{c|i}}{\eta_{D_s}}, \tag{5.13}$$

where $\eta_{D_s}$ is the quantum efficiency of the detector for the signal and $P_{c|i}$ is the probability of detecting a coincidence, conditioned on having detected an idler. For $P_{Loss_j}$ being the probability that the signal photon is lost in an optical element or interface indexed j, $P_{s|i}$ can also be calculated as $\prod_j(1 - P_{Loss_j})$, where the product includes each element in the signal arm from the generation in the crystal to just before the detection.

### 5.2.2 Coincidence rate

The coincidence rate $R_{coin}$, is the ratio of the total coincidences detected per unit time per unit pump power. Since the brightness from SPDC scales linearly with pump power $P_p$,

$$R_{coin} = \frac{\sum_\Delta n_{coin}(t_b\,\Delta)}{T_i\,P_p}. \tag{5.14}$$

## 5.3 $G^{(2)}_{s,i}(t_s, t_i)$ AND THE TWO-PHOTON JSA

The spectral amplitude of an optical field $s(\omega)$ is defined as the Fourier transform (FT) of the time-varying optical electric field and the power spectral density $S(\omega) = |s(\omega)|^2$, is the energy in the field per unit bandwidth. By the Wiener-Khinchin theorem, the spectral density function and the first-order correlation of a field form a Fourier pair,

$$S(\omega) = \frac{1}{\sqrt{2\pi}}\int_{-\infty}^{\infty} d\tau\; G^{(1)}(\tau)e^{i\omega\tau}. \tag{5.15}$$

3 In practice a large coincidence interval is chosen.

Similarly, the second-order cross-correlation function between the signal and idler photons in a down-converted pair is closely related to the JSA which is the function describing their joint spectrum. To show this, we analyse the $G^{(2)}_{s,i}$ when the the two-photon state from SPDC is the input. As seen previously, the signal-idler two-photon state from SPDC is described by

$$|\psi_i\rangle = \int d\omega_i \int d\omega_s f(\omega_s, \omega_i)\, \hat{a}^\dagger_s(\omega_s)\, \hat{a}^\dagger_i(\omega_i)\, |0_s, 0_i\rangle\,. \tag{5.16}$$

where $f(\omega_s, \omega_i)$ is the JSA. The detection of a photon each in the signal and idler mode will annihilate both the photons and leave the state in the vacuum state, so $|\psi_f\rangle = |0_s, 0_i\rangle$. The $G^{(2)}_{s,i}(t_s, t_i)$ is then,

$$\begin{aligned} G^{(2)}_{s,i}(t_s, t_i) &= \left|\langle 0_s, 0_i|\, \hat{E}^{(+)}_i(t_i)\hat{E}^{(+)}_s(t_s)\, |\psi_i\rangle\right|^2 \\ &= \left|\langle 0_s, 0_i|\, \hat{E}^{(+)}_i(t_i)\hat{E}^{(+)}_s(t_s) \int d\omega_i \int d\omega_s f(\omega_s, \omega_i)\right. \\ &\quad \left.\times\, \hat{a}^\dagger_s(\omega_s)\, \hat{a}^\dagger_i(\omega_i)\, |0_s, 0_i\rangle\right|^2 \\ &\propto \left|\, \langle 0_s, 0_i| \int d\omega'_s \int d\omega'_i \int d\omega_i \int d\omega_s\, e^{-i\omega'_s t_s} e^{-i\omega'_i t_i}\right. \\ &\quad \left.\times f(\omega_s, \omega_i)\hat{a}_s(\omega'_s)\hat{a}_i(\omega'_i)\hat{a}^\dagger_s(\omega_s)\hat{a}^\dagger_i(\omega_i)\, |0_s, 0_i\rangle\, \right|^2. \end{aligned} \tag{5.17}$$

Using the commutation relations $[\hat{a}_\epsilon(\omega_\epsilon), \hat{a}^\dagger_\nu(\omega'_\nu)] = \delta_{\epsilon,\nu}\delta(\omega_\epsilon - \omega'_\nu)$ for Kronecker delta function $\delta_{\epsilon,\nu}$ and Dirac delta function $\delta(\omega_\epsilon - \omega'_\nu)$ when $\nu, \epsilon \in \{s, i\}$,

$$\begin{aligned} G^{(2)}_{s,i}(t_s, t_i) &\propto \left|\int d\omega_i \int d\omega_s f(\omega_s, \omega_i) e^{-i\omega_s t_s} e^{-i\omega_i t_i}\right|^2 \\ &\propto |\tilde{f}(t_s, t_i)|^2. \end{aligned} \tag{5.18}$$

In the last line we have introduced the Joint Temporal Amplitude (JTA) which is the 2-D FT of the JSA,

$$\begin{aligned} \tilde{f}(t_s, t_i) &\equiv \frac{1}{2\pi} \int d\omega_i \int d\omega_s f(\omega_s, \omega_i) e^{-i\omega_s t_s} e^{-i\omega_i t_i} \\ &\propto \langle 0, 0|\, \hat{E}^{(+)}_i(t_i)\hat{E}^{(+)}_s(t_s)\, |\psi_i\rangle\,. \end{aligned} \tag{5.19}$$

The second order cross-correlation function is proportional to the magnitude squared of the JTA, and thus can also be called the Joint Temporal Intensity (JTI).

For the specific case where the SPDC pump is monochromatic with a frequency $\omega_p$, following Equation 2.7, the JSA can be expanded as $f(\omega_s, \omega_i) = \delta(\omega_p - \omega_s - \omega_i)g(\omega_s, \omega_i)$, where $g(\omega_s, \omega_i)$ is the crystal phase matching function. Consequently, the JTA can be written as,

$$\tilde{f}(t_s, t_i) = \frac{1}{2\pi}\int d\omega_i \int d\omega_s \, \delta(\omega_p - \omega_s - \omega_i)g(\omega_s, \omega_i)e^{-i\omega_s t_s}e^{-i\omega_i t_i} \tag{5.20}$$

Expressing the JTA in terms of a delay $\tau$ between the signal detection at $t_s = t$ and the idler at $t_i = t + \tau$

$$\begin{aligned}
\tilde{f}(\tau) &= \frac{1}{2\pi}\int d\omega_i \int d\omega_s \, \delta(\omega_p - \omega_s - \omega_i)g(\omega_s, \omega_i)e^{-i\omega_i \tau}e^{-i(\omega_s+\omega_i)t} \\
&\propto \int d\omega_s \, g(\omega_s, \omega_p - \omega_s)e^{-i(\omega_p-\omega_s)\tau}e^{-i\omega_p t} \\
&= e^{-i\omega_p(t+\tau)}\int d\omega_s \, g(\omega_s, \omega_p - \omega_s)e^{i\omega_s \tau}.
\end{aligned} \tag{5.21}$$

Here $e^{-i\omega_p(t+\tau)}$ is a global phase that does not affect the cross-correlation measurement, leaving,

$$G^{(2)}_{s,i}(\tau) \propto \left|\int d\omega_s \, g(\omega_s, \omega_p - \omega_s)e^{i\omega_s \tau}\right|^2. \tag{5.22}$$

We see that in this scenario of a monochromatic pump, the $G^{(2)}_{s,i}$ as a function of the delay $\tau$ between the signal and idler arrival times, is directly related to the 1-D Fourier transform of the JSA expressed exclusively in terms of either the signal or idler frequency.

As a consequence of this close relationship between the spectral function describing two fields and the second-order intensity cross-correlation between those two fields, the $G^{(2)}_{s,i}(\tau)$ function will vary depending on the two-photon JSA describing the signal-idler spectrum. In the following sections, we analyse the $G^{(2)}_{s,i}(\tau)$ from CE-SPDC and filtered CE-SPDC, and discuss how features in the $G^{(2)}_{s,i}$ relate to features in the spectrum. Going beyond the Fourier relations, we also try to provide a more intuitive explanation of the the features observed in the $G^{(2)}_{s,i}(\tau)$ through an analysis of down-conversion process in the time domain. We then present experimental results from measurements performed with our source. Throughout the discussion, we replace $\omega_i = \omega_p - \omega_s$ to restrict it to the monochromatic-pump scenario.

### 5.3.1 $G^{(2)}_{s,i}(\tau)$ from CE-SPDC

From Equation 2.32, the JSA for a two-photon state from CE-SPDC, $f_C$, is the product of three functions, one being the two-photon JSA from single-pass SPDC and one each for the signal and idler frequency response in the cavity. The JTA is a FT of the JSA as seen in Equation 5.19. Thus, due to the convolution theorem, the JTA from CE-SPDC $\widetilde{f}_C$ is a convolution of the individual FTs of each of these functions, giving,

$$\tilde{f}_C(\tau) \propto \left(\widetilde{f}_{NB} * \widetilde{\Gamma}(\gamma_s, \omega_s^0, FSR_s) * \widetilde{\Gamma}(\gamma_i, \omega_i^0, FSR_i)\right)(\tau). \tag{5.23}$$

Here $*$ indicates convolution and $\widetilde{f}$ is the FT of a function $f$. In particular, $\widetilde{\Gamma}(\gamma_\epsilon, \omega_\epsilon^0, FSR_\epsilon)(\tau)$ is the FT with respect to $\omega_\epsilon$ of $\Gamma(\omega_\epsilon, \gamma_\epsilon, \omega_\epsilon^0, FSR_\epsilon)$ for $\epsilon \in \{s, i\}$. To understand the shape of the $G^{(2)}_{s,i}$ from CE-SPDC, we first look at the magnitude squared of the FTs of each of the functions present in the JSA from CE-SPDC.

The sinc function from phase matching in $f_{NB}(\omega_s, \omega_p - \omega_s)$ determines the maximum range of frequencies present in the spectrum from CE-SPDC. In this sense it is the "broadest" feature in frequency domain. The magnitude squared of its FT is the rectangular or "box" function with a width given by the signal-idler relative propagation delay $\tau_o$ in the crystal (related to the SPDC bandwidth according to Equation 2.18), as shown in Figure 5.1. This is the "narrowest" feature in time domain and is usually not resolved in experiment. To intuitively understand the "box" shaped signal-idler arrival time distribution, we analyse the time-domain picture of SPDC where the photons are produced at the same time and position in the crystal. Since the photon pair has an equal probability of being generated at any point within the length of the crystal, they can be generated at the very end of the crystal and have the least delay between them, or they can be generated at the beginning of the crystal and acquire a maximum delay $\tau_o$ between them by the time they leave the crystal. They can also equally well be generated anywhere in the crystal and acquire an intermediate value of delay. This results in a box shaped distribution of arrival times.

The other factors of $f_C$ are $\Gamma$ functions that describe the signal/idler cavity frequency-response functions. We analyse the FTs of them. The $\Gamma$ function is a convolution of a comb of Dirac delta functions with comb spacing equal to the FSR, and a single complex Lorentzian [104]

$$\mathcal{L}(\omega, \gamma) = \frac{\gamma/2}{\frac{\gamma}{2} - i\omega}. \tag{5.24}$$

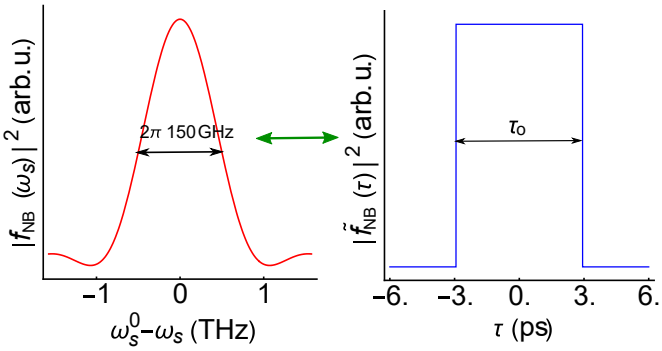


Figure 5.1: Illustration of JSI and JTI from free-space SPDC with a monochromatic pump. Left: JSI which is the $\text{sinc}^2$ function plotted against the detuning of $\omega_s$ from $\omega_s^0$- the frequency at which perfect phase matching is satisfied. The SPDC bandwidth $\Delta\omega_{spdc} = 2\pi\times150$ GHz. Right: box function with a width $\tau_o = \frac{2\pi\,0.88}{\Delta\omega_{spdc}} \approx 6$ ps. Green arrow indicates a Fourier relation between the amplitude functions which give the intensity functions plotted on either side.

Once again, by the convolution theorem, the FT of $\Gamma$ is a product of the FT of a comb (which is also a comb) and the FT of $\mathcal{L}$. We analyse the FTs in parts. Figure 5.2 shows the temporal intensity function if the spectral amplitude function was 1) $f_1(\omega_s) = \mathcal{L}(\omega_s,\gamma_s)$ i.e., a single complex Lorentzian, 2) $f_2(\omega_s) = \mathcal{L}(\omega_s,\gamma_s)\,\mathcal{L}(\omega_p-\omega_s,\gamma_i)$ i.e., a product of 2 complex Lorentzians with different line-widths (one each for a single signal and idler resonance) and 3) $f_3(\omega_s) = \sum_m \mathcal{L}(\omega_s - m\,\text{FSR}_s,\gamma_s)$ a comb of complex Lorentzians, which is the same as a $\Gamma$ function. In scenario 1), $|\widetilde{\mathcal{L}}(\tau,\gamma_s)|^2$ gives the probability of detecting a single signal photon outside the cavity given that at $\tau = 0$ there was a signal photon inside the cavity. It drops exponentially in time according to $|\widetilde{\mathcal{L}}(\tau,\gamma_s)|^2 \propto e^{-\gamma_s\tau}$, with a decay time (Equation 2.44) $\tau_d = 1/\gamma_s$. Whenever a function describing the spectrum contains a single Lorentzian with linewidth $\gamma$ as a factor which describes the narrowest feature in frequency, $\widetilde{\mathcal{L}}(\tau,\gamma_s)$ is the broadest feature in time.

In scenario 2) from Figure 5.2, $f_2(\omega_s) = \mathcal{L}(\omega_s,\gamma_s)\mathcal{L}(\omega_p-\omega_s,\gamma_i)$, which represents the signal spectrum when influenced by the idler resonance in the cavity. It is product of a single complex Lorentzian each for the signal and idler with different linewidths. The resulting spectral shape is no longer exactly a Lorentzian and has a reduced FWHM $\gamma$, which is less than both $\gamma_s$ and $\gamma_i$ as illustrated in Figure 5.2. If $\gamma_s \approx \gamma_i$, $\gamma = \gamma_{tp} \approx 0.64\gamma_s$, $\gamma_{tp}$ is the two-photon linewidth defined in Equation 2.45. $|\widetilde{f_2}(\tau)|^2$ is

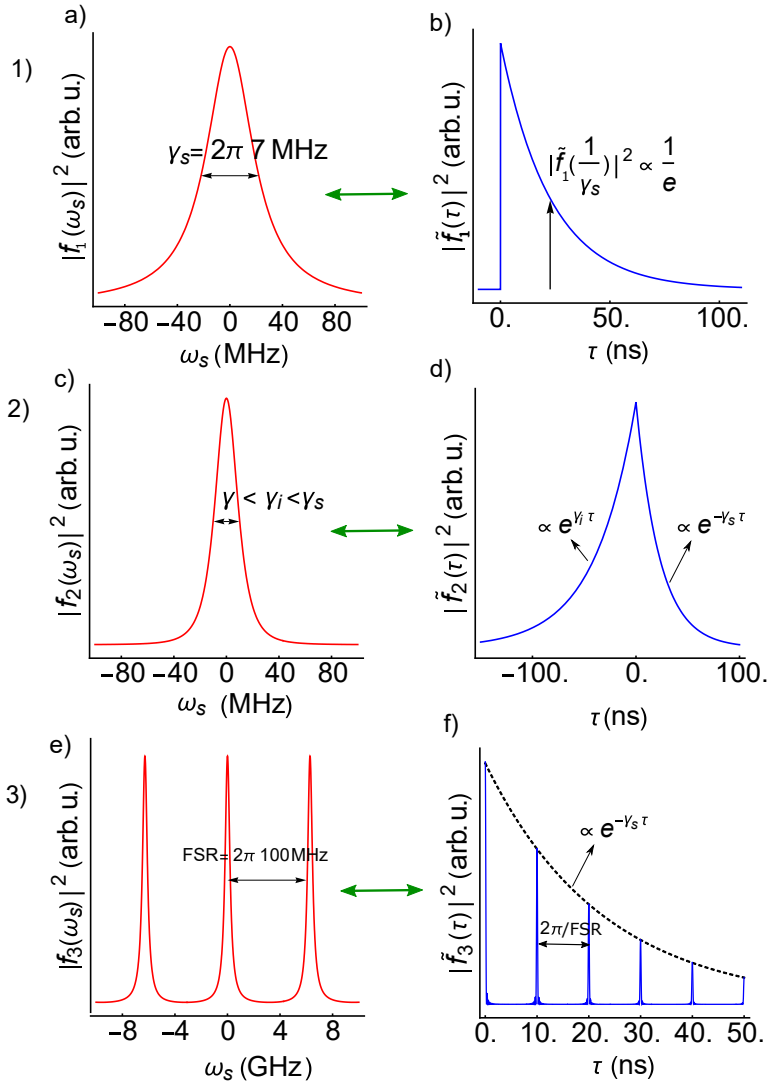


Figure 5.2: Illustration of spectral intensities (left column) and associated temporal intensities (right column) for various spectral amplitude functions that are factors of $f_C$. Three cases are shown: 1) $f_1(\omega_s) = \mathcal{L}(\omega_s, \gamma_s)$ for $\gamma_s = 2\pi \times 7\,\mathrm{MHz}$, 2) $f_2(\omega_s) = \mathcal{L}(\omega_s, \gamma_s)\mathcal{L}(\omega_p - \omega_s, \gamma_i)$ for $\gamma_s = 2\pi \times 7\,\mathrm{MHz}$, $\gamma_i = 2\pi \times 4\,\mathrm{MHz}$ and 3)$f_3(\omega_s) = \sum_m^M \mathcal{L}(\omega_s - m\,\mathrm{FSR}_s, \gamma_s)$ for $\mathrm{FSR}_s = 2\pi \times 100\,\mathrm{MHz}$ and $\gamma_s = 2\pi \times 7\,\mathrm{MHz}$. Discussion in text. While f) has been plotted for a fixed value of M, in reality $M \to \infty$ and the lines in the comb in f) get narrower as M increases.

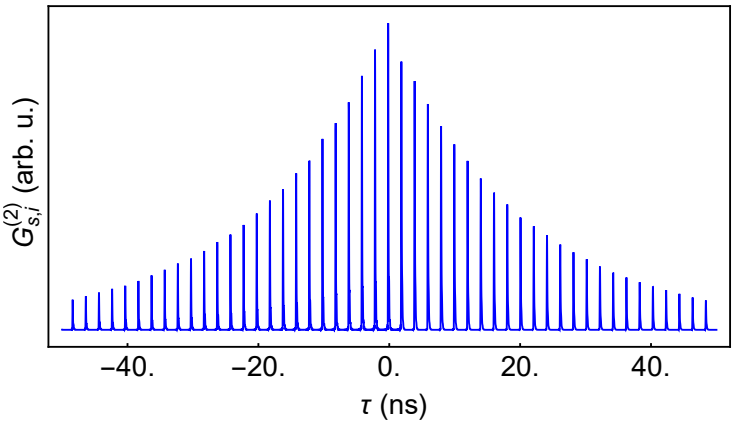


Figure 5.3: Simulated $G^{(2)}_{s,i}$ from CE-SPDC. Function in Equation 5.25 plotted for $\gamma_s = \gamma_i = 2\pi \times 7.6\,\mathrm{MHz}$, $\mathrm{FSR}_i = 2\pi \times 494.25\,\mathrm{MHz}$, $\mathrm{FSR}_s = 2\pi \times 497.75\,\mathrm{MHz}$ and $\tau_o = 6\,\mathrm{ps}$.

a double exponential with the decay time for positive delays being the inverse of one linewidth and the decay time for negative delays the inverse of the other linewidth. While the probability that either a signal or idler from a pair individually leaves the cavity decays exponentially at the respective decay rate, the JTI $|\widetilde{f_2}(\tau)|^2$ describes the joint probability of detecting both them separated by a delay $\tau$. For positive values of $\tau$ the JTI describes the probability of detecting a signal at a time $\tau$ after the detection of an idler, and at negative values of $\tau$ the JTI is proportional to the probability of detecting an idler after a delay $|\tau|$ from the detecting a signal.

As a last step before presenting the final form of the $G^{(2)}_{s,i}$ from CE-SPDC, we look at the shape of $|\widetilde{f_3}(\tau)|^2$ when $f_3(\omega_s)\sum_m^M = \mathcal{L}(\omega_s - m\,\mathrm{FSR}_s, \gamma_s)$ i.e., a series of repeating complex Lorentzians describing the multi-mode character of the cavity frequency response. This is equal to $\Gamma(\omega_s, \gamma_s, \omega_s^0, \mathrm{FSR}_s)$ when $M \to \infty$. See part 3) in Figure 5.2. As mentioned in the beginning of the paragraph, $\widetilde{\Gamma}$ is the product of a comb and $\widetilde{\mathcal{L}}(\tau, \gamma_s)$. The temporal intensity is described by a comb with teeth spaced by $2\pi/\mathrm{FSR}_s$ and enveloped by the exponentially decaying $|\widetilde{\mathcal{L}}(\tau, \gamma_s)|^2$ function. In the time domain picture, light can exit the cavity only after an integer number of round trips, a situation that is reflected in the fact that the comb spacing is equal to the round trip time (defined in Equation 2.38).

Convolving all these individual FTs as shown in Equation 5.23, a final expression for $G^{(2)}_{s,i}(\tau)$ from CE-SPDC $= |\widetilde{f_C}(\tau)|^2$ can be obtained [102],

$$G^{(2)}_{s,i}(\tau) \propto \left| \sum_{m_i, m_s} \frac{1}{\Upsilon_s + \Upsilon_i} \begin{cases} e^{-\Upsilon_s[\tau - \frac{\tau_o}{2}]} \mathrm{sinc}\left(i\frac{\tau_o}{2}\Upsilon_s\right), & \tau \geqslant \tau_0/2 \\ e^{\Upsilon_i[\tau - \frac{\tau_o}{2}]} \mathrm{sinc}\left(i\frac{\tau_o}{2}\Upsilon_i\right), & \tau < \tau_o/2 \end{cases} \right|^2. \quad (5.25)$$

Here $\Upsilon$ relates to the linewidth $\gamma$, mode index ($m$) and angular FSR of the signal/idler mode according to,

$$\Upsilon_\epsilon = \frac{\gamma_\epsilon}{2} + i\, m_\epsilon \mathrm{FSR}_\epsilon \quad (5.26)$$

for $\epsilon \in \{s, i\}$.

Figure 5.3 shows a numerically calculated plot of the $G^{(2)}_{s,i}(\tau)$ from CE-SPDC, for measured signal-idler linewidths and FSRs of our CE-SPDC cavity. The multiple frequency modes in the signal and idler spectrum translate to a comb under a double exponential envelope, similar to $|\widetilde{f_3}(\tau)|^2$. For positive delays, the teeth are spaced by $2\pi/\mathrm{FSR}_s$ and the envelope describes the exponential decay in time of signal-intensity in the cavity. For negative delays, the teeth are spaced by $2\pi/\mathrm{FSR}_i$ and the envelope describes the exponential decay in time of the idler's intensity in the cavity. Similar to $|\widetilde{f_2}(\tau)|^2$ the $G^{(2)}_{s,i}(\tau)$ is proportional to the joint probability of detecting the signal and idler at times $t_s$ and $t_i$, respectively, separated by a delay $\tau = t_i - t_s$. At positive values of $\tau$, the comb can be understood to be the result of the signal photon leaving the cavity after more round trips than its partner idler. Similarly, at negative values of $\tau$, the comb is a consequence of the idler photon staying for more round trips in the cavity as compared to its partner signal. The peak at zero time implies both signal and idler in a pair leave after the same number of round trips.

### *Experimental results*

The CE-SPDC source was pumped with 350 $\mu W$ of pump power. The signal and idler photons from the CE-SPDC source were separated using a polarising beam splitter (PBS), detected in APDs and their coincidences measured as described in section 5.2. Results are shown in Figure 5.4. The results are in agreement with the numerically calculated plot in Figure 5.3. However, the comb teeth in section 5.2 are not arbitrarily fine like the teeth in Figure 5.3 due to the finite time resolution of the detection process. The round trip time in the cavity for the signal and idler is $2\pi/\mathrm{FSR}_s \approx 2\pi/\mathrm{FSR}_i \approx 2$ ns

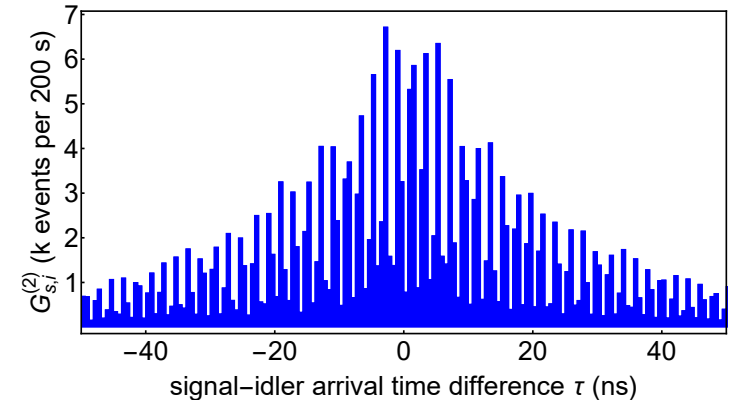


(a)

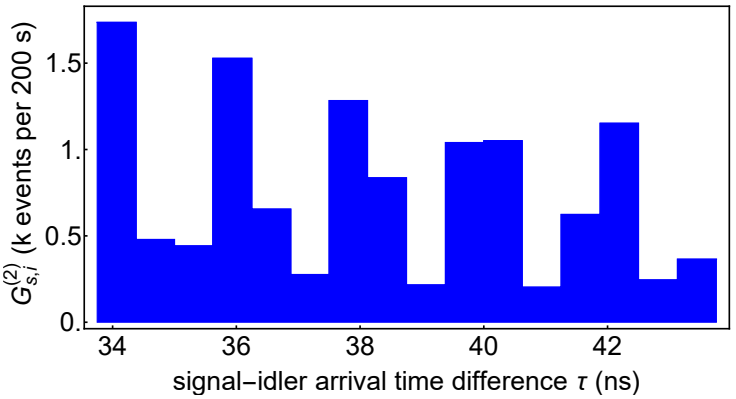


(b)

Figure 5.4: Measurement of signal-idler intensity cross-correlation from CE-SPDC. Plots show distribution of signal-idler coincidences at various delays, when CE-SPDC was pumped with 350 $\mu W$ of pump power and data collected for an integration time of 200 s. (a) Shows the coincidence distribution within a coincidence interval of 100 ns. (b) The same distribution zoomed-in between 30-55 ns to better visualise the 2 ns separation between the peaks.

and is resolved by the 625 ps timing resolution. The resolution, however, is insufficient to observe the difference in the FSRs.

### 5.3.2 $G^{(2)}_{s,i}(\tau)$ from filtered CE-SPDC

Equation 3.8 from chapter 3 gives the modified two-photon JSA $f_F(\omega_s, \omega_i)$, from filtering the CE-SPDC output to select a single frequency mode each for the signal and idler. In the monochromatic pump scenario, $f_F(\omega_s, \omega_p - \omega_s)$ is proportional to the function $f_2(\omega_s)$ illustrated in Figure 5.2. The $G^{(2)}_{s,i}(\tau)$ for a filtered single-mode CE-SPDC source, proportional to $|\widetilde{f_F}(\tau)|^2$ is,

$$G^{(2)}_{s,i}(\tau) \propto |\xi|^2 \frac{\gamma_i^2 \gamma_s^2}{(\gamma_i + \gamma_s)^2} \times \begin{cases} e^{\tau\gamma_i} & \tau \leqslant 0 \\ \\ e^{-\tau\gamma_s} & \tau > 0 \end{cases} . \tag{5.27}$$

Here $\xi$, comes from Equation 3.8.

The normalised second order cross-correlation function for a filtered single-mode CE-SPDC source, is related to the pair production rate $\mathcal{R}$ according to, [121]

$$g^{(2)}_{s,i}(\tau) = \begin{cases} 1 + \frac{\gamma_i}{2\mathcal{R}} e^{\tau\gamma_i} & \tau \leqslant 0 \\ \\ 1 + \frac{\gamma_s}{2\mathcal{R}} e^{-\tau\gamma_s} & \tau > 0 \end{cases} \tag{5.28}$$

Similar to the previous section, we use the time-domain picture to understand the shape of the $G^{(2)}_{s,i}$ in Equation 5.27. This function has been derived on the condition that the decay times of the FP filters used for filtering are much shorter than the signal-idler decay times in the CE-SPDC cavity (refer conditions for single mode output in subsection 3.1.1). Thus, the $G^{(2)}_{s,i}$ function continues to be dominated by the double exponential envelop pertaining to the CE-SPDC cavity decay rates. However, from the conditions in subsection 3.1.1, the decay times of the FP filters used have to be longer than the round trip times in the CE-SPDC cavity. As discussed in the previous section, the comb in the unfiltered CE-SPDC $G^{(2)}$ (Equation 5.25) is a consequence of the the signal/idler photon in a down-converted pair exiting the CE-SPDC cavity after more round trips as compared to its parter. Introducing a filter with a long decay time erases (or reduces the resolution of) information about the number of round trips taken by a down-converted photon in the CE-SPDC cavity. Thus the shape of the $G^{(2)}_{s,i}$ is a smooth double exponential if the conditions for a single frequency mode output from a filtered CE-SPDC source are satisfied.

**Correlation time**: The two-photon correlation time is defined as the FWHM of $G^{(2)}_{s,i}(\tau)$ [32, 99]. It gives an estimate of the time-window over which the probability of

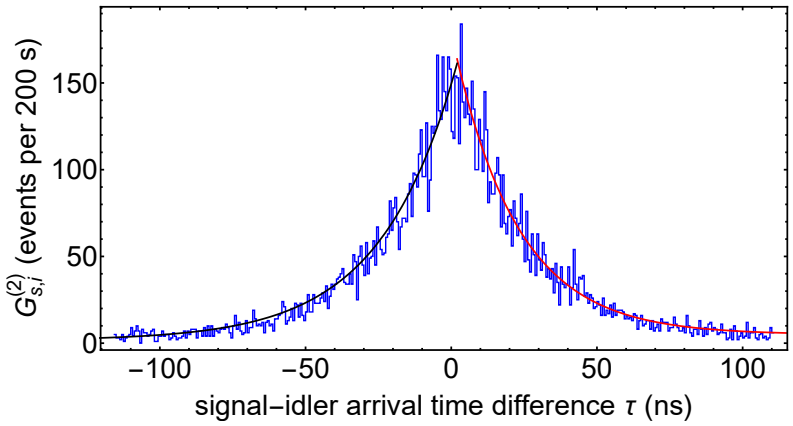


Figure 5.5: Measurement of signal-idler intensity cross-correlation from CE-SPDC with a single signal mode filtered. Plots show distribution of signal-idler coincidences at various delays, when CE-SPDC was pumped with 350 $\mu W$ of pump power and data collected for an integration time of 200 s. The experimental data are fit with exponential decays for positive and negative delays to obtain the signal and idler linewidths respectively.

detecting both photons from a down-converted pair is significant. For the $G^{(2)}_{s,i}(\tau)$ in Equation 5.27, the correlation time is,

$$\tau_c = 0.69/\gamma_i + 0.69/\gamma_s. \tag{5.29}$$

When $\gamma_s \approx \gamma_i$,

$$\tau_c \approx 0.89/\gamma_{tp}, \tag{5.30}$$

where $\gamma_{tp}$ is the two-photon linewidth defined in Equation 2.45.

### *Experimental results*

The CE-SPDC source was pumped with 350 $\mu W$ of pump power. The signal and idler photons were split using a PBS after the source, and a single signal frequency mode selected using the FP filter described in section 3.2. The down-converted photons were detected in APDs and coincidences counted as described in section 5.2. As seen from the results shown in Figure 5.5, when the filter is introduced, the comb structure previously seen in Figure 5.4 is washed out from the $G^{(2)}_{s,i}$. This indicates the absence of signal frequency components detuned from the filtered mode by less than $\pm$ 1.6 GHz (the

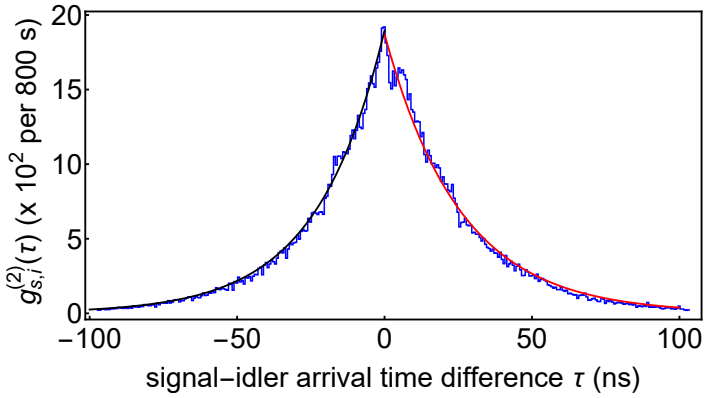


Figure 5.6: Measurement of the normalised signal idler cross-correlation from the filtered CE-SPDC system. Plot shows $g^{(2)}_{s,i}(\tau)$ when both the signal and idler are split and filtered after CE-SPDC, to contain a single frequency mode each. Measurement was performed with 500 $\mu W$ of pump power and for a total integration time of 800 s. The experimental data are fit with Equation 5.28 to obtain the signal and idler linewidths and the pair production rate. The error bars are small in comparison to the plot scales.

inverse of the 625 ps time resolution), as expected from the predicted filter behaviour. In combination with the results shown in Figure 3.7, where the absence of unwanted frequency components outside a 3 GHz window was demonstrated, this leads us to conclude that the output after the filter can be considered to contain a single spectral mode for all practical purposes. Refer chapter 6 for a quantitative analysis of the power contained in unwanted frequency modes after the filtering. Fitting Equation 5.27 to the experimental data gives the cavity relaxation rates $\gamma_s = 2\pi \times 7.0(3)$ MHz and $\gamma_i = 2\pi \times 6.2(1)$ MHz. The correlation time of the two photons is $\tau_c = 33(4)$ ns.

We also measure the normalised second-order cross- correlation function $g^{(2)}_{s,i}(\tau)$. For this, two filters are used each in the signal and idler arm to select a single mode-pair. The filtered signal and idler are detected in APDs and Equation 5.10 is used to calculate the $g^{(2)}_{s,i}$. The measurement is repeated for various pump powers. A representative result is shown in Figure 5.6. Fitting Equation 5.28 to all the data, we get $\gamma_s = 2\pi \times 6.98(4)$ MHz and $\gamma_i = 6.16(24)$ MHz. We estimate the two-photon linewidth to be $\gamma_{tp} \approx 0.64 \times \gamma_{avg} = 2\pi \times 4.2$ MHz using the average of the signal

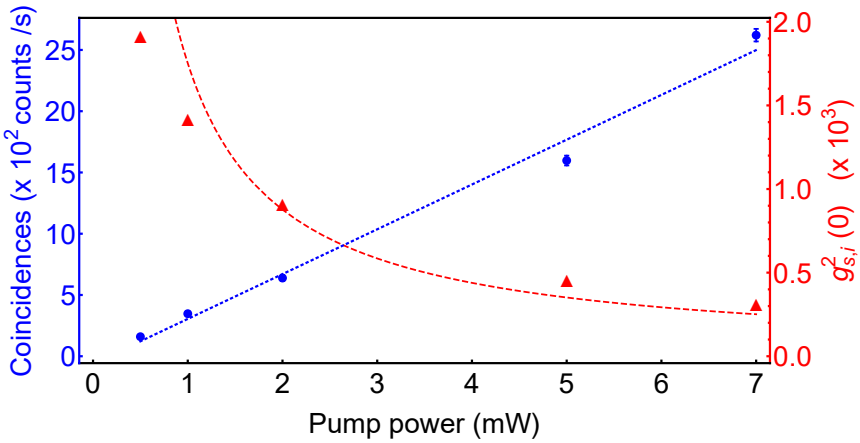


Figure 5.7: Power dependence of total coincidences detected (right axis, blue circles) and $g^{(2)}_{s,i}(0)$ (left axis, red, triangles). All measurements were performed over an 800 s integration time and the total coincidences summed over a coincidence interval of 200 ns. Refer text for details on fits. Error bars in the $g^{(2)}_{s,i}(0)$ plot are small in comparison to the plot scale.

and idler linewidths $\gamma_{avg}$ and following the definition of the two-photon linewidth in Equation 2.45.

The orange triangles in Figure 5.7 show $g^{(2)}_{s,i}(0)$ for various pump powers $P_p$. The data are fit with $1 + \gamma_{avg}/(2\beta P_p)$. From the fit (orange dashed line) we estimate the pair-production rate per unit pump in the crystal, $\beta = \frac{\mathcal{R}}{P_p} = 11(5) \times 10^3\ pairs\ mW^{-1}\ s^{-1}$ in the central mode that we filter and detect. A pair production rate of $3.4 \times 10^6\ pairs\ mW^{-1}\ s^{-1}$ in a total of 300 frequency modes within the SPDC bandwidth, was reported in [105] where the same CE-SPDC cavity was operated such that difference in the signal-idler FSRs was compensated. Our result for the pair product rate per mode is in rough agreement with this value as $3.4 \times 10^6/300 = 11.3 \times 10^3$ . We note that the ~ 300 participating modes in the compensated configuration is a rough estimate that does not take precise account of the distribution of brightness among the cavity modes.

Blue circles in Figure 5.7 show the total number of coincidences $\sum_\Delta n_{coin}(\Delta t_b)$ detected in a coincidence interval $T_{coin} = 200\,ns$ for various pump powers. The data

are fit with a linear function of the pump power (blue dotted line) to obtain the coincidence rate (Equation 5.14) $R_{coin} = 336(25)\,counts\,s^{-1}\,mW^{-1}$. All experimental data reported is averaged over the chopper duty cycle of 32%. This implies a coincidence rate of $1050\,counts\,s^{-1}\,mW^{-1}$ when the chopper is open. The accidental coincidences are consistently 3 orders of magnitude less than the measured coincidences and so have been neglected.

From the cross-correlation measurements, we get $P_{c|i} = 18(3)\%$ using Equation 5.13 and a heralding efficiency of $\eta_H = 36(6)\%$ for $\eta_{D_s} = 50\%$. This matches our estimated heralding efficiency of 34% based on the following values for the transmission ($1 - P_{Loss_j}$ in subsection 5.2.1) of a signal photon through various optical elements until it reaches the detector: cavity escape efficiency ($\eta = 72\%$), coupling efficiency into fiber after the CE-SPDC cavity (65%), maximum transmission through fiber to fiber connectors ($\sim 90\%$), on resonance transmission through the FP filter cavity ($\sim 90\%$) and fiber and coupling efficiency into fiber after the filter ($\sim 90\%$ ).

The measured coincidence rate and the quantum efficiency of the detectors imply $\sim 4000\,pairs\,s^{-1}\,mW^{-1}$ of correlated photon-pairs in fiber and $720\,s^{-1}\,mW^{-1}$ of heralded signal photons available for cold atom experiments when the chopper is open.

## 5.4 SECOND ORDER AUTOCORRELATION FUNCTION

The autocorrelation of a field quantifies the extent to which it is correlated with itself. The second order intensity autocorrelation function gives the distribution of photon detection times in the same mode, as a function of the delay $\tau$ between the detections. The normalised form of this is [122],

$$g^{(2)}_{\epsilon,\epsilon}(\tau) = \frac{\left\langle \hat{E}^{(-)}_{\epsilon}(t)\hat{E}^{(-)}_{\epsilon}(t+\tau)\hat{E}^{(+)}_{\epsilon}(t+\tau)\hat{E}^{(+)}_{\epsilon}(t)\right\rangle}{\left\langle \hat{E}^{(-)}_{\epsilon}(t+\tau)\hat{E}^{(+)}_{\epsilon}(t+\tau)\right\rangle \left\langle \hat{E}^{(-)}_{\epsilon}(t)\hat{E}^{(+)}_{\epsilon}(t)\right\rangle}, \tag{5.31}$$

where subscript $\epsilon$ is either $s$ for the autocorrelation of the signal mode or $i$ for the idler autocorrelation. The autocorrelation at 0 delay $g^{(2)}_{\epsilon,\epsilon}(0)$ is 2 for a source that exhibits thermal statistics, 1 for a Poissonian source and 0 for a genuine single photon source [122].

The autocorrleation of a field from SPDC shows completely different statistics depending on whether it is heralded or not. In the absence of heralding, the light displays thermal statistics and the photons are bunched [123].

### 5.4.1 Heralded autocorrelation

Suppressing the emission and quantifying the presence of multi-photon components is important for applications that require a genuine single photon source. The probability of generating states with two or more number of pairs from SPDC increases with the pump power. So, it is important to quantify the single-photon character of the heralded mode when SPDC is used as a source for heralded single photons. As mentioned earlier, the autocorrelation at zero delay is zero for an ideal single photon source and this indicates anti-bunching.

For single quantum emitters such as single atoms or single quantum dots, which naturally emit anti-bunched light, anti-bunching can be observed with a Hanbury-Brown and Twiss (HBT) setup, following [11]. The emission from single quantum emitters is anti-bunched because, following the emission of one photon, the emitter is necessarily in a low-energy state, and must wait to be excited before it can emit a second photon. In contrast, SPDC is a parametric process that does not change the state of the material (the nonlinear crystal), and is driven by a pump beam containing many photons. As a result, the emission of a photon pair leaves the source perfectly ready to emit another photon pair. Indeed, through the process of stimulated emission, SPDC is more likely to emit multiple pairs simultaneously, than it is to emit them separated in time. In other words, SPDC output is bunched, not anti-bunched.

Nonetheless, it is possible to create anti-bunched beams by SPDC thorough the process of heralding. Because the signal and idler photons are produced in pairs, detection of a signal photon indicates, or "heralds," the presence of at least one photon in the idler beam. And, assuming the rate of pair production is significantly less than one pair per correlation time, it is unlikely that there is more than one photon in the idler. In this way, detection of a signal heralds an idler state that approximates a single photon state, in the sense that the probability for n=1 photons is reasonably large (limited by the efficiencies of the system), and the probability for more than one photon is very small. This phenomenon can be detected using a three-detector HBT set-up, in which one detector acts as the herald, and the other two, at different outputs of a beam splitter, are used for a correlation measurement, but only when the heralding detector fires.

The first demonstration of anti-bunching from SPDC was by Fasel and team [124] who measured the second order heralded-autocorrelation function to demonstrate this.

The normalised idler-heralded signal autocorrelation function (for two detections at $t_1$ and $t_2$ in the signal arm) is [125]

$$g^{(2)}_{s,s|i}(t_1,t_2|t_i) = \frac{\left\langle \hat{E}_s^{(-)}(t_1)\hat{E}_s^{(-)}(t_2)\hat{E}_s^{(+)}(t_2)\hat{E}_s^{(+)}(t_1)\right\rangle_{pm}}{\left\langle \hat{E}_s^{(-)}(t_1)\hat{E}_s^{(+)}(t_1)\right\rangle_{pm}\left\langle \hat{E}_s^{(-)}(t_2)\hat{E}_s^{(+)}(t_2)\right\rangle_{pm}} \tag{5.32}$$

where subscript $\langle . \rangle_{pm}$ refers to the expectation value over the state post-measurement of an idler at $t_i$, also called the post-selected state.

For an ideal heralded-single photon source, the heralded second order autocorrelation function when $t_1 = t_2 = t_i = t$ (zero delay between detections) is expressed as $g^{(2)}_{s,s|i}(t,t|t) \equiv g^{(2)}_{s,s|i}(0)$ and is equal to zero. It has been shown by Bocquillon and colleagues that $g^{(2)}_{s,s|i}(0) \to 0\big|_{\mathcal{R}\to 0}$, i.e., for an SPDC source anti-bunching is achieved in the low conversion efficiency regime, where the pump power is low and SPDC brightness is low [125]. However for large delays, $g^{(2)}_{c|i}(t_1, t_2 \to \infty|t_i) = 1$. Experimentally, the idler-heralded signal autocorrelation can be measured by splitting the signal arm into two modes indexed s and s′ and using [125, 126]

$$g^{(2)}_{s,s|i}(0,\tau|0) \quad = \quad \frac{\mathcal{N}^{(2)}_{s,s',i}(\tau)\,\mathcal{N}_i}{\mathcal{N}_{s,i}(0)\mathcal{N}_{s',i}(\tau)}. \tag{5.33}$$

Here $\mathcal{N}^{(2)}_{s,s',i}(\tau)$ is the count rate of 3-fold coincidences - one detection each in one signal and the idler arm at the same instant and another detection in the other signal arm with a $\tau$ delay, $\mathcal{N}_i$ is the total singles of the idler detected, $\mathcal{N}_{s,i}(0)$ and $\mathcal{N}_{s',i}(\tau)$ are number of coincidences between each of the signal arms and idler arm with 0 and $\tau$ delays respectively.

### *Experimental Results*

To perform a measurement of the $g^{(2)}_{s,s|i}$, the signal and idler after the CE-SPDC were first split and individually filtered to select a single signal-idler mode pair. Then the signal was then split in a 50:50 beamsplitter (BS) and the transmitted mode detected in an APD we call $\text{APD}_s$ and the reflected mode detected in an APD we call $\text{APD}_{s'}$. The filtered idler was sent to an APD called $\text{APD}_i$. Detection events were collected for various values of pump power.

We perform the following analysis to compare $g^{(2)}_{s,s|i}(0)$ and $g^{(2)}_{s,s|i}(0,\tau|0)$. We count the number of idlers (heralds) detected in the delay between coincidences registered

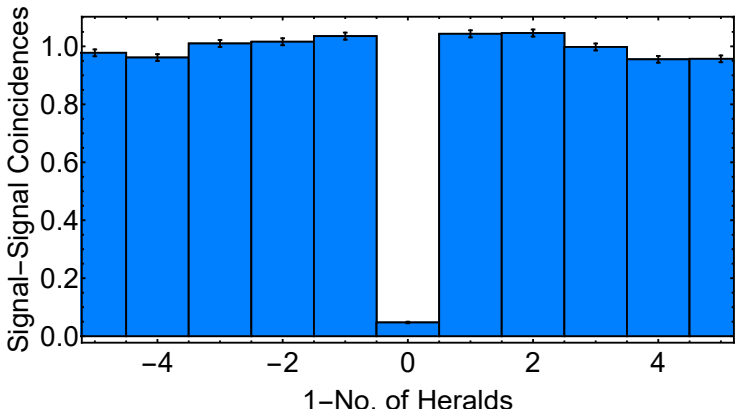


Figure 5.8: Distribution of signal-signal coincidences per number of heralds detected within the coincidence delay. Horizontal axis shows $x = 1-$ number of heralds. Each vertical bar in the histogram associated with bin $x$, shows total number of coincidences between $APD_s$ and $APD_{s'}$ for $1 + x$ heralds detected within the coincidence delay. Measurement was performed for a pump power of 3 $mW$ and an integration time of of 600 s. Data are normalised to the average height of outer bins (which is $7760 \pm 28$ counts). The height of bin $x = 0$, which is the number of signal-signal coincidences in the window between detecting one herald and the next, gives $g^{(2)}_{s,s|i}(0) = 0.05 \pm 0.002$.

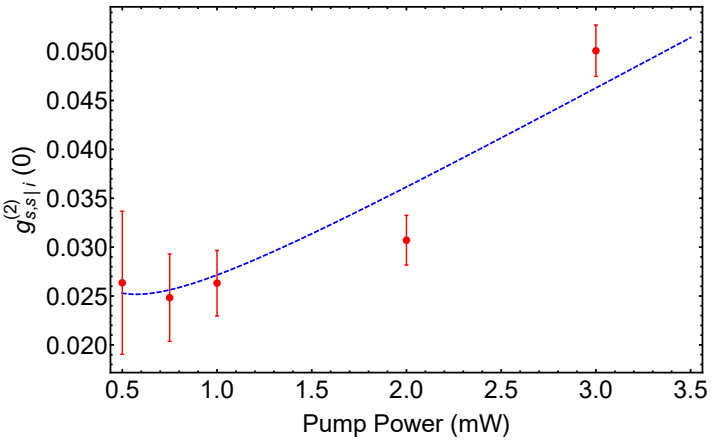


Figure 5.9: The normalised heralded signal autocorrelation as a function of source brightness. Red points calculated as described in text from measurements over 600 s of integration time each. Blue dashed line fit to theory developed in [127].

between $APD_s$ and $APD_{s'}$. We generate a histogram of the number of coincidences between $APD_s$ and $APD_{s'}$ per number of herald events detected in the delay between these coincidences. The result for data collected at 3 $mW$ of pump power is shown in Figure 5.8.

We measure $g^{(2)}_{s,s|i}(0)$ at various values of pump power to study the degradation in the single-photon character of the signal mode with increasing source brightness. In Equation 5.33, we take $\tau = 0$ and substitute the count-rates for the 3-fold coincidences, coincidences and singles with the following expressions

$$\begin{aligned}
\mathcal{N}^{(2)}_{s,s',i}(0) &= \sum_k \sum_{\Delta_2} \sum_{\Delta_1} n_s^{(k+\Delta_1)} n_{s'}^{(k+\Delta_2)} n_i^{(k)} \\
\mathcal{N}_{s,i}(0) &= \sum_k \sum_{\Delta_1} n_s^{(k+\Delta_1)} n_i^{(k)} \\
\mathcal{N}_{s',i}(0) &= \sum_k \sum_{\Delta_2} n_{s'}^{(k+\Delta_2)} n_i^{(k)} \\
\mathcal{N}_i &= \sum_k n_i^{(k)}
\end{aligned} \tag{5.34}$$

where $\Delta_1$ and $\Delta_2$ both range from $-T_{coinc}/2\,t_b$ to $T_{coinc}/2\,t_b$. We look for both 3-fold and double coincidences within a coincidence interval set by $T_{coin} = 200\,ns$. This value for $T_{coin}$ was chosen because 200 $ns$ is sufficiently greater than the two-photon correlation time $\tau_c$ which is 33(4) $ns$, so that outside the window $\Delta\,t_b \in$[-100 $ns$, 100 $ns$], the coincidence rate drops to the accidental coincidence rate. $N = T_i/t_b$ and $T_i = 600$ s for each value of pump power. The results are shown in Figure 5.9. The lowest measured value of $g^{(2)}_{s,s|i} = 0.025(4)$ which is over a 100 standard deviations below the classical threshold $g^{(2)}_{s,s|i} \geqslant 1$. The data are fit with equation 24 from [127], where the impact of imperfect noisy detectors on the outcome of correlation measurements is studied. From the fit we estimate the $g^{(2)}_{s,s|i}(0)$ at 5 $mW$ (a typical power to have sufficient brightness for cold-atom experiments) to be 0.08.

# 6

# AUTOHETERODYNE CHARACTERISATION

This chapter has been adapted from the following publication [128].

## 6.1 QUANTUM INTERFERENCE WITH PHOTONS: A BRIEF BACKGROUND

At the outset of the thesis, we highlighted the fundamentally quantum nature of the light produced by SPDC. The very first proofs of this appeared in the 1980s through demonstrations of quantum interference effects, i.e., interference effects that could not be explained with the classical theory of light, using SPDC photons. These demonstrations followed predictions of such interference effects with markedly different signatures depending on whether the light used is a coherent state or a Fock state [93, 129]. The very first such quantum interference effect demonstrated was the Ghosh-Mandel (GM) effect [94]. The GM experiment utilised photons from SPDC that were produced with equal frequency and polarisation, but with photons in a pair having different momenta, to observe spatial interference of the two photons emitted by the source. One week after the publication of the GM article, a second nonclassical interference effect was reported, called the Hong-Ou-Mandel (HOM) effect [1], this time bringing signal and idler to different inputs of a beamsplitter, and observing from which outputs the photons emerged. Both the GM and HOM effects can be illustrated with single-mode calculations.

### 6.1.1 The Ghosh-Mandel effect

In the GM effect, two photons impinge on the detection region from different directions. The effect manifests as a position-dependent variation in the coincidences detected. To calculate this we need to consider both position and time dependence of the quantised

optical electric field in free space. We have neglected the first of these so far in this thesis. The positive frequency part of the position dependent quantised optical electric field is,

$$\hat{E}^{(+)}(\mathbf{x},t) = \sum_{\mathbf{k}} i\sqrt{\frac{\hbar\omega_k}{2\epsilon_0 V}}\hat{a}_k e^{i(\mathbf{k}\cdot\mathbf{x}-\omega_k t)} \tag{6.1}$$

where $V$ is the quantisation volume, $\hbar$ is Planck's constant and $\epsilon_0$ is the permittivity of free space. The factor $i\sqrt{\frac{\hbar\omega_k}{2\epsilon_0 V}}$ is slowly varying over the frequencies produced by SPDC, so we treat it as a constant.

We consider the two-photon Fock state from SPDC, $|\psi\rangle = \hat{a}_p^\dagger \hat{a}_q^\dagger |0\rangle$, where $\hat{a}_p$ and $\hat{a}_q$ are annihilation operators for modes with photon wave-vector $\mathbf{p}$ and $\mathbf{q}$, respectively and at frequencies $\omega_p$ and $\omega_q$ respectively. The two photons are made incident on a screen along the $\mathbf{x}$ direction. The probability density for detecting singles at a position $\mathbf{x}_1$ on the screen is proportional to the first order correlation function

$$\begin{aligned} G^{(1)}(\mathbf{x}_1,t) &= \langle\psi|\hat{E}^{(-)}(\mathbf{x}_1,t)\hat{E}^{(+)}(\mathbf{x}_1,t)|\psi\rangle \\ &\propto \langle 0|\hat{a}_p\hat{a}_q\left[\hat{a}_p^\dagger e^{-i(\mathbf{p}\cdot\mathbf{x}_1-\omega_p t)} + \hat{a}_q^\dagger e^{-i(\mathbf{q}\cdot\mathbf{x}_1-\omega_q t)}\right] \\ &\quad \times\left[\hat{a}_p e^{i(\mathbf{p}\cdot\mathbf{x}_1-\omega_p t)} + \hat{a}_q e^{i(\mathbf{q}\cdot\mathbf{x}_1-\omega_q t)}\right]\hat{a}_p^\dagger\hat{a}_q^\dagger|0\rangle \\ &= 2 \end{aligned} \tag{6.2}$$

Thus the average rate of singles detected on the screen is the same at all positions and shows no patterns.

The probability density for coincidences detected at positions $\mathbf{x}_1$ and $\mathbf{x}_2$ at times $t_1$ and $t_2$ respectively, is proportional to $G^{(2)}(\mathbf{x}_1,t_1,\mathbf{x}_2,t_2)$

$$\begin{aligned} G^{(2)}(\mathbf{x}_1,t_1,\mathbf{x}_2,t_2) &= \langle\psi|\hat{E}^{(-)}(\mathbf{x}_1,t_1)\hat{E}^{(-)}(\mathbf{x}_2,t_2) \\ &\quad\times\hat{E}^{(+)}(\mathbf{x}_2,t_2)\hat{E}^{(+)}(\mathbf{x}_1,t_1)|\psi\rangle\,. \end{aligned} \tag{6.3}$$

Here, the only terms that contribute a nonzero value to the expectation over the input state $|\psi\rangle$ are

$$\begin{aligned}
\left\langle \hat{a}_p^\dagger \hat{a}_q^\dagger \hat{a}_p \hat{a}_q \right\rangle &= 1, \\
\left\langle \hat{a}_q^\dagger \hat{a}_p^\dagger \hat{a}_q \hat{a}_p \right\rangle &= 1, \\
\left\langle \hat{a}_p^\dagger e^{-i(\mathbf{p}\cdot\mathbf{x}_1 - \omega_p t_1)} \hat{a}_q^\dagger e^{-i(\mathbf{q}\cdot\mathbf{x}_2 - \omega_q t_2)} \right. & \\
\left. \times \hat{a}_q e^{i(\mathbf{q}\cdot\mathbf{x}_1 - \omega_q t_1)} \hat{a}_p e^{i(\mathbf{p}\cdot\mathbf{x}_2 - \omega_p t_2)} \right\rangle &= e^{i(\mathbf{q}-\mathbf{p})\cdot(\mathbf{x}_1 - \mathbf{x}_2)} e^{-i(\omega_q - \omega_p)(t_1 - t_2)}, \\
\left\langle \hat{a}_q^\dagger e^{-i(\mathbf{q}\cdot\mathbf{x}_1 - \omega_q t_1)} \hat{a}_p^\dagger e^{-i(\mathbf{p}\cdot\mathbf{x}_2 - \omega_p t_2)} \right. & \\
\left. \times \hat{a}_p e^{i(\mathbf{p}\cdot\mathbf{x}_1 - \omega_p t_1)} \hat{a}_q e^{i(\mathbf{q}\cdot\mathbf{x}_2 - \omega_q t_2)} \right\rangle &= e^{-i(\mathbf{q}-\mathbf{p})\cdot(\mathbf{x}_1 - \mathbf{x}_2)} e^{+i(\omega_q - \omega_p)(t_1 - t_2)}.
\end{aligned} \tag{6.4}$$

The time dependence of the $G^{(2)}$ vanishes if either $t_1 = t_2$ or if $\omega_p = \omega_q$. Under these conditions, summing the contributions from the terms in Equation 6.5 we get,

$$G^{(2)}(\mathbf{x}_1, \mathbf{x}_2, ) \propto 2 + 2\cos\left[(\mathbf{q}-\mathbf{p})\cdot(\mathbf{x}_1 - \mathbf{x}_2)\right]. \tag{6.5}$$

which shows the remarkable feature that, while detection of a photon at any location is possible, once one photon is detected at $\mathbf{x}_1$, there are locations where it is impossible to find the other photon. It was also proven in the 1987 GM article [94] that this behaviour cannot be reproduced with the semiclassical theory of light, in which classical waves excite detectors described quantum mechanically to produce discrete detection events.

### 6.1.2 Hong-Ou-Mandel effect

The HOM effect, which is a much better known quantum interference effect, finds plenty of application in quantum technologies such as quantum computing [130], communication [131] and sensing [5, 132]. The effect is seen when identical single photons are simultaneously incident on a beamsplitter, one on each input face, and coincidences measured between the output ports. To calculate this, we consider the state $|\psi\rangle = \hat{a}_u^\dagger \hat{a}_v^\dagger |0\rangle$ where each photon is incident on one face of a 50:50 beamsplitter (the spatial mode indicated with subscripts $u$ and $v$ respectively). Due to the beamsplitter, creation operators in the input modes $u, v$ of the beamsplitter are related to creation operators in the output modes $m, n$ according to,

$$\hat{a}_{u/v}^\dagger = \frac{1}{\sqrt{2}} \left( \hat{a}_m^\dagger \pm \hat{a}_n^\dagger \right). \tag{6.6}$$

Thus, the state $|\psi\rangle$ in terms of modes $m, n$ after the beamsplitter is,

$$\begin{aligned}\hat{a}_u^\dagger \hat{a}_v^\dagger |0\rangle &= \frac{1}{2}\left(\hat{a}_m^\dagger + \hat{a}_n^\dagger\right)\left(\hat{a}_m^\dagger - \hat{a}_n^\dagger\right)|0\rangle \\ &= \frac{1}{2}(\hat{a}_m^\dagger \hat{a}_m^\dagger - \hat{a}_m^\dagger \hat{a}_n^\dagger + \hat{a}_n^\dagger \hat{a}_m^\dagger - \hat{a}_n^\dagger \hat{a}_n^\dagger)|0\rangle\,. \end{aligned} \tag{6.7}$$

The effect is observed in detectors that are in fixed positions and so is not dependent on the position of the optical electric field. Hence, we go back to neglecting the position dependence of the quantised electric field and use $\hat{E}_\kappa^{(+)}(t) \propto \int d\omega\ \ \hat{a}_\kappa(\omega) e^{-i\omega t}$. The rate of coincidences detected between the output ports of the beamsplitter at zero delay between detections is proportional to the $G^{(2)}$ computed with the state given in Equation 6.7.

$$G_{m,n}^{(2)}(t, t+0) = \left\langle \hat{E}_m^{(-)}(t)\hat{E}_n^{(-)}(t)\hat{E}_n^{(+)}(t)\hat{E}_m^{(+)}(t)\right\rangle = 0. \tag{6.8}$$

Thus when identical photons are simultaneously incident in a BS, it is not possible to observe a coincidence in which one photon leaves by each output port and both photons get bunched to one output port of the beamsplitter.

## 6.2 OVERVIEW OF AUTOHETERODYNE CHARACTERISATION

In the introduction (chapter 1) of this thesis, we presented the importance of narrowband photons pairs with $\sim$ MHz bandwidths for applications in quantum information and for furthering our understanding of light-matter interactions. Such narrowband photon-pairs are not easily measured by passive frequency-domain techniques, because of the very high optical frequency resolution it would require. In such a two-photon Fock state, first-order interference vanishes, producing no observable beat-note. One alternative is stimulated parametric down-conversion [133], in which laser photons are used to seed the down-conversion and map the difference frequencies generated vs those suppressed [68, 134]. This technique has potential for use in tomography of the JSA [135], but requires an additional well-characterised laser source and careful matching of spatial modes.

Here we present a simpler and more efficient alternative, a time-domain characterisation of the two-photon state using nonclassical interference. The JSI is a two-dimensional function, while the Hong-Ou-Mandel (HOM) interference visibility is a scalar observable. Thus a characterisation of the JSI even along a single dimension requires many HOM

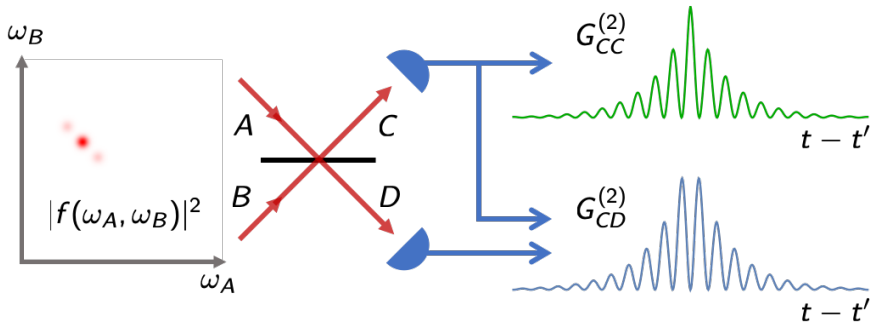


Figure 6.1: Principle of the method. Two photons, one in mode A and one in mode B, with joint spectral amplitude $f(\omega_A, \omega_B)$, illustrated in left graph ( color density indicates square magnitude), meet at a 50:50 BS and are detected in modes C and D. Single-photon-sensitive detectors register the photon arrival times. The correlation functions $G^{(2)}_{C,C}(t, t')$, $G^{(2)}_{D,D}(t, t')$ and $G^{(2)}_{C,D}(t, t')$ oscillate with $t - t'$, revealing the distribution $\omega_A - \omega_B$.

visibility measurements under changing experimental conditions, such as a changing path length [136, 137]. In contrast, the Ghosh and Mandel experiment [94] (GM), which measured the spatial interference pattern produced by photons of unequal momentum, showed how a correlation spectrum can be acquired with a single experimental condition. This motivates us to look for techniques that give more direct and more efficient access to the frequency correlations of interest. Our proposals for narrowband photon pair characterisation, are extensions of the HOM and GM interference effects.

The principle of the method is illustrated in Figure 6.1. Narrowband photon-pairs with the photons of each pair matched in polarisation and spatial profile but with unequal frequency, are injected, one into port A and the other into port B of a 50:50 beamsplitter (BS). Single-photon-sensitive detectors register photons leaving the BS by ports C and D, and time-tagging electronics record the arrival times. Many events are accumulated, and the second order correlation functions $G^{(2)}_{\kappa,\mu}(t, t')$, $\kappa, \mu \in \{C, D\}$ are calculated. Information about the JSA can then be inferred from the $G^{(2)}$ functions. We refer to this method as *autoheterodyne characterisation* (AHC), not to be confused with the single-photon self-heterodyne technique [138].

When photons of different frequency meet at a BS, their arrival-time distribution becomes modulated at the difference of their frequencies. This can be understood as follows: a detection at C and D with zero time delay, i.e. $t = t'$, can happen by two

channels in configuration space: either reflection of both photons or transmission of both photons. The amplitudes for these channels sum to zero, due to phase factors in the transmission and reflection processes. The resulting vanishing of $G^{(2)}_{C,D}(t,t)$ and the corresponding increase of $G^{(2)}_{C,C}(t,t)$ and $G^{(2)}_{D,D}(t,t)$ is the well-known HOM effect [1]. For unequal detection times, one must also consider the phase factors $\exp[-i\omega_A t - i\omega_B t']$ and $\exp[-i\omega_A t' - i\omega_B t]$ that apply to the two-reflection and two-transmission channels, respectively. The relative phase $(\omega_A - \omega_B)(t - t')$ between the channels then induces an oscillation of the $G^{(2)}$ correlations at the difference frequency $\omega_A - \omega_B$. We refer to this nonclassical interference between distinguishable photons as the nondegenerate HOM effect. Small frequency differences between the photons manifest as long-period oscillations in the relative arrival time distribution, which are technologically convenient to detect.

This technique implements a variant of the GM effect [94]. In GM, photon pairs with unequal transverse momenta $k_s, k_i$ are observed to produce a spatial autocorrelation function $G^{(2)}(x - x')$ that is maximum for $x - x' = 0$ and modulated with momentum $k_s - k_i$. The temporal modulation of $G^{(2)}_{C,C}$ or $G^{(2)}_{D,D}$, which describes the correlations of photon pairs with unequal frequencies $\omega_A, \omega_B$ in a single output channel, is the temporal analog of GM. We refer to this as the temporal Ghosh-Mandel effect. By conservation of probability at the BS, the GM and HOM signals must add to give $G^{(2)}_{A,B}(t,t')$, the signal-idler cross-correlation, as illustrated in Figure 6.1. As a result, the two methods give very similar information about the JSA.

## 6.3 THEORY OF AHC

### 6.3.1 Preliminaries and Definitions

The effect can be easily calculated. For a two-photon, two-mode state $|\psi\rangle$, written in the general form

$$|\psi\rangle = \int d\omega_s d\omega_i \, f(\omega_s, \omega_i) \hat{a}^\dagger_s(\omega_s) \hat{a}^\dagger_i(\omega_i) \, |0\rangle \,, \tag{6.9}$$

where $\omega_s$ and $\omega_i$ are, respectively, the signal and idler angular frequencies, $f(\omega_s, \omega_i)$ is the JSA, and $|f(\omega_s, \omega_i)|^2$ is the JSI. In the time-domain,

$$\tilde{f}(t_s, t_i) \propto \int d\omega_s d\omega_i f(\omega_s, \omega_i) e^{-i\omega_s t_s} e^{-i\omega_i t_i} \tag{6.10}$$

is the joint temporal amplitude (JTA) of the two-photon state.

In AHC, we introduce each mode of the two-photon state at one input face of a 50:50 beamsplitter (BS) and look for correlations at the BS outputs C, D of the form $G^{(2)}_{\kappa,\mu}(t,t') \equiv |\langle 0|\hat{E}^{(+)}_{\kappa}(t)\hat{E}^{(+)}_{\mu}(t')|\psi\rangle|^2$, $\kappa,\mu \in \{C,D\}$. Here the positive-frequency part of the fields at the detector are $\hat{E}^{(+)}_{\kappa}(t) \propto \int d\omega \hat{a}_{\kappa}(\omega)\exp[-i\omega t]$ and $\hat{a}_{\kappa}$, is an annihilation operator. Due to the BS, the output fields are related to the signal-idler fields (indicated with subscripts $s$ and $i$ respectively) according to $\hat{E}^{(+)}_{C/D}(t) = \frac{1}{\sqrt{2}}\left[\hat{E}^{(+)}_{s}(t) \pm \hat{E}^{(+)}_{i}(t)\right]$.

### 6.3.2 Exchange (anti)symmetries in AHC $G^{(2)}$

We now calculate the second-order correlations after the BS. The nondegenerate HOM effect and the temporal GM effect can be understood via exchange symmetries. Considering first the nondegenerate HOM signal, i.e. $G^{(2)}_{C,D}$, we find

$$\begin{aligned} G^{(2)}_{C,D}(t,t') &= \left|\langle 0|\,\hat{E}^{(+)}_{C}(t')\hat{E}^{(+)}_{D}(t)\,|\psi\rangle\right|^2 \\ &= \left|\int d\omega_s d\omega_i f(\omega_s,\omega_i)\langle 0|\frac{1}{2}\left[\hat{E}^{(+)}_{s}(t)+\hat{E}^{(+)}_{i}(t)\right]\right. \\ &\quad \left.\times\left[\hat{E}^{(+)}_{s}(t')-\hat{E}^{(+)}_{i}(t')\right]\hat{a}^{\dagger}_{s}(\omega_s)\hat{a}^{\dagger}_{i}(\omega_i)|0\rangle\right|^2. \end{aligned} \tag{6.11}$$

Here only the following 2 out of the 4 cross terms,

$$\langle 0|\left[-\hat{E}^{(+)}_{s}(t)\hat{E}^{(+)}_{i}(t')+\hat{E}^{(+)}_{i}(t)\hat{E}^{(+)}_{s}(t')\right]\hat{a}^{\dagger}_{s}(\omega_s)\hat{a}^{\dagger}_{i}(\omega_i)\,|0\rangle\,, \tag{6.12}$$

contribute to nonzero terms, to give

$$\begin{aligned} G^{(2)}_{C,D}(t,t') &\propto \left| \int d\omega_s d\omega_i f(\omega_s,\omega_i) \frac{1}{2} \langle 0| \left[ \int d\omega_i' \, e^{-i\omega_i' t} \hat{a}_i(\omega_i') \right. \right. \\ &\quad \times \int d\omega_s' \, e^{-i\omega_s' t'} \hat{a}_s(\omega_s') - \int d\omega_s' \, e^{-i\omega_s' t} \hat{a}_s(\omega_s') \\ &\quad \left. \left. \times \int d\omega_i' \, e^{-i\omega_i' t'} \hat{a}_i(\omega_i') \right] \hat{a}_s^\dagger(\omega_s) \hat{a}_i(\omega_i) |0\rangle \right|^2 \\ &\propto \left| \int d\omega_s d\omega_i f(\omega_s,\omega_i) \frac{1}{2} \left[ e^{-i(\omega_i t + \omega_s t')} - e^{-i(\omega_s t + \omega_i t')} \right] \right|^2 \quad (6.13) \\ &= \left| \frac{1}{2} [\tilde{f}(t',t) - \tilde{f}(t,t')] \right|^2 \\ &\equiv \left| \tilde{f}_A(t,t') \right|^2, \quad (6.14) \end{aligned}$$

where $\tilde{f}_A(t,t') \equiv \frac{1}{2}[\tilde{f}(t',t) - \tilde{f}(t,t')]$ is the exchange-antisymmetric part of the JTA.

We note that $G^{(2)}_{C,D}(t,t')$ can also be expressed directly in terms of the exchange-antisymmetric part of the JSA, as follows:

$$\begin{aligned} G^{(2)}_{C,D}(t,t') &\propto \left| \int d\omega_s d\omega_i f(\omega_s,\omega_i) \frac{1}{2} \left[ e^{-i(\omega_s t' + \omega_i t)} - e^{-i(\omega_s t + \omega_i t')} \right] \right|^2 \\ &= \left| \int d\omega_s d\omega_i e^{-i\omega_i t} e^{-i\omega_s t'} \frac{1}{2} f(\omega_s,\omega_i) \right. \\ &\quad \left. - \int d\omega_s d\omega_i e^{-i\omega_s t} e^{-i\omega_i t'} \frac{1}{2} f(\omega_s,\omega_i) \right|^2 \\ &= \left| \int d\omega' d\omega e^{-i\omega t} e^{-i\omega' t'} \frac{1}{2} f(\omega',\omega) \right. \\ &\quad \left. - \int d\omega d\omega' e^{-i\omega t} e^{-i\omega' t'} \frac{1}{2} f(\omega,\omega') \right|^2 \\ &= \left| \int d\omega d\omega' e^{-i\omega t} e^{-i\omega' t'} \frac{1}{2} \left[ f(\omega',\omega) - f(\omega,\omega') \right] \right|^2 \\ &\equiv \left| \int d\omega d\omega' e^{-i\omega t} e^{-i\omega' t'} f_A(\omega,\omega') \right|^2, \quad (6.15) \end{aligned}$$

where $f_A(\omega,\omega') \equiv \frac{1}{2}[f(\omega',\omega) - f(\omega,\omega')]$ is the exchange-antisymmetric part of the JSA. From Equation 6.14 and Equation 6.15, we see that $G^{(2)}_{C,D}(t,t')$ is the square magnitude of the antisymmetric part of the JTA, or equivalently the 2-D Fourier transform of the antisymmetric part of JSA.

In the same way, the temporal GM signals, i.e. $G^{(2)}_{C,C}$ and $G^{(2)}_{D,D}$, are related to the exchange-symmetric part of the JSA.

$$G^{(2)}_{\kappa,\kappa}(t,t') = \left| \int d\omega_s d\omega_i f(\omega_s,\omega_i) \times \frac{1}{\sqrt{2}} \langle 0|\hat{E}^{(+)}_\kappa(t)\hat{E}^{(+)}_\kappa(t')\hat{a}^\dagger_s(\omega_s)\hat{a}^\dagger_i(\omega_i)|0\rangle \right|^2 \tag{6.16}$$

where $\kappa \in \{C, D\}$. The factor $\frac{1}{\sqrt{2}}$, which does not appear in Equation 6.12, is introduced to correctly predict the number of two-photon events detected when both photons leave the beamsplitter by the same output. This is related to the normalisation of the two-photon state $\langle 0|\,\hat{E}^{(+)}_\kappa(t)\hat{E}^{(+)}_\kappa(t') \propto \langle 0|\,\hat{a}_\kappa\hat{a}_\kappa = \sqrt{2}\,\langle 2|$.

$$\begin{aligned} G^{(2)}_{\kappa,\kappa}(t,t') &= \left| \int d\omega_s d\omega_i f(\omega_s,\omega_i) \frac{1}{2\sqrt{2}} \langle 0| \left[\hat{E}^{(+)}_s(t) + \hat{E}^{(+)}_i(t)\right] \right. \\ &\quad \left. \times \left[\hat{E}^{(+)}_s(t') + \hat{E}^{(+)}_i(t')\right] \hat{a}^\dagger_s(\omega_s)\hat{a}^\dagger_i(\omega_i)|0\rangle \right|^2 \\ &\propto \left| \int d\omega_s d\omega_i f(\omega_s,\omega_i) \right. \\ &\quad \left. \times \frac{1}{2\sqrt{2}} \left[e^{-i(\omega_s t+\omega_i t')} + e^{-i(\omega_s t'+\omega_i t)}\right] \right|^2 \qquad (6.17) \\ &= \frac{1}{2}\left|\frac{1}{2}\left[\tilde{f}(t,t') + \tilde{f}(t',t)\right]\right|^2 \\ &\equiv \frac{1}{2}\left|\tilde{f}_S(t,t')\right|^2, \qquad (6.18) \end{aligned}$$

where $\tilde{f}_S(t,t') \equiv \frac{1}{2}[\tilde{f}(t,t') + \tilde{f}(t',t)]$ is the exchange-symmetric part of the JTA. Also $G^{(2)}_{C,C}(t,t') = G^{(2)}_{D,D}(t,t') \propto \frac{1}{2}\left|\int d\omega d\omega' e^{-i\omega t}e^{-i\omega' t'} f_S(\omega,\omega')\right|^2$ and $f_S(\omega,\omega') \equiv \frac{1}{2}\left[f(\omega,\omega') + f(\omega',\omega)\right]$, in analogy to Equation 6.15.

### 6.3.3 Sum and difference co-ordinates

It is convenient to work in the sum and difference co-ordinates $\omega_\pm \equiv \omega_s \pm \omega_i$ and $t_\pm \equiv t \pm t'$ to better visualise the results. The JSA in these co-ordinates can be written as

$$\mathring{f}(\omega_+,\omega_-) \equiv f\left(\frac{\omega_+ + \omega_-}{2}, \frac{\omega_+ - \omega_-}{2}\right). \tag{6.19}$$

Applying this transformation of co-ordinates to Equation 6.13 for the nondegenerate HOM effect,

$$\begin{aligned} \mathring{G}^{(2)}_{C,D}(t_+,t_-) &\propto \left|\frac{1}{2}\int d\omega_+ d\omega_- \mathring{f}(\omega_+,\omega_-) \right. \\ &\left. \times\frac{1}{2}\left[e^{-\frac{i}{2}(\omega_+ t_+ - \omega_- t_-)} - e^{-\frac{i}{2}(\omega_+ t_+ + \omega_- t_-)}\right]\right|^2. \end{aligned} \tag{6.20}$$

This can be simplified to

$$\mathring{G}^{(2)}_{C,D}(t_+,t_-) \propto \left|\frac{1}{2}\int d\omega_+ d\omega_- \mathring{f}(\omega_+,\omega_-) e^{-i\omega_+ t_+/2}\, i\sin(\omega_- t_-/2)\right|^2 \tag{6.21}$$

or equivalently to

$$\mathring{G}^{(2)}_{C,D}(t_+,t_-) \propto \left|\frac{1}{2}\int d\omega_+ d\omega_- e^{-i\omega_+ t_+/2} e^{-i\omega_- t_-/2}\, \mathring{f}_A(\omega_+,\omega_-)\right|^2, \tag{6.22}$$

where the antisymmetric part of parametrised JSA

$$\mathring{f}_A(\omega_+,\omega_-) = \frac{1}{2}\left[\mathring{f}(\omega_+,-\omega_-) - \mathring{f}(\omega_+,\omega_-)\right]. \tag{6.23}$$

Similarly for the GM effect introducing the transformation of co-ordinates to Equation 6.17 we get

$$\begin{aligned} \mathring{G}^{(2)}_{C,C}(t_+,t_-) &\propto \left|\frac{1}{2}\int d\omega_+ d\omega_- \mathring{f}(\omega_+,\omega_-) \right. \\ &\left. \times\frac{1}{2\sqrt{2}}\left[e^{-\frac{i}{2}(\omega_+ t_+ - \omega_- t_-)} + e^{-\frac{i}{2}(\omega_+ t_+ + \omega_- t_-)}\right]\right|^2 \end{aligned} \tag{6.24}$$

This can be simplified to

$$\mathring{G}^{(2)}_{C,C}(t_+,t_-) \propto \frac{1}{2}\left|\frac{1}{2}\int d\omega_+ d\omega_- \mathring{f}(\omega_+,\omega_-) e^{-i\omega_+ t_+/2}\cos(\omega_- t_-/2)\right|^2 \tag{6.25}$$

or equivalently to

$$\mathring{G}^{(2)}_{C,C}(t_+,t_-) \propto \frac{1}{2}\left|\frac{1}{2}\int d\omega_+ d\omega_- e^{-i\omega_+ t_+/2} e^{-i\omega_- t_-/2}\, \mathring{f}_S(\omega_+,\omega_-)\right|^2 \tag{6.26}$$

where the symmetric part of parametrised JSA is

$$\mathring{f}_S(\omega_+,\omega_-) = \frac{1}{2}\left[\mathring{f}(\omega_+,-\omega_-) + \mathring{f}(\omega_+,\omega_-)\right]. \tag{6.27}$$

***Discussion***

The AHC correlation results describe a Fourier transform of the JSA along the $\omega_\pm$ coordinates. When the two-photon state is produced by SPDC, and pumped by a broadband pump with field $E_p(t) = \int d\omega_p \alpha(\omega_p) e^{-i\omega_p t}$, we find that $f(\omega_+, \omega_-) \propto \int d\omega_p \alpha(\omega_p)\delta(\omega_p - \omega_+)g(\omega_-, \omega_+) \propto \alpha(\omega_+)g(\omega_-, \omega_+)$. When the variation of the crystal phase matching function over the pump-bandwidth can be neglected, $g$ becomes independent of $\omega_+$ and the JSA factorises as $f(\omega_+, \omega_-) \propto \alpha(\omega_+)g(\omega_-)$. The AHC $G^{(2)}$ then gives the sine or cosine power spectrum of $g(\omega_-)$ in the $t_-$ dimension and also gives the Fourier transformed spectrum of $\alpha(\omega_+)$ via the $t_+$ dimension. For a monochromatic pump $\alpha(\omega_+) \to \delta(\omega_+ - \omega_p)$, such that $f(\omega_+, \omega_-) \propto \delta(\omega_+ - \omega_p)g(\omega_-)$, so that $G^{(2)}$ depends only on $t_-$. In the following section we study the narrowband, cw-pump case. The use of AHC in the pulsed scenario and to obtain measures such as entanglement entropy, state purity and Schmidt number [113] is discussed in the last section.

## 6.4 MONOCHROMATIC PUMP SCENARIO

For a monochromatic narrowband pump of frequency $\omega_p$ the two-photon JSA can be written as,

$$\begin{aligned} f(\omega_s, \omega_i) &= \int d\omega_p' \delta(\omega_p - \omega_p')\delta(\omega_p' - \omega_s - \omega_i)g(\omega_s, \omega_i) \\ &= \delta(\omega_p - \omega_s - \omega_i)g(\omega_s, \omega_i), \end{aligned} \tag{6.28}$$

where $\int d\omega_p' \delta(\omega_p - \omega_p')$ describes the pump frequency distribution and $\delta(\omega_p' - \omega_s - \omega_i)$ is the energy conservation condition from SPDC. Transforming the JSA to the $\omega_\pm$ basis,

$$\mathring{f}(\omega_+, \omega_-) = \delta(\omega_p - \omega_+)g\left(\frac{\omega_+ + \omega_-}{2}, \frac{\omega_+ - \omega_-}{2}\right). \tag{6.29}$$

Applying this to Equation 6.21 or Equation 6.25, we see that the AHC $G^{(2)}$ reduces to a function of a single variable $t_-$. We now proceed to model the AHC output for our specific case of the output from a filtered CE-SPDC system.

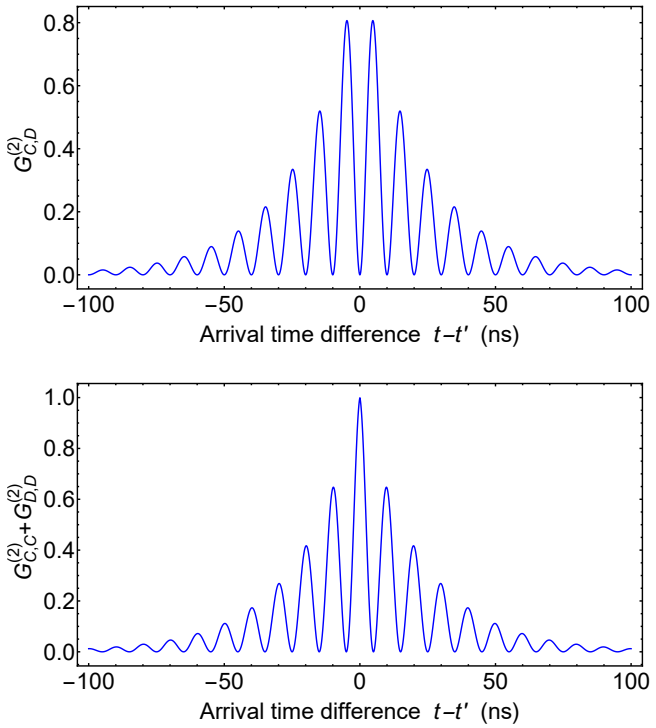


Figure 6.2: Simulated AHC measurements for narrowband pump, signal-idler beat-note of 100 MHz and signal-idler linewidth of $2\pi \times 7$ MHz. Top: Normalised nondegenerate HOM results. Bottom: Normalised temporal GM results. Simulations show oscillations with a 10 ns period, offset by 180° with a double exponential envelop decaying in accordance with the linewidth.

### 6.4.1 Modelling AHC results for perfect filter functionality

We consider the JSA when the filters select signal-idler frequency modes from the CE-SPDC output of central frequency $\omega_s^0$ and $\omega_i^0$ respectively and perfectly extinguish all other frequency components from the CE-SPDC. We call this "perfect filtering". In this scenario the two-photon JSA consists of a single Lorentzian line each for the signal and idler and can be given as in Equation 3.8 as,

$$f(\omega_s, \omega_i) = \xi\, \delta(\omega_p - \omega_s - \omega_i) \prod_{\nu \in \{s,i\}} \frac{\gamma_\nu/2}{\gamma_\nu/2 + i\,(\omega_\nu^0 - \omega_\nu)}, \tag{6.30}$$

for some constant $\xi$. We consider the case when $\gamma_s = \gamma_i = \gamma$. Performing a co-ordinate transformation to the $\omega_\pm$ basis,

$$\begin{aligned}
\mathring{f}(\omega_+, \omega_-) &= \xi\, \delta(\omega_p - \omega_+) \frac{\gamma/2}{\gamma/2 + i\,\left(\omega_s^0 - \frac{\omega_+ + \omega_-}{2}\right)} \frac{\gamma/2}{\gamma/2 + i\,\left(\omega_i^0 - \frac{\omega_+ - \omega_-}{2}\right)} \\
&= \xi\gamma\, \delta(\omega_p - \omega_+) \frac{1}{\gamma^2 + (\omega_s^0 - \omega_i^0 - \omega_-)^2} \\
&\equiv \delta(\omega_p - \omega_+) g(\omega_-), \qquad (6.31)
\end{aligned}$$

noting that $\omega_s^0 + \omega_i^0 = \omega_+$.

Thus the JSA and $G^{(2)}$ signals can be reduced to a function of a single coordinate. The symmetric (antisymmetric) JSA in the sum/difference coordinates is

$$\mathring{f}_{S/A}(\omega_+, \omega_-) = \delta(\omega_+ - \omega_p) \frac{1}{2} \left[ g(-\omega_-) \pm g(\omega_-) \right], \qquad (6.32)$$

at which point the integral over $d\omega_+$ that appears in Equation 6.22 and Equation 6.26 can be performed trivially. $\mathring{G}^{(2)}_{C,C/D}(t_+, t_-)$ is seen to be independent of $t_+$,

$$\begin{aligned}
\mathring{G}^{(2)}_{C,D}(t_-) &\propto \left| \int d\omega_- e^{-i\omega_- t_-/2} \frac{1}{2} \left[ g(-\omega_-) - g(\omega_-) \right] \right|^2 \\
&\equiv |\tilde{g}_A(t_-)|^2 . \\
\mathring{G}^{(2)}_{C,C}(t_-) &\propto \frac{1}{2} \left| \int d\omega_- e^{-i\omega_- t_-/2} \frac{1}{2} \left[ g(-\omega_-) + g(\omega_-) \right] \right|^2 \\
&\equiv \frac{1}{2} |\tilde{g}_S(t_-)|^2 , \qquad (6.33)
\end{aligned}$$

where $\tilde{g}_S(t_-)$ is the exchange-symmetric part and $\tilde{g}_A(t_-)$ is the exchange-antisymmetric part of the JTA. We henceforth omit the $t_+$ argument when discussing this monochromatic pump scenario. Evaluating $\tilde{g}_{S/A}(t_-)$ and $\mathring{G}^{(2)}_{C,C/D}(t_-)$ for $g(\omega_-)$ from Equation 6.31 we get

$$\tilde{g}_{S/A}(t_-) \propto \xi \begin{matrix} \cos \\ i \sin \end{matrix} \left[ \left(\omega_s^0 - \omega_i^0\right) \frac{t_-}{2} \right] \times \begin{cases} e^{\frac{\gamma t_-}{2}} & t_- \leqslant 0 \\ e^{-\frac{\gamma t_-}{2}} & t_- > 0 \end{cases}, \qquad (6.34)$$

where cos is associated with $\tilde{g}_S(t_-)$ and sin with $\tilde{g}_A(t_-)$.

The exchange-(anti)symmetric part of the JTA is proportional to $\xi$, and so the $G^{(2)}$ in Equation 6.33 proportional to $\xi^2$. Note that the JSI also scaled as $\xi^2$. While $\tilde{g}_{S/A}(t_-)$

oscillates with a periodicity of $2 \times \left[\frac{1}{2\pi}\left(\omega_s^0 - \omega_i^0\right)\right]^{-1}$, $\mathring{G}^{(2)}_{C,D}(t_-)$ oscillates with a periodicity of $\left[\frac{1}{2\pi}\left(\omega_s^0 - \omega_i^0\right)\right]^{-1}$. The signals for the temporal Ghosh-Mandel effect ($G^{(2)}_{CC}$ or $G^{(2)}_{DD}$) are shifted in phase by $\pi$ from the nondegenerate HOM signal ($G^{(2)}_{CD}$). Due to conservation of photon number, $G^{(2)}_{CC} + G^{(2)}_{DD}$ and $G^{(2)}_{CD}$ must sum to give $G^{(2)}_{AB}$, the output of the SPDC cavity before HOM mixing on the beamsplitter. $G^{(2)}_{AB}$ does not exhibit a beat-note; it's spectrum is limited to the two-photon bandwidth. The oscillating components of $G^{(2)}_{CC} + G^{(2)}_{DD}$ and of $G^{(2)}_{CD}$ are thus equal and opposite as shown in Figure 6.2.

### 6.4.2 Power spectral density analysis

By looking at the power spectral density (PSD) of $\mathring{G}^{(2)}_{C,D}(t_+, t_-)$ $\left(\mathrm{PSD}\left[G^{(2)}\right]\right)$, we get information about the JSA and JSI. By definition, the two-dimensional PSD of $G^{(2)}_{C,D}(t, t')$ is proportional to the square magnitude of the Fourier transform of $G^{(2)}_{C,D}(t, t')$.

$$\mathrm{PSD}\left[G^{(2)}_{C,D}(t,t')\right](\omega,\omega') \propto \left|\int dt\, dt'\, e^{i(\omega t+\omega' t')} G^{(2)}_{C,D}(t,t')\right|^2. \quad (6.35)$$

This can also be represented in the sum and difference coordinates

$$\mathrm{PSD}\left[\mathring{G}^{(2)}_{C,D}(t_+,t_-)\right](\omega_+,\omega_-) \propto \left|\int dt_+\, dt_- \times e^{i(\omega_+ t_+ + \omega_- t_-)} \mathring{G}^{(2)}_{C,D}(t_+,t_-)\right|^2 \quad (6.36)$$

We now show how a spectral feature in the JSI translates to a spectral feature in $\mathrm{PSD}\left[\mathring{G}^{(2)}_{C,D}\right]$. For the two-photon state described in Equation 6.31, we note that if $g(\omega_-)$ has a peak at some frequency, e.g. $\omega_-^0 \equiv \omega_s^0 - \omega_i^0$, then $g(-\omega_-) - g(\omega_-)$, will have a peak at $-\omega_-^0$ and also at $\omega_-^0$. These give a beat-note in $\mathring{G}^{(2)}_{C,D}(t_-)$ at frequency $|\omega_i^0 - \omega_s^0|$. Note that the frequency doubling (beating of $\omega_-^0$ with $-\omega_-^0$, a result of (anti)symmetrisation) cancels the factor of $1/2$ due to the use of sum and difference coordinates. We thus see that peaks in $g(\omega_-)$ will be represented as peaks in the PSD of $\mathring{G}^{(2)}$ at the same frequencies.

To illustrate this, we simulate AHC resuts using Equation 6.34, and with the spectral parameters taken from our system, in Figure 6.3. Also shown is the JSI $|\mathring{f}(\omega_+ = 0, \omega_-)|^2$, which illustrates the fact that the line width in the JSI and in the PSD of

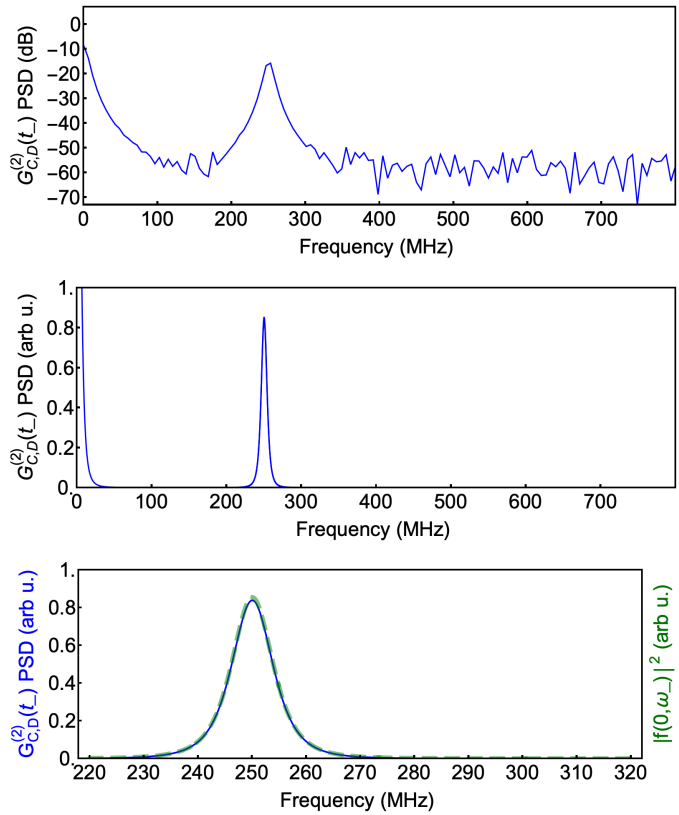


Figure 6.3: Simulated spectra using Equation 6.35, a signal-idler beat-note of 250 MHz and measured CE-SPDC cavity linewidths. Top: PSD of $G^{(2)}_{C,D}(t_-)$ in log scale, (as in the manuscript). A pseudo-random noise has been added to simulate the statistical noise of the $G^{(2)}_{C,D}$ acquisition. Middle: same as in the top graph, but on a linear scale. Bottom: close-up of the feature at 250 MHz (in blue), overlain with $|\mathring{f}(\omega_+ = 0, \omega_-)|^2$ (in dashed green), showing the agreement of linewidth and line shape.

$\mathring{G}^{(2)}_{C,D}(t_-)$ are the same. The width of the peak in the $G^{(2)}$ PSD is the spectral width, along the $\omega_-$ direction, of the two-photon JSI. This is evident from Equation 6.34, which shows that the oscillations in the AHC $G^{(2)}$, albeit in the $t_-$ dimension, decay exponentially according to the linewidth $\gamma$ of the CE-SPDC source.

We note that $G^{(2)}$, like the JSI, scales quadratically with f (the JSA), and thus that PSD$[G^{(2)}]$ scales as the fourth power of f. This nonlinear relationship between the JSI and PSD$[G^{(2)}]$ leads to a number of effects. First and most simply, if the the height of a

peak in the JSA is proportional to $\xi$ (Equation 6.31), the JSI scales as $|\xi|^2$ and PSD[$G^{(2)}$] scales as $|\xi|^4$, and is proportional to the square of the height of the corresponding peak in the JSI. Second, PSD[$G^{(2)}$] has many of the properties of a convolution (in suitable coordinates) of the JSI with itself. This, for example, explains the origin of the peak in PSD[$G^{(2)}$] around zero frequency. To continue with the example just described, if $|f_A(\omega_s, \omega_i)|^2$ has peaks at $\omega^0_-$ and $-\omega^0_-$, then the autoconvolution will (again taking into account the factor of $1/2$ from the change of coordinates) have peaks at zero, $\omega^0_-$ and $-\omega^0_-$, as seen in Figure 6.3.) A more complex JSI, e.g. with multiple difference-frequency peaks, would lead to cross-terms at frequencies that are sums and differences of the frequencies represented in the JSI.

### 6.4.3 Modelling AHC results for imperfect filter functionality

In the event that the designed FP filter cavities do not select exclusively a single pair of signal-idler frequency modes from the CE-SPDC, but instead allow other modes from a cluster to leak, there will be multiple frequency components in the two-photon state and the JSA can no longer be described by Equation 3.8. Since the AHC is sensitive to the difference frequencies in the two-photon state, it can be used for a quantitative measurement of the contamination with unwanted frequency content and thereby assess the performance of the FP filters. On the other hand, the AHC results can be simulated in advance to estimate the tolerances in filter parameters and this information can be used to then design a suitable filter. For this, a complete model for the JSA, taking into account repeating resonances for both signal and idler in both cavities (CE-SPDC and FP), can be used in combination with Equation 6.21. To demonstrate this we use the expression for the JSA from CE-SPDC after a filter each in the signal and idler arms given in Equation 3.4, where no simplifications have been made from assuming that the FP filters perfectly extinguish unwanted frequency modes from the CE-SPDC.

We consider the scenario when the FP filters are tuned to the preferred CE-SPDC output modes such that the filters' index frequencies coincide with those of the CE-SPDC cavity, i.e., $\omega^0_{f_\nu} = \omega^0_\nu$ for $\nu \in \{s, i\}$. Under these conditions, transforming the JSA in Equation 3.4 to the $\omega_\pm$ basis, and noting that the $G^{(2)}$ from AHC is only dependent on $t_-$ for a monochromatic pump as discussed previously, we numerically compute the $G^{(2)}$ and use it to calculate the PSD[$G^{(2)}$], for various values of FP linewidth $\gamma_f$. The summations were truncated to cover only the central cluster. Since contribution from

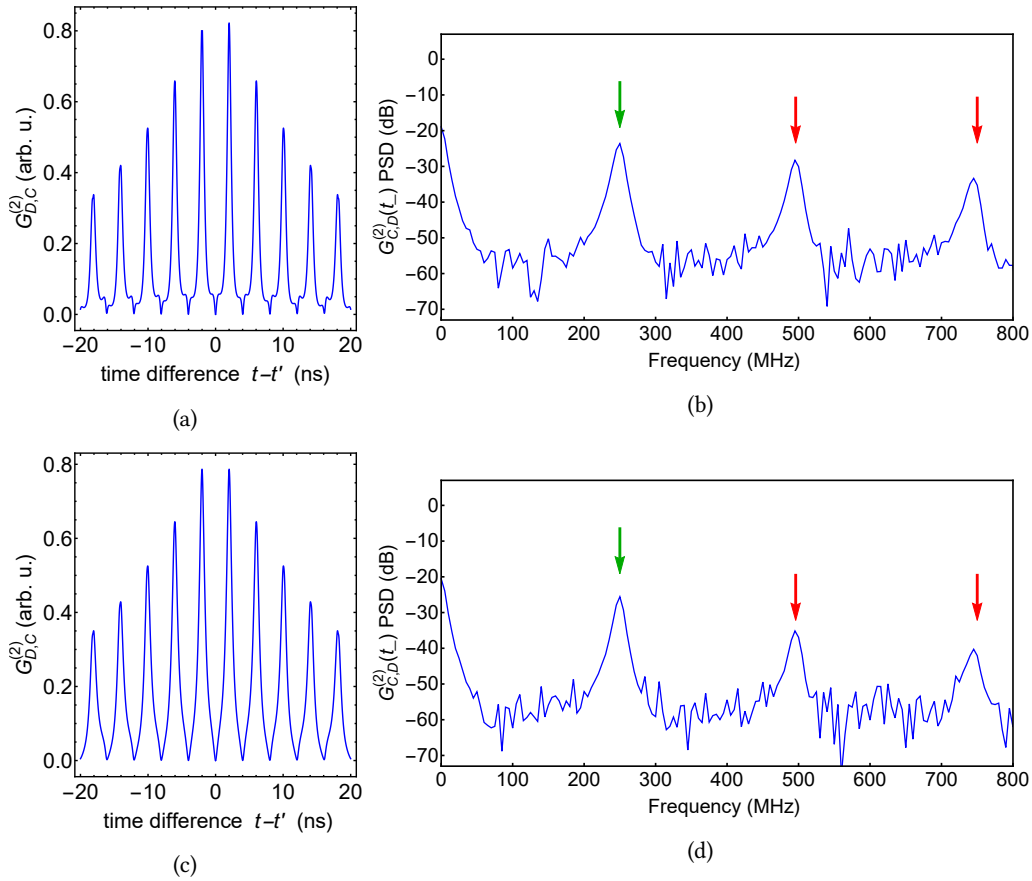


Figure 6.4: Simulated $G^{(2)}_{C,D}$ and PSD$[G^{(2)}_{C,D}]$ for various FP linewidths when $\omega^0_-$ is 250 MHz: (a) and (b): $G^{(2)}_{C,D}$ and PSD$[G^{(2)}_{C,D}]$ respectively for $\gamma_p = 2\pi \times 600$ MHz. (c) and (d): the same functions for $\gamma_p = 2\pi \times 400$ MHz. Note the distortion of the valleys in (a) and (c) relative to what is seen in Figure 6.2. The PSD results show a peak at $\omega^0_-/2\pi$ (green arrow) additional peaks (red arrows) at 496 MHz, due to leakage of adjacent CE-SPDC modes and 750 MHz, due to leakage of mode pairs with $|\omega_-|/2\pi = |250\,\text{MHz} - 2\text{FSR}|$. The amplitude of the unwanted peaks decreases with increasing FP finesse.

$f_{NB}(\omega_s, \omega_i)$, which has a spectral width of $\sim$ 100 GHz, does not change appreciably over the central cluster, which has a spectral width of $\sim$ 1 GHz, we treat $f_{NB}$ as a constant. Other cavity parameters were set to match experimentally measured values reported in subsection 2.2.2. Results are shown in Figure 6.4 and Figure 6.5 for a

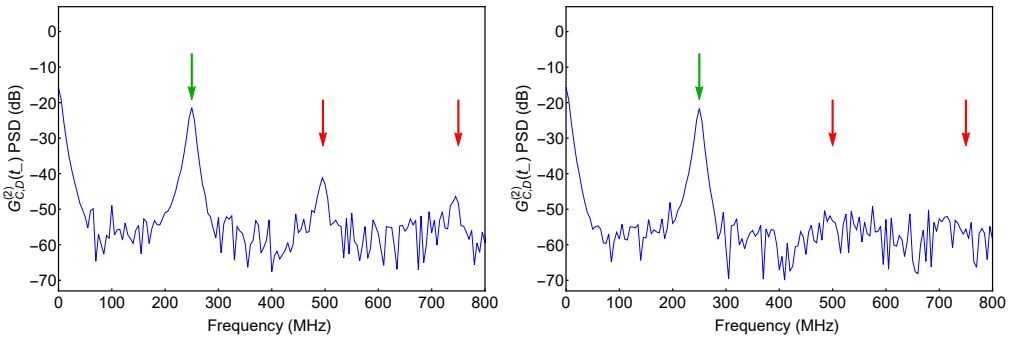


Figure 6.5: Simulated PSD[$G^{(2)}$] for various FP linewidths when $\omega^0_-$ is 250 MHz: (a) and (b): PSD[$G^{(2)}$] when $\gamma_f = 2\pi \times 200$ MHz and $\gamma_f = 2\pi \times 100$ MHz respectively. The contribution of unwanted frequencies (red arrows) drops to within the noise (30 dB below the main beat frequency) when the FP linewidth is 100 MHz.

frequency difference of $\omega^0_- = 250$ MHz between the central signal-idler modes $\omega^0_s$ and $\omega^0_i$ which the filters are tuned to maximally transmit. Figure 6.5b shows that, for a FP filter linewidth of 100 MHz, the unwanted modes are 30 dB below the main peak. For this FP linewidth, the PSD[$G^{(2)}$] results match Figure 6.3 obtained using the simplified model for the JSA in Equation 6.30 which assumes "perfect filtering". Since the FP filters we employ in our experiment have this bandwidth, we can conclude that the "perfect filtering" model in Equation 6.30, where the two-photon JSA comprises a single Lorentzian each for the signal and idler, well describes the actual JSA of the two-photon state from our CE-SPDC + filter system. In what follows, we experimentally verify this.

### 6.4.4 Experimental results

To perform AHC of the CE-SPDC source, the pump laser, cavity mode and FP mode frequencies are tuned to produce and pass a single signal-idler mode pair with a frequency difference $\omega^0_- = \omega^0_s - \omega^0_i$. The measurement is performed for two values of $\omega^0_-/(2\pi)$, 250 MHz and 165 MHz. Single-mode fibers and linear polarisers ensure good spatial and polarisation matching when the signal and idler photons arrive at the BS via spatial modes A and B, respectively. BS output modes C and D are coupled into

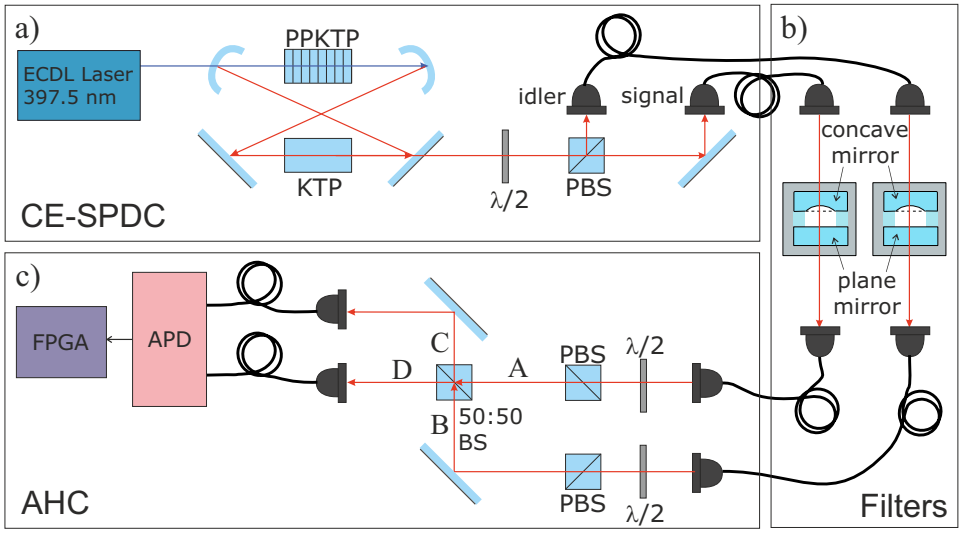


Figure 6.6: Schematic of setup for generation and characterisation of narrowband photon-pairs. (a) CE-SPDC source, consisting of a bow-tie cavity containing an ECDL-pumped SPDC crystal (PPKTP) and a second crystal (KTP). Photon pairs are separated by polarisation. (b) Tuneable FP filters are used to select desired "teeth" from the comb of CE-SPDC output modes. (c) Autoheterodyne characterisation. The photons are set to the same polarisation, interfered on a beam splitter (BS), detected using avalanche photodiodes (APDs) and time-tagged with an FPGA. KTP - potassium titanyl phosphate crystal; PPKTP - periodically-poled KTP crystal; PBS - polarising beam splitter; $\lambda/2$ - half-wave plate; FPGA - field programmable gate array.

single mode fibers leading to APDs. An FPGA with a resolution of 625 ps (sampling rate 1.6 GHz) is used to time-stamp the APD detections. The experimental set-up is shown schematically in Figure 6.6

Figure 6.7 shows the observed and predicted $G^{(2)}_{C,D}$ for a frequency difference of $\omega^0_- = 250$ MHz between the signal and idler modes. In accordance with the theory, the results show a clear oscillation with period 4 ns, the inverse of 250 MHz. The visibility of the interference is 82%, which is greater than the classical limit of 50% [94], attests to the fact that the interference was produced by nonclassical states. The predicted $G^{(2)}_{C,D}$, calculated with $\gamma = 2\pi \times 7.6$ MHz, agrees with the observed fringe period and also with the decay rate of the exponential envelope. This implies a FWHM bandwidth of $\gamma\sqrt{\sqrt{2}-1} = 2\pi \times 4.9$ MHz for signal, idler, and difference frequency [139]. The

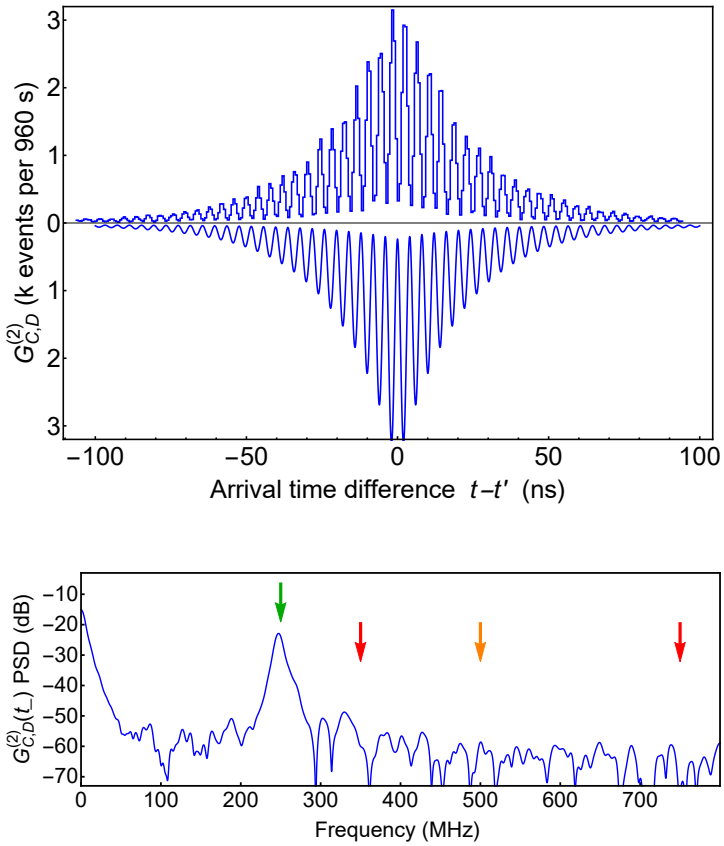


Figure 6.7: Observed and predicted $G^{(2)}_{C,D}$ cross-correlation and spectral analysis. Top: (upper curve) Histogram of recorded arrival time differences with 625 ps time bins, for $\omega^0_- = 2\pi \times 250\,\mathrm{MHz}$ . (lower curve) Predicted $G^{(2)}_{C,D}$ with factors chosen manually such that the amplitude and visibility match the experimental results. Bottom: Power spectral density (PSD) of $G^{(2)}_{C,D}(t_-)$ computed from observed histogram for $\omega^0_- = 2\pi \times 250\,\mathrm{MHz}$ . The beat-note is clearly seen at 250 MHz. Locations at which spectral contamination might be expected are indicated with red and orange arrows. The contamination is at least 25 dB below the power level of the desired beat-note.

AHC measurement was repeated for a signal-idler frequency difference of 165 MHz, and thus an oscillation period $\approx 6$ ns in the $G^{(2)}_{C,D}$ was observed Figure 6.8.

The power spectra of the observed $G^{(2)}_{C,D}$ for $\omega^0_-/2\pi$ of 250 MHz and 165 MHz are shown in Figure 6.7 and 6.8 respectively. Each shows a peak at dc and a Lorentzian peak

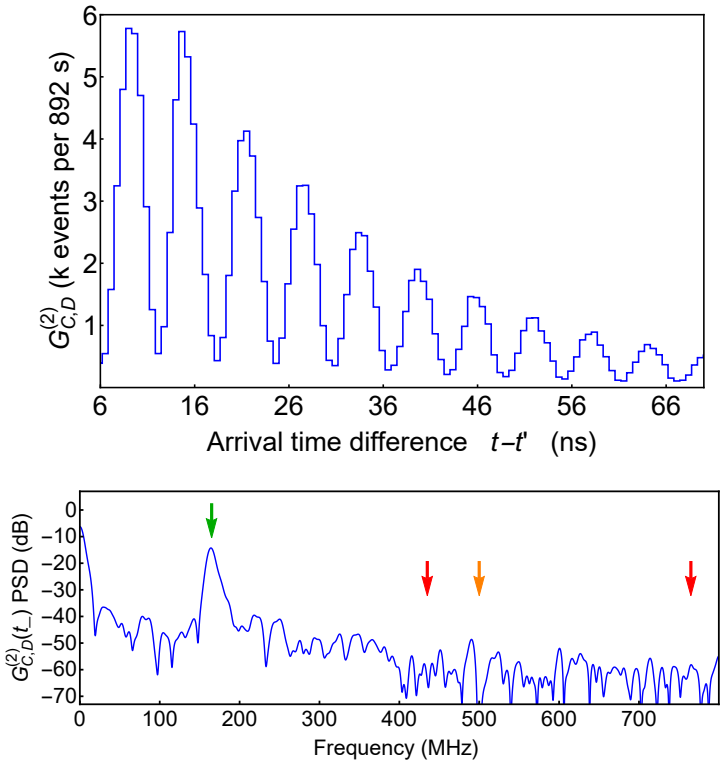


Figure 6.8: Observed $G^{(2)}_{C,D}$ cross-correlation and spectral analysis for $\omega^0_- = 2\pi \times 165\,\mathrm{MHz}$ . Top: Histogram of recorded arrival time differences with 625 ps time bins, zoomed-in to show oscillations at 6 ns. Bottom: Power spectral density (PSD) of $G^{(2)}_{C,D}(t_-)$ computed from observed histogram . The beat-note is clearly seen at 165 MHz. Locations at which spectral contamination might be expected are indicated with red and orange arrows. The contamination is at least 25 dB below the power level of the desired beat-note.

at the corresponding $\omega^0_-$, of the same width and center frequency as the Lorentzian in the JSI computed from Equation 6.38. The resolution of these spectra is inversely proportional to the range of $t - t'$, which can extend to the full acquisition time. In practice, the resolution is much finer than any spectral feature.

Inefficient extinction of neighbouring CE-SPDC modes by the FP filter would manifest as additional signals in the PSD besides one at the expected $\omega^0_-$. In Figure 6.7, peaks at 750 MHz and/or 350 MHz (aliased down from 1250 MHz due to the sampling rate of the FPGA) would indicate leakage of mode pairs with $\omega_-/2\pi = 250\,\mathrm{MHz} \pm 2\,\mathrm{FSR}$

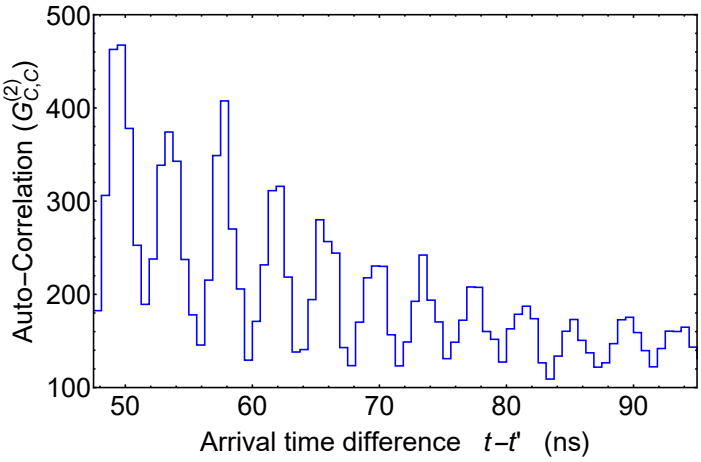


Figure 6.9: Temporal GM effect. Graph shows the un-normalised autocorrelation detected in detector C ($G^{(2)}_{C,C}$) after the BS. The oscillations corresponding to the inverse frequency difference for $\omega^0_- = 2\pi \times 250\,\mathrm{MHz}$.

(red arrows). A peak at 500 MHz (the FSR for both signal and idler) might also be expected, but is not seen (orange arrow). Similarly, leakage would produce peaks at 765 MHz and 435 MHz (red arrows), and again 500 MHz (orange arrow) in Figure 6.8. We thus conclude that the FP cavity filtering succeeds in blocking contributions from neighbouring CE-SPDC modes and that the combined CE-SPDC and filter system emits on one pair of CE-SPDC cavity modes.

Measurement of $G^{(2)}_{C,C}$, showing the temporal GM effect, is shown in Figure 6.9 for $\omega^0_- = 2\pi \times 250\,\mathrm{MHz}$. Typically SPDC $G^{(2)}$ autocorrelations require a BS and two detectors, in order to record photon pairs that arrive spaced by less than a detector's dead time, here $\approx 40\,\mathrm{ns}$. For narrowband photon-pairs, however, it is possible to acquire the autocorrelation with just one detector, as we do here. The predicted oscillation with a period of 4 ns is clearly observed. The temporal GM effect thus offers a simple way to characterize relative frequencies with a single detector. Frequency shifting of one input photon through nonlinear frequency conversion [140], would allow AHC to measure spectra with difference frequencies outside the the detection electronics' bandwidth.

***Comment: Spectral resolution and range of AHC***

Spectral characterisation by the AHC technique is based on time-correlated photon counting, not on optical frequency discrimination, e.g. using a monochromator. For this reason, its spectral resolution is not limited by the resolution of any optical instrument. It is, rather, limited by frequency resolution of the electronic systems used to record the photon detections. For the experiment reported here, this limit would be set by the frequency instability of the electronic clock used in the time-tagging module, and ultimately by the duration of the acquisition. In practice, these resolution limits allow measurement of the finest spectral features of any practical SPDC source and contribute negligible broadening to the inferred spectra, e.g. those shown in Figure 6.7

The spectral range of the AHC technique is limited by the time resolution (or jitter) of the detectors and time-tagging electronics. Although not the case for our equipment, this time resolution can be in the few-picosecond regime with modern detectors and electronics, giving a $\sim$ 100 GHz beat-note bandwidth for the technique [141]. If the frequency difference to be investigated is larger than this, nonlinear optical frequency conversion could be used to shift the frequency of one photon while preserving its nonclassical features [140], and thereby bring the beat-note and sidebands within the range of the technique.

## 6.5 BROADBAND PUMP AND PURE-STATE CHARACTERISATION

One major motivation for studying two-photon states is their potential use as heralded single photon states or in quantum networking, in which photons from different sources are interfered for purposes such as entanglement swapping. These applications typically require two-photon states which are approximately a product of two pure single photon states [28]. In such states, the frequency entanglement between the down-converted photons is small. When one photon from such a pair is detected, the resulting state – mathematically described by a partial trace over the original state – shows the partner photon to be in a pure or nearly-pure state.

The extent of spectral entanglement between the photons in a two-photon state can be quantified through Schmidt decomposition of the JSA [79, 113, 142]. For this, the JSA of the composite state is expressed in terms of two sets of independent orthonormal functions $\{S_n(\omega_s)\}$ and $\{I_n(\omega_i)\}$ for the signal and idler, respectively, such that $f(\omega_s, \omega_i) = \sum_n \sqrt{\lambda_n} S_n(\omega_s) I_n(\omega_i)$. Here $\lambda_n$ are called Schmidt coefficients or

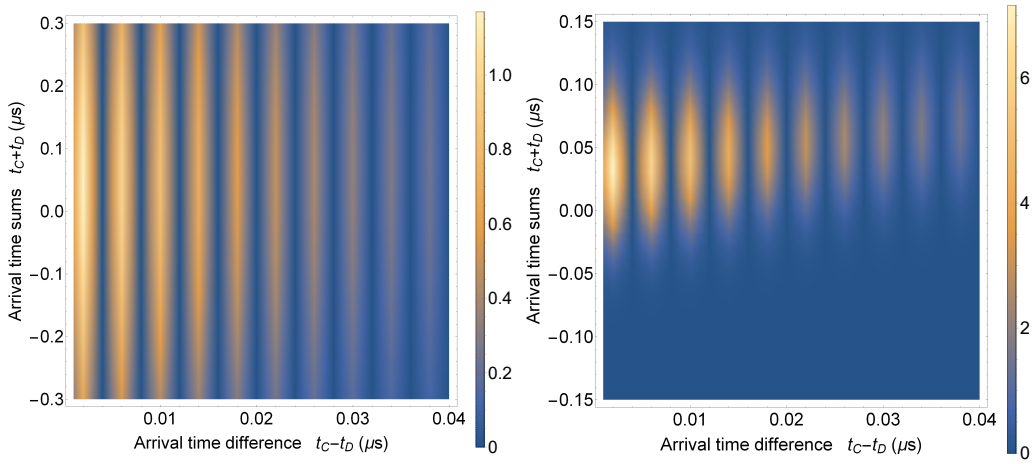


(a) $G^{(2)}_{C,D}$ for $\sigma_p = 2\pi \times 0.5\,\mathrm{MHz}$

(b) $G^{(2)}_{C,D}$ for $\sigma_p = 2\pi \times 5\,\mathrm{MHz}$

Figure 6.10: Modelled AHC coincidences $G^{(2)}_{C,D}$ for various pump bandwidths, for a CESPDC cavity bandwidth of 7 MHz and $\omega_- = 2\pi \times 250\,\mathrm{MHz}$. Oscillations in the coincidences along the $t_-$ axis correspond to the inverse of the frequency spacing. The drop in coincidences along the $t_-$ axis gives the 2-photon correlation time or bandwidth. The Gaussian profile of coincidences in the $t_+$ axis has a FWHM which is the inverse of the pump bandwidth. The $t_+$ distribution is centred on $t_+ \approx 0.05\,\mu s$, which is the group delay produced by the filter cavities.

eigenvalues and $\sum_n \lambda_n = 1$. The JSA is perfectly separable if it can be expressed as a product of some $S_0(\omega_s)I_0(\omega_i)$, in which case the sole Schmidt coefficient is $\lambda_0 = 1$. In this case the signal spectral amplitude is given solely by $S_0(\omega_s)$ while the idler spectral amplitude is $I_0(\omega_i)$ and the two-photon state is a product of two pure states, one each for the signal and idler. Figures of merit such as Schmidt number $K = 1/\sum_n \lambda_n^2$ and the entanglement entropy $E_{ent} = \sum_{i=1}^{n} \lambda_n \log_2 \lambda_n$ are useful to characterise the entanglement in such a bipartite state. The entropy of entanglement ranges from 0 to $\infty$ and the Schmidt number from 1 to 0 for a product state to a maximally entangled state.

In practice, systems that produce nearly separable two-photon states, typically employ pulsed pump fields, which have the effect of broadening the JSA along the $\omega_+$ dimension, thereby producing signal-idler pairs which are less anti-correlated. Here we study this scenario and show how AHC can be applied to it.

We write the pump field $E_p(t)$ in terms of its Fourier amplitudes $\alpha(\omega_p)$

$$E_p(t) = \int d\omega_p \alpha(\omega_p) e^{-i\omega_p t}. \tag{6.37}$$

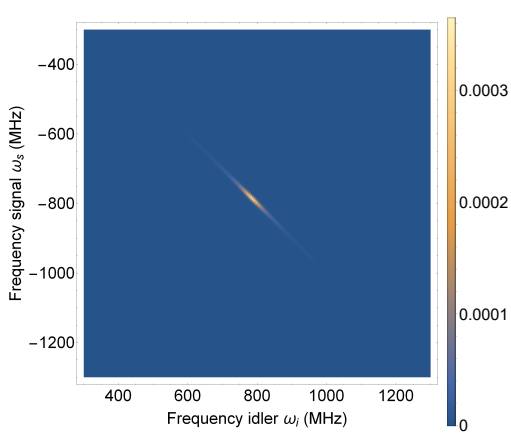


(a) JSA magnitude $|f(\omega_s, \omega_i)|$ for $\sigma_p = 2\pi \times 0.5\,\mathrm{MHz}$

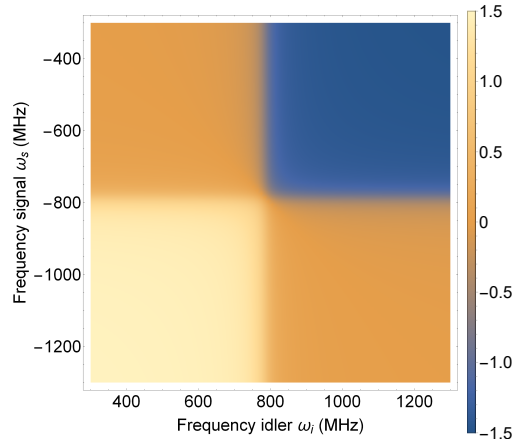


(b) JSA phase $\arg[f(\omega_s, \omega_i)]$ for $\sigma_p = 2\pi \times 0.5\,\mathrm{MHz}$

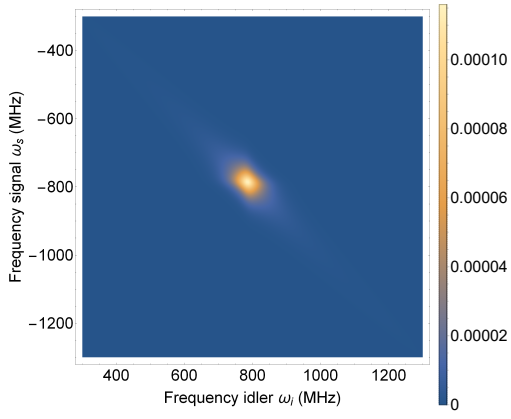


(c) JSA magnitude $|f(\omega_s, \omega_i)|$ for $\sigma_p = 2\pi \times 5\,\mathrm{MHz}$

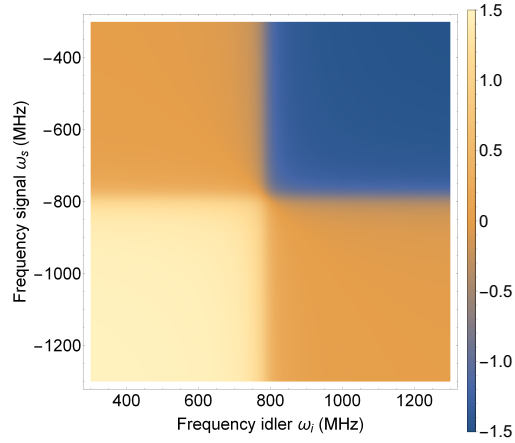


(d) JSA phase $\arg[f(\omega_s, \omega_i)]$ for $\sigma_p = 2\pi \times 5\,\mathrm{MHz}$

Figure 6.11

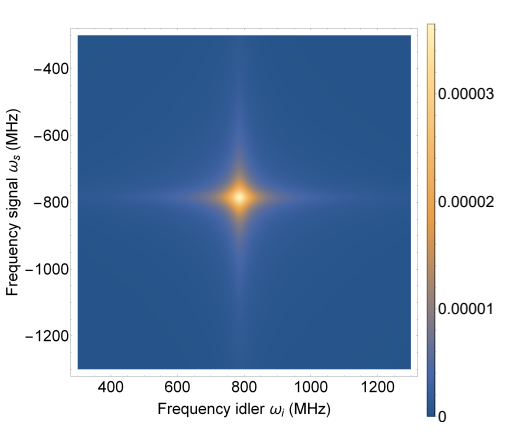


(e) JSA magnitude $|f(\omega_s, \omega_i)|$ for $\sigma_p = 2\pi \times 50\,\text{MHz}$

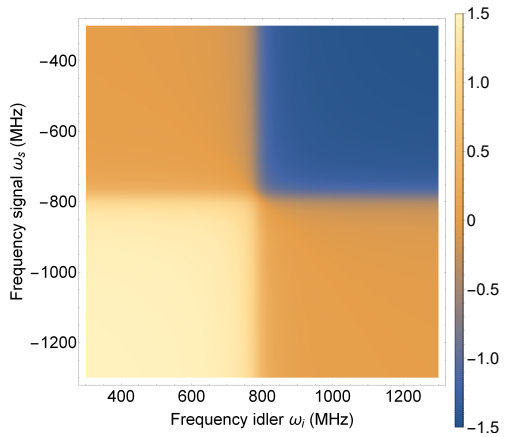


(f) JSA phase $\arg[f(\omega_s, \omega_i)]$ for $\sigma_p = 2\pi \times 50\,\text{MHz}$

Figure 6.11: JSA for various pump bandwidths inferred from autoheterodyne results. Plots (a) and (b) correspond to the JSA when the pump is narrowband. In this scenario the photons are highly correlated with an entanglement entropy of 4.4. Plots (c) and (d) correspond to a pump bandwidth comparable to the 2-photon bandwidth and thus there is lesser entanglement with the down-converted photons. The entanglement entropy in this case is 1.8. Plots (e) and (f) give the JSA for a very broadband pump and the entanglement entropy here is 0.2, much closer to the limit of 0 for a pure state.

The two-photon state from the filtered CE-SPDC system is as in Equation 6.9 above, with

$$f(\omega_s, \omega_i) \quad \propto \quad \int d\omega_p \delta(\omega_p - \omega_s - \omega_i)\alpha(\omega_p) \prod_{\nu\in\{s,i\}} \frac{1}{\gamma_\nu/2 + i\,(\omega_\nu^0 - \omega_\nu)}. \tag{6.38}$$

Here $\omega_{s,i}^0$ and $\gamma$ are the center frequencies and linewidth of two cavity modes. If we take $\alpha(\omega_p)$ to be a Gaussian of RMS width $\sigma_p$, we have the JSA for a narrowband SPDC source with a pulsed pump.

We now show how AHC can be applied to a state generated in this way. The two-photon state in the sum and difference co-ordinates is,

$$|\psi\rangle = \int \frac{1}{2} d\omega_+ d\omega_- \mathring{f}_A(\omega_+, \omega_-)\hat{a}_s^\dagger\left(\frac{\omega_+ + \omega_-}{2}\right)\hat{a}_i^\dagger\left(\frac{\omega_+ - \omega_-}{2}\right)|0\rangle\,. \tag{6.39}$$

Performing the integral over $\omega_p$ in Equation 6.38 we find

$$\mathring{f}_A(\omega_+, \omega_-) \propto \alpha(\omega_+) \frac{1}{\gamma + i\,(2\omega_s^0 - \omega_+ - \omega_-)} \frac{1}{\gamma + i\,(2\omega_i^0 - \omega_+ + \omega_-)}. \quad (6.40)$$

Using this in Equation 6.21 and Equation 6.25, we compute the AHC signals. The correlation function $G^{(2)}_{CD}(t, t')$ for various pump bandwidths is shown in Figure 6.10. The other AHC signals, $G^{(2)}_{CC}(t, t')$ and $G^{(2)}_{DD}(t, t')$ look similar, but the "beating," i.e. oscillation with $t - t'$, is 180° out of phase. These signals are directly observable by measuring the arrival times of the photons at detectors C and D, and provide spectral information about the JSA. As described in equations Equation 6.21 and Equation 6.25, the various $G^{(2)}$ functions can be expressed as the square magnitude of a two-dimensional Fourier transform (the usual complex Fourier transform along the $\omega_+$ axis and either a sine or cosine transform along the $\omega_-$ axis).

As with more established methods [79], the AHC observations can be compared against the theoretical model, for validation and to estimate parameters such as $\gamma$, $\sigma_p$ and $\omega_s^0 - \omega_i^0$. From the modelled JSA, with parameters found by measurement, the state purity and other figures of merit can then be computed numerically. The Schmidt number and entanglement entropy can be estimated by computing the singular value decomposition on discretising the JSA [113]. Examples are shown graphically in Figure 6.11.

# 7

# CONCLUSION

## 7.1 SUMMARY OF RESULTS

We have described a CE-SPDC source for tuneable, narrowband, frequency anti-correlated photon pairs, each of which can be tuned to the same or different transitions in the rubidium spectrum. The photon source is a type-II phase matched nonlinear crystal, pumped with a monochromatic pump, within a doubly-resonant optical parametric oscillator (OPO) operated far below threshold. The tuneability is achieved by controlling the length of the OPO and temperature tuning the birefringence using an additional crystal, thereby exerting control over the free spectral ranges of the OPO.

The power decay rate in the down-conversion cavity for V polarised light at 794.7 nm is $\gamma_s = 2\pi \times 6.98(4)$ MHz and the cavity power decay rate for H polarised light at the same wavelength is $\gamma_i = 2\pi \times 6.16(24)$ MHz [1]. The FWHM of the signal and idler modes from CE-SPDC, are equal to the two-photon linewidth $\gamma_{tp} = 2\pi \times 4.2$ MHz. Due to birefringence in the down-conversion cavity, the FSRs of the down-converted signal and idler modes are different. As a result, the spectrum of the signal/idler from the source is in clusters of frequency modes. Through DFG we have measured the frequency spacing between clusters to be $\omega_{cluster} = 2\pi \times 70.7$ GHz. This implies a difference in free spectral ranges between the V polarised signal mode and the H polarised idler mode of $\Delta FSR = FSR_s - FSR_i = 2\pi \times 3.5(1)$ MHz. The mean free spectral range $FSR_{mean} = 2\pi \times 496$ MHz. The enhancement in spectral brightness at the signal-idler pair frequencies corresponding to exact cavity resonance scales as the square of the finesse and is $\sim 1000$ for our down-conversion cavity.

1 Values reported in subsubsection 5.3.2

A single spectral mode pair is selected from the CE-SPDC output using a frequency tuneable Fabry-Perot (FP) filter on each of the signal and idler arms. The FP filters are identical in design. Tuneability of the FP filter is achieved by changing its temperature, as this alters the length of a spacer that determines the cavity length and its resonance frequency. The filter has a power decay rate of $\gamma_f = 2\pi \times 96.6(9)$ MHz, a free spectral range of $FSR_f = 2\pi \times 39.4$ GHz and an on resonance maximum transmission of $\approx 90\%$. The sensitivity of the FP resonance frequency to temperature is $1.24\,\mathrm{MHz\,mK^{-1}}$. The resolution with which its temperature can be adjusted is 5 mK around room temperature. The resolution increases with decreasing temperature.

Using an interconnected frequency stabilising scheme that controls the frequencies of the lasers and cavity resonances, we are able to tune the individual frequencies of the signal and idler in a down-converted pair from degeneracy to a maximum range of 1.8 GHz with MHz resolution

From second order intensity cross-correlations measurements between the down-converted signal and idler modes, we measure a two-photon correlation time of 33(4) ns. We estimate a pair-production rate per unit pump power in the crystal to be $11(5) \times 10^3\,\mathrm{pairs\,s^{-1}\,mW^{-1}}$, in the central mode that we filter and detect. The rate of coincidences is $1050\,\mathrm{counts\,s^{-1}\,mW^{-1}}$ when the chopper is open. We measure a heralding efficiency of $\eta_H = 36(6)\%$. The measured coincidence rate and the quantum efficiency of the detectors imply $\sim 4000\,\mathrm{pairs\,s^{-1}\,mW^{-1}}$ of correlated photon pairs in fiber and $720\,\mathrm{s^{-1}\,mW^{-1}}$ of heralded signal photons available for cold atom experiments when the chopper is open. Measurements of the heralded autocorrelation function at zero delay give $g^{(2)}_{s,s|i} = 0.026(3)$ at 1 mW of pump power.

We have introduced a new technique called autoheterodyne characterisation (AHC) to quantify the frequency correlations of photon pairs, and applied it to measure the spectral content from our filtered CE-SPDC source. By interfering the photons on a BS and performing Fourier analysis on the temporal auto and cross-correlations, AHC directly measures the beat-note spectrum with the spectral resolution limited only by the acquisition time. The technique is simple to implement with one detector via the temporal Ghosh-Mandel effect, or with two detectors via the nondegenerate Hong-Ou-Mandel effect. Here is a partial list of features of a two-photon state that can be obtained from the method.

- A high-resolution frequency-difference spectrum. This includes not just the frequency spacing between signal and idler photons, but also quantitative mea-

surement of contamination with other frequencies, e.g. from unwanted cavity modes. This is fundamental to any narrowband application, including interaction of photons or photon pairs with atoms, ions, or molecules.

- The time-sum distribution, also with high resolution. This could be useful, for example, in characterising the pump pulses. This is useful in any application for which the pump characteristics are important, e.g. producing heralded single photons in pure states.
- The cavity relaxation time, in cases where a cavity determines the spectral properties of the the photon pairs. This is seen directly in the double-exponential envelope of the $G^{(2)}(t - t')$ distribution. This is useful for bandwidth matching of the SPDC photons to material systems such as atoms, and also for bandwidth matching between different photon sources.
- Information from the $G^{(2)}(t, t')$ measurements can be used to validate or disprove a model for the JSA, and to find unknown parameters in that model, e.g. line widths. This gives basic information about the SPDC process.
- A model-derived JSA can be used to compute correlation strengths, state purity and entanglement entropy. This is useful in multi-photon interferometry for several quantum technology applications.

We scrutinise our model for the JSA from our filtered CE-SPDC source using AHC and verify that the two-photon spectrum is well described by a single frequency mode each for the signal and idler. Power spectral analysis of the AHC results show that the FP filters extinguish unwanted frequency modes from the CE-SPDC output by over 25 dB.

## 7.2 SCOPE FOR IMPROVEMENT

As is the case with the first implementation of any system, there is room for improving the performance and ease of use of our experimental set-up too. Here we outline some immediate improvements that can be implemented in our system, for the benefit of future students.

On reading this thesis, one might have noticed that while we claim that signal and idler photons with any arbitrary value of frequency difference between them can be

obtained using our source, all measurements that utilise nondegenerate photons have been performed with either 250 MHz or around 165 MHz of frequency difference between the signal and idler. The reason for this is that we had only one frequency stabilised laser at 795 nm (the reference laser) available for all measurements. To change the frequency difference between the required signal and idler modes, the frequency of the reference laser was scanned, and its light made diagonally polarised before it enters the down-conversion cavity, so it may excite both the H polarised idler mode and the V polarised signal modes in the cavity. The transmission of H and V modes was analysed in an oscilloscope and the temperature of the tuning crystal adjusted such that an idler resonance is either midway in frequency between adjacent signal resonances, making the frequency difference $\approx \mathrm{FSR}_{\mathrm{mean}}/2 \approx 250\,\mathrm{MHz}$, or $1/3^{\mathrm{rd}}$ in frequency between adjacent signal resonances, making the frequency difference $\approx \mathrm{FSR}_{\mathrm{mean}}/3 \approx 165\,\mathrm{MHz}$. This technique to determine the frequency difference has limited precision, and should in the future be replaced with a more precise and flexible system. Let us assume we require an arbitrary frequency difference $\Delta\nu_{\mathrm{diff}} = \nu_s - \nu_i$ between the required signal and idler CE-SPDC modes. At present, the light with frequency $\nu_{\mathrm{lock}}$, from the frequency stabilised reference laser, is used to stabilise the cavity such that the frequency of the signal mode $\nu_s = \nu_{\mathrm{lock}}$ and there is no reference light available to verify the frequency at which the idler is resonant in the cavity. However, if another laser at 795 nm is available and stabilised at a frequency $\nu_{\mathrm{lock}} - \Delta\nu_{\mathrm{diff}}$, the resonance frequency of the idler mode can be verified by looking at the transmission of H polarised light from this laser. For this, the second laser can be stabilised using a PLL lock, referenced to a beat note with the original reference laser.

The next source of limitation in the range of possible frequency differences between the signal and idler, is the maximum frequency detuning possible between the pump and the SHG light. This is limited by the bandwidth of the detector for the beat-note between the SHG and pump light. At present we use a detector with a bandwidth of 1.5 GHz and as a consequence, the maximum possible frequency difference between the signal and idler photon is 1.82 GHz. This range can be increased by replacing the existing detector with one that has a larger bandwidth.

The locking mechanism for the CE-SPDC cavity could be improved. A PID circuit, implemented in a FPGA board, feeds back to the piezo voltage to maintain cavity resonance. From time to time this PID hits a rail, i.e. reaches its maximum or minimum output voltage, and the cavity loses lock. This loss of lock is in principle fully avoidable,

because the FPGA output range includes more than one resonance mode of the cavity. If, when the controller reaches a rail, it were to jump to the next resonance, the system could remain locked indefinitely despite large drifts in temperature and pressure.

The photons from this source will be used for interaction with a single Rb atom in a dipole trap. The architecture of the atom trap is such that once an atom randomly falls into the trap, its lifetime in the trap is around a second, during which time it is available for atom-photon experiments. We observe that, under quiet laboratory conditions, the CE-SPDC cavity remains on resonance for about 1 second in the absence of active stabilisation. This suggest the possibility to program the chopper (used in the CE-SPDC cavity locking scheme), such that when an atom falls into the dipole trap, the chopper opens the path for the photons to reach the atom for a duration of around a second.

## 7.3 OUTLOOK

The introduction provided a broad discussion on the applications and relevance of the techniques developed during this thesis. Here we discuss ideas that we would have liked to explore during the course of this thesis, but did not due to limitations in time.

### 7.3.1 Towards atom-photon experiments

Due to the type-II phase matching employed and the control over the spectral properties of the down-converted photons, the photons from our source can be easily entangled in the polarisation and/or energy-time degrees of freedom, making them suitable for quantum networking applications such as entangling different material systems. This versatile source, capable of producing both correlated and indistinguishable photons, will also open up possibilities to explore new aspects of matter-induced nonlinearity at the single photon level and exotic quantum interference effects.

The first steps towards studying quantum light-matter interactions, would be to quantify the efficiency of the interface between the photons from our source and the cold single Rb atom that other members of our team have trapped. The atom sits at the centre of 4 high NA lenses that allow us to probe it from different directions. The first step will be to perform heralded single photon-atom measurements, to quantify the probability of interaction of a single photon with a single atom. For this, we will send one photon from the pair to the atom and use the other as a herald. The ratio of

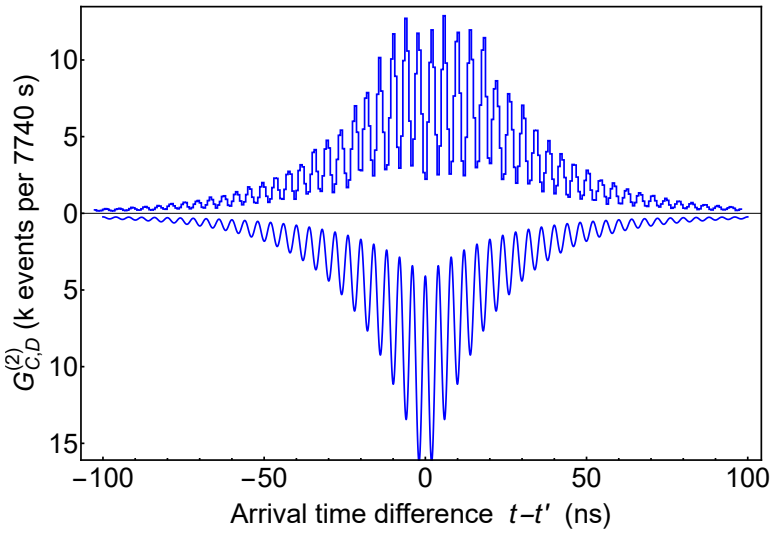


Figure 7.1: Autoheterodyne coincidences $G^{(2)}_{C,D}$ for a narrowband pump and $\omega^0_- = 2\pi \times 250\,\mathrm{MHz}$. Upper curve shows histogram of coincidences recorded for arrival time differences with 625 ps time bins, when a delay is introduced in the relative path taken by the photons to the BS. Lower curve shows predicted $G^{(2)}_{C,D}$ in the absence of a relative delay. Experimental results show a clear modification in the $G^{(2)}$ profile as a consequence of phase sensitivity, when compared with the results in Figure 6.7 where no delay was introduced in the relative path. The experimental results show a "flat-top" and reduced visibility that can be modelled as a sum of two overlapping oscillations with a double exponential envelope offset by a time corresponding to the relative delay between the photons.

photons that pass through the atom trap undeviated to those collected from the lenses perpendicular to the direction of probing, will give us the probability of interaction of a single photon with the atom. This information is important for determining the duty cycle and repetition rates of our future experiments in order to obtain statistically significant results.

### 7.3.2 Future work with AHC

The AHC technique is well suited to characterise narrowband photon sources for interaction with atoms and ions, which typically require bandwidths below 10 MHz.

The technique may be especially valuable in quantum networking, computing and simulation with mixed photon-atom systems.

As shown in section 6.5, the technique can be applied to CE-SPDC with pulsed pumps to characterise the entanglement in the down-converted photons. Since the technique gives access to the sum frequency information in the down-converted pair through its Fourier transform, narrow sum frequencies i.e., pump bandwidths less than or comparable to the CE-SPDC two-photon bandwidth are well resolved by this technique. Thus, the technique can be readily applied when sub MHz to 10s of MHz bandwidth pumps are used. Such quasi cw-pumping is common when the pulsing is used to synchronise photon pair generation from SPDC. However, for larger bandwidth pump pulses, we would run into two issues. First and foremost, the detector timing resolution may not be good enough to resolve the sum frequency distribution in this case. Secondly, we note that the results for broadband pumping in section 6.5 were derived under the assumption of a single signal-idler mode pair, and may not hold when a very broadband pump is used. For our filtered CE-SPDC source, there are multiple frequency scales involved like the CE-SPDC FSR, the filter linewidth and filter FSR. If the pump bandwidth is comparable or larger than these frequency scales, the spectrum of the CE-SPDC output and consequently the physics of the AHC results would get more complicated. This remains to be investigated.

We note that the $G^{(2)}(t, t')$ functions in AHC are sensitive to the phases in the JSA $f(\omega_s, \omega_i)$. These phases can be manipulated in a controlled way through delays of signal and/or idler. We illustrate this in Figure 7.1. Although it is a topic for further research, we believe this could offer a convenient way to make a tomographic measurement of the full JSA, including phases. Proposals for phase detecting in the JSA using variable path length delays in HOM interferometry have been made [143]. These could be implemented with narrowband photons and the AHC in a single experimental run without the need for changing conditions such as the path length.

There have been proposals to use hyper-entangled states for discrimination of all four Bell states [144]. Since the temporal Ghosh-Mandel effect is sensitive to the exchange-symmetric part of the state and the nondegenerate HOM to the exchange-antisymmetric part of the state, it would be interesting to investigate how such proposals can be extended to involve AHC and states entangled in both time-energy and polarisation.

# BIBLIOGRAPHY


[1] C. K. Hong, Z. Y. Ou, and L. Mandel, "Measurement of subpicosecond time intervals between two photons by interference," Phys. Rev. Lett. **59**, 2044 (1987).

[2] P. G. Kwiat, K. Mattle, H. Weinfurter, A. Zeilinger, A. V. Sergienko, and Y. Shih, "New high-intensity source of polarization-entangled photon pairs," Phys. Rev. Lett. **75**, 4337 (1995).

[3] A. Aspect, P. Grangier, and G. Roger, "Experimental realization of Einstein-Podolsky-Rosen-Bohm gedankenexperiment: A new violation of Bell's inequalities," Phys. Rev. Lett. **49**, 91 (1982).

[4] J. L. O'Brien, G. J. Pryde, A. G. White, T. C. Ralph, and D. Branning, "Demonstration of an all-optical quantum controlled-NOT gate," Nature **426**, 264 (2003).

[5] F. Wolfgramm, C. Vitelli, F. A. Beduini, N. Godbout, and M. W. Mitchell, "Entanglement-enhanced probing of a delicate material system," Nature Photonics **7**, 28 (2013).

[6] P. Kochan and H. J. Carmichael, "Photon-statistics dependence of single-atom absorption," Phys. Rev. A **50**, 1700 (1994).

[7] A. Roulet, H. N. Le, and V. Scarani, "Two photons on an atomic beam splitter: Nonlinear scattering and induced correlations," Phys. Rev. A **93**, 033838 (2016).

[8] A. Nysteen, P. T. Kristensen, D. P. S. McCutcheon, P. Kaer, and J. Mørk, "Scattering of two photons on a quantum emitter in a one-dimensional waveguide: exact dynamics and induced correlations," New Journal of Physics **17**, 023030 (2015).

[9] A. Nysteen, D. P. S. McCutcheon, and J. Mørk, "Strong nonlinearity-induced correlations for counterpropagating photons scattering on a two-level emitter," Phys. Rev. A **91**, 063823 (2015).

[10] C. Couteau, "Spontaneous parametric down-conversion," Contemporary Physics **59**, 291 (2018).

[11] H. J. Kimble, M. Dagenais, and L. Mandel, "Photon antibunching in resonance fluorescence," Phys. Rev. Lett. **39**, 691 (1977).

[12] P. Goy, J. M. Raimond, M. Gross, and S. Haroche, "Observation of cavity-enhanced single-atom spontaneous emission," Phys. Rev. Lett. **50**, 1903 (1983).

[13] P. Münstermann, T. Fischer, P. Maunz, P. W. H. Pinkse, and G. Rempe, "Dynamics of single-atom motion observed in a high-finesse cavity," Phys. Rev. Lett. **82**, 3791 (1999).

[14] J. Ye, D. W. Vernooy, and H. J. Kimble, "Trapping of single atoms in cavity QED," Phys. Rev. Lett. **83**, 4987 (1999).

[15] T. Sauter, W. Neuhauser, R. Blatt, and P. E. Toschek, "Observation of quantum jumps," Phys. Rev. Lett. **57**, 1696 (1986).

[16] C. Monroe, D. M. Meekhof, B. E. King, W. M. Itano, and D. J. Wineland, "Demonstration of a fundamental quantum logic gate," Phys. Rev. Lett. **75**, 4714 (1995).

[17] N. Schlosser, G. Reymond, I. Protsenko, and P. Grangier, "Sub-poissonian loading of single atoms in a microscopic dipole trap," Nature **411**, 1024 EP (2001).

[18] M. K. Tey, Z. Chen, S. A. Aljunid, B. Chng, F. Huber, G. Maslennikov, and C. Kurtsiefer, "Strong interaction between light and a single trapped atom without the need for a cavity," Nature Physics **4**, 924 (2008).

[19] M. K. Tey, G. Maslennikov, T. C. H. Liew, S. A. Aljunid, F. Huber, B. Chng, Z. Chen, V. Scarani, and C. Kurtsiefer, "Interfacing light and single atoms with a lens," New Journal of Physics **11**, 043011 (2009).

[20] S. A. Aljunid, M. K. Tey, B. Chng, T. Liew, G. Maslennikov, V. Scarani, and C. Kurtsiefer, "Phase shift of a weak coherent beam induced by a single atom," Phys. Rev. Lett. **103**, 153601 (2009).

[21] S. A. Aljunid, G. Maslennikov, Y. Wang, H. L. Dao, V. Scarani, and C. Kurtsiefer, "Excitation of a single atom with exponentially rising light pulses," Phys. Rev. Lett. **111**, 103001 (2013).

[22] G. Wrigge, I. Gerhardt, J. Hwang, G. Zumofen, and V. Sandoghdar, "Efficient coupling of photons to a single molecule and the observation of its resonance fluorescence," Nature Physics **4**, 60 EP (2007).

[23] H. de Riedmatten, M. Afzelius, M. U. Staudt, C. Simon, and N. Gisin, "A solid-state light–matter interface at the single-photon level," Nature **456**, 773 EP (2008).

[24] M. Sondermann and G. Leuchs, "Light–matter interaction in free space," Journal of Modern Optics **60**, 36 (2013).

[25] M. Hennrich, A. Kuhn, and G. Rempe, "Transition from antibunching to bunching in cavity QED," Physical Review Letters **94**, 053604 (2005).

[26] M. Steiner, V. Leong, M. A. Seidler, A. Cerè, and C. Kurtsiefer, "Photon bandwidth dependence of light-matter interaction," Opt. Express **25**, 6294 (2017).

[27] V. Leong, M. A. Seidler, M. Steiner, A. Cerè, and C. Kurtsiefer, "Time-resolved scattering of a single photon by a single atom," Nature Communications **7**, 13716 (2016).

[28] F. Monteiro, A. Martin, B. Sanguinetti, H. Zbinden, and R. T. Thew, "Narrowband photon pair source for quantum networks," Opt. Express **22**, 4371 (2014).

[29] E. Distante, P. Farrera, A. Padrón-Brito, D. Paredes-Barato, G. Heinze, and H. de Riedmatten, "Storing single photons emitted by a quantum memory on a highly excited rydberg state," Nature Communications **8**, 14072 (2017).

[30] A. Seri, A. Lenhard, D. Rieländer, M. Gündoğan, P. M. Ledingham, M. Mazzera, and H. de Riedmatten, "Quantum correlations between single telecom photons and a multimode on-demand solid-state quantum memory," Phys. Rev. X **7**, 021028 (2017).

[31] A. Haase, N. Piro, J. Eschner, and M. W. Mitchell, "Tunable narrowband entangled photon pair source for resonant single-photon single-atom interaction," Opt. Lett. **34**, 55 (2009).

[32] Z. Y. Ou and Y. J. Lu, "Cavity enhanced spontaneous parametric down-conversion for the prolongation of correlation time between conjugate photons," Phys. Rev. Lett. **83**, 2556 (1999).

[33] O. Slattery, L. Ma, K. Zong, and X. Tang, "Background and review of cavity-enhanced spontaneous parametric down-conversion," Journal of Research of the National Institute of Standards and Technology **124**, 1 (2019).

[34] E. M. Purcell, "Proceedings of the American Physical Society," Physical Review **69**, 681 (1946).

[35] M. Oberparleiter and H. Weinfurter, "Cavity-enhanced generation of polarization-entangled photon pairs," Optics Communications **183**, 133 (2000).

[36] M. Scholz, F. Wolfgramm, U. Herzog, and O. Benson, "Narrow-band single photons from a single-resonant optical parametric oscillator far below threshold," Applied Physics Letters **91**, 191104 (2007).

[37] F. Wolfgramm, X. Xing, A. Cerè, A. Predojević, A. M. Steinberg, and M. W. Mitchell, "Bright filter-free source of indistinguishable photon pairs," Opt. Express **16**, 18145 (2008).

[38] X.-H. Bao, Y. Qian, J. Yang, H. Zhang, Z.-B. Chen, T. Yang, and J.-W. Pan, "Generation of narrow-band polarization-entangled photon pairs for atomic quantum memories," Phys. Rev. Lett. **101**, 190501 (2008).

[39] F.-Y. Wang, B.-S. Shi, and G.-C. Guo, "Generation of narrow-band photon pairs for quantum memory," Optics Communications **283**, 2974 (2010).

[40] J. Fekete, D. Rieländer, M. Cristiani, and H. de Riedmatten, "Ultranarrow-band photon-pair source compatible with solid state quantum memories and telecommunication networks," Physical Review Letters **110**, 220502 (2013).

[41] M. Rambach, A. Nikolova, T. J. Weinhold, and A. G. White, "Sub-megahertz linewidth single photon source," APL Photonics **1**, 096101 (2016).

[42] A. Ahlrichs and O. Benson, "Bright source of indistinguishable photons based on cavity-enhanced parametric down-conversion utilizing the cluster effect," Applied Physics Letters **108**, 021111 (2016).

[43] C. Schuck, F. Rohde, N. Piro, M. Almendros, J. Huwer, M. W. Mitchell, M. Hennrich, A. Haase, F. Dubin, and J. Eschner, "Resonant interaction of a single atom with single photons from a down-conversion source," Physical Review A **81**, 011802 (2010).

[44] N. Piro, F. Rohde, C. Schuck, M. Almendros, J. Huwer, J. Ghosh, A. Haase, M. Hennrich, F. Dubin, and J. Eschner, "Heralded single-photon absorption by a single atom," Nature Physics **7**, 17 (2011).

[45] C. Clausen, I. Usmani, F. Bussières, N. Sangouard, M. Afzelius, H. de Riedmatten, and N. Gisin, "Quantum storage of photonic entanglement in a crystal," Nature **469**, 508 (2011).

[46] H. Zhang, X.-M. Jin, J. Yang, H.-N. Dai, S.-J. Yang, T.-M. Zhao, J. Rui, Y. He, X. Jiang, F. Yang, G.-S. Pan, Z.-S. Yuan, Y. Deng, Z.-B. Chen, X.-H. Bao, S. Chen, B. Zhao, and J.-W. Pan, "Preparation and storage of frequency-uncorrelated entangled photons from cavity-enhanced spontaneous parametric downconversion," Nature Photonics **5**, 628 (2011).

[47] D. Rieländer, K. Kutluer, P. M. Ledingham, M. Gündoğan, J. Fekete, M. Mazzera, and H. de Riedmatten, "Quantum storage of heralded single photons in a praseodymium-doped crystal," Physical Review Letters **112**, 040504 (2014).

[48] A. Lenhard, M. Bock, C. Becher, S. Kucera, J. Brito, P. Eich, P. Müller, and J. Eschner, "Telecom-heralded single-photon absorption by a single atom," Phys. Rev. A **92**, 063827 (2015).

[49] G. Schunk, U. Vogl, D. V. Strekalov, M. Förtsch, F. Sedlmeir, H. G. L. Schwefel, M. Göbelt, S. Christiansen, G. Leuchs, and C. Marquardt, "Interfacing transitions of different alkali atoms and telecom bands using one narrowband photon pair source," Optica **2**, 773 (2015).

[50] U. Paudel, J. J. Wong, M. Goggin, P. G. Kwiat, A. S. Bracker, M. Yakes, D. Gammon, and D. G. Steel, "Direct excitation of a single quantum dot with cavity-SPDC photons," Opt. Express **27**, 16308 (2019).

[51] P.-J. Tsai, Y.-F. Hsiao, and Y.-C. Chen, "Quantum storage and manipulation of heralded single photons in atomic memories based on electromagnetically induced transparency," Phys. Rev. Research **2**, 033155 (2020).

[52] D. Lago-Rivera, S. Grandi, J. V. Rakonjac, A. Seri, and H. de Riedmatten, "Telecom-heralded entanglement between multimode solid-state quantum memories," Nature **594**, 37 (2021).

[53] S. E. Harris and Y. Yamamoto, "Photon switching by quantum interference," Phys. Rev. Lett. **81**, 3611 (1998).

[54] S. E. Harris and L. V. Hau, "Nonlinear optics at low light levels," Phys. Rev. Lett. **82**, 4611 (1999).

[55] D. E. Chang, A. S. Sørensen, E. A. Demler, and M. D. Lukin, "A single-photon transistor using nanoscale surface plasmons," Nature Physics **3**, 807 EP (2007).

[56] J. Hwang, M. Pototschnig, R. Lettow, G. Zumofen, A. Renn, S. Götzinger, and V. Sandoghdar, "A single-molecule optical transistor," Nature **460**, 76 (2009).

[57] P. Kolchin, R. F. Oulton, and X. Zhang, "Nonlinear quantum optics in a waveguide: Distinct single photons strongly interacting at the single atom level," Phys. Rev. Lett. **106**, 113601 (2011).

[58] T. Peyronel, O. Firstenberg, Q.-Y. Liang, S. Hofferberth, A. V. Gorshkov, T. Pohl, M. D. Lukin, and V. Vuletić, "Quantum nonlinear optics with single photons enabled by strongly interacting atoms," Nature **488**, 57 (2012).

[59] J. Perczel, J. Borregaard, D. E. Chang, H. Pichler, S. F. Yelin, P. Zoller, and M. D. Lukin, "Topological quantum optics in two-dimensional atomic arrays," Physical Review Letters **119**, 023603 (2017).

[60] A. Asenjo-Garcia, M. Moreno-Cardoner, A. Albrecht, H. J. Kimble, and D. E. Chang, "Exponential improvement in photon storage fidelities using subradiance and "selective radiance" in atomic arrays," Phys. Rev. X **7**, 031024 (2017).

[61] J. Rui, D. Wei, A. Rubio-Abadal, S. Hollerith, J. Zeiher, D. M. Stamper-Kurn, C. Gross, and I. Bloch, "A subradiant optical mirror formed by a single structured atomic layer," Nature **583**, 369 (2020).

[62] S. J. Masson and A. Asenjo-Garcia, "Atomic-waveguide quantum electrodynamics," Phys. Rev. Research **2**, 043213 (2020).

[63] I. H. Deutsch, R. Y. Chiao, and J. C. Garrison, "Diphotons in a nonlinear fabry-pérot resonator: Bound states of interacting photons in an optical "quantum wire"," Phys. Rev. Lett. **69**, 3627 (1992).

[64] Y. Ke, J. Zhong, A. V. Poshakinskiy, Y. S. Kivshar, A. N. Poddubny, and C. Lee, "Radiative topological biphoton states in modulated qubit arrays," Phys. Rev. Research **2**, 033190 (2020).

[65] M. W. Mitchell, C. I. Hancox, and R. Y. Chiao, "Dynamics of atom-mediated photon-photon scattering," Phys. Rev. A **62**, 043819 (2000).

[66] W. Chen, K. M. Beck, R. Bücker, M. Gullans, M. D. Lukin, H. Tanji-Suzuki, and V. Vuletić, "All-optical switch and transistor gated by one stored photon," Science **341**, 768 (2013).

[67] J. Volz, M. Scheucher, C. Junge, and A. Rauschenbeutel, "Nonlinear phase shift for single fibre-guided photons interacting with a single resonator-enhanced atom," Nature Photonics **8**, 965 EP (2014).

[68] V. Prakash, L. C. Bianchet, M. T. Cuairan, P. Gomez, N. Bruno, and M. W. Mitchell, "Narrowband photon pairs with independent frequency tuning for quantum light-matter interactions," Opt. Express **27**, 38463 (2019).

[69] N. Bruno, L. C. Bianchet, V. Prakash, N. Li, N. Alves, and M. W. Mitchell, "Maltese cross coupling to individual cold atoms in free space," Opt. Express **27**, 31042 (2019).

[70] L. Bianchet, N. Alves, L. Zarraoa, N. Bruno, and M. Mitchell, "Manipulating and measuring single atoms in the maltese cross geometry [version 1; peer review: awaiting peer review]," Open Research Europe **1** (2021), 10.12688/openreseurope.13972.1.

[71] A. M. Kaufman, B. J. Lester, C. M. Reynolds, M. L. Wall, M. Foss-Feig, K. R. A. Hazzard, A. M. Rey, and C. A. Regal, "Two-particle quantum interference in tunnel-coupled optical tweezers," Science **345**, 306 (2014).

[72] H. Labuhn, D. Barredo, S. Ravets, S. de Léséleuc, T. Macrì, T. Lahaye, and A. Browaeys, "Tunable two-dimensional arrays of single Rydberg atoms for realizing quantum ising models," Nature **534**, 667 EP (2016).

[73] S. Jennewein, M. Besbes, N. J. Schilder, S. D. Jenkins, C. Sauvan, J. Ruostekoski, J.-J. Greffet, Y. R. P. Sortais, and A. Browaeys, "Coherent scattering of near-resonant

light by a dense microscopic cold atomic cloud," Phys. Rev. Lett. **116**, 233601 (2016).

[74] Y.-S. Chin, M. Steiner, and C. Kurtsiefer, "Nonlinear photon-atom coupling with 4pi microscopy," Nature Communications **8**, 1200 (2017).

[75] C. Reimer, S. Sciara, P. Roztocki, M. Islam, L. Romero Cortés, Y. Zhang, B. Fischer, S. Loranger, R. Kashyap, A. Cino, S. T. Chu, B. E. Little, D. J. Moss, L. Caspani, W. J. Munro, J. Azaña, M. Kues, and R. Morandotti, "High-dimensional one-way quantum processing implemented on d-level cluster states," Nature Physics **15**, 148 (2019).

[76] O. Pfister, "Continuous-variable quantum computing in the quantum optical frequency comb," Journal of Physics B: Atomic, Molecular and Optical Physics **53**, 012001 (2019).

[77] T. Gerrits, F. Marsili, V. B. Verma, L. K. Shalm, M. Shaw, R. P. Mirin, and S. W. Nam, "Spectral correlation measurements at the Hong-Ou-Mandel interference dip," Phys. Rev. A **91**, 013830 (2015).

[78] Y.-H. Kim and W. P. Grice, "Measurement of the spectral properties of the two-photon state generated via type II spontaneous parametric downconversion," Opt. Lett. **30**, 908 (2005).

[79] K. Zielnicki, K. Garay-Palmett, D. Cruz-Delgado, H. Cruz-Ramirez, M. F. O'Boyle, B. Fang, V. O. Lorenz, A. B. U'Ren, and P. G. Kwiat, "Joint spectral characterization of photon-pair sources," Journal of Modern Optics **65**, 1141 (2018).

[80] W. Wasilewski, P. Wasylczyk, P. Kolenderski, K. Banaszek, and C. Radzewicz, "Joint spectrum of photon pairs measured by coincidence Fourier spectroscopy," Opt. Lett. **31**, 1130 (2006).

[81] S. Mittal, V. V. Orre, A. Restelli, R. Salem, E. A. Goldschmidt, and M. Hafezi, "Temporal and spectral manipulations of correlated photons using a time lens," Phys. Rev. A **96**, 043807 (2017).

[82] T. Gerrits, M. J. Stevens, B. Baek, B. Calkins, A. Lita, S. Glancy, E. Knill, S. W. Nam, R. P. Mirin, R. H. Hadfield, R. S. Bennink, W. P. Grice, S. Dorenbos, T. Zijlstra,

T. Klapwijk, and V. Zwiller, "Generation of degenerate, factorizable, pulsed squeezed light at telecom wavelengths," Opt. Express **19**, 24434 (2011).

[83] S. Wang, C.-X. Liu, J. Li, and Q. Wang, "Research on the Hong-Ou-Mandel interference with two independent sources," Scientific Reports **9**, 3854 (2019).

[84] V. Thiel, A. O. C. Davis, K. Sun, P. D'Ornellas, X.-M. Jin, and B. J. Smith, "Single-photon characterization by two-photon spectral interferometry," Opt. Express **28**, 19315 (2020).

[85] R. W. Boyd, Nonlinear Optics (Academic Press Inc., 1992).

[86] W. H. Louisell, A. Yariv, and A. E. Siegman, "Quantum fluctuations and noise in parametric processes. I," Phys. Rev. **124**, 1646 (1961).

[87] B. R. Mollow and R. J. Glauber, "Quantum theory of parametric amplification. I," Phys. Rev. **160**, 1076 (1967).

[88] B. R. Mollow and R. J. Glauber, "Quantum theory of parametric amplification. II," Phys. Rev. **160**, 1097 (1967).

[89] D. N. Klyshko, A. N. Penin, and B. F. Polkovnikov, "Parametric luminescence and light scattering by polaritons," Soviet Journal of Experimental and Theoretical Physics Letters **11**, 5 (1970).

[90] D. C. Burnham and D. L. Weinberg, "Observation of simultaneity in parametric production of optical photon pairs," Phys. Rev. Lett. **25**, 84 (1970).

[91] C. K. Hong and L. Mandel, "Theory of parametric frequency down conversion of light," Phys. Rev. A **31**, 2409 (1985).

[92] Z. Y. Ou and L. Mandel, "Violation of Bell's inequality and classical probability in a two-photon correlation experiment," Phys. Rev. Lett. **61**, 50 (1988).

[93] R. Ghosh, C. K. Hong, Z. Y. Ou, and L. Mandel, "Interference of two photons in parametric down conversion," Phys. Rev. A **34**, 3962 (1986).

[94] R. Ghosh and L. Mandel, "Observation of nonclassical effects in the interference of two photons," Phys. Rev. Lett. **59**, 1903 (1987).

[95] A. Ahlrichs, "Triply-resonant cavity-enhanced spontaneous parametric down-conversion," PhD dissertation, Humboldt-Universität zu Berlin (2019).

[96] B. E. Saleh and M. C. Teich, Fundamentals of photonics (John Wiley and Sons, 2019).

[97] J. A. Giordmaine and R. C. Miller, "Tunable coherent parametric oscillation in $LiNbO_3$ at optical frequencies," Phys. Rev. Lett. **14**, 973 (1965).

[98] A. Yariv and W. Louisell, "Theory of the optical parametric oscillator," IEEE Journal of Quantum Electronics **2**, 418 (1966).

[99] Y. J. Lu and Z. Y. Ou, "Optical parametric oscillator far below threshold: Experiment versus theory," Phys. Rev. A **62**, 033804 (2000).

[100] U. Herzog, M. Scholz, and O. Benson, "Theory of biphoton generation in a single-resonant optical parametric oscillator far below threshold," Phys. Rev. A **77**, 023826 (2008).

[101] M. Scholz, L. Koch, and O. Benson, "Statistics of narrow-band single photons for quantum memories generated by ultrabright cavity-enhanced parametric down-conversion," Phys. Rev. Lett. **102**, 063603 (2009).

[102] M. Scholz, L. Koch, and O. Benson, "Analytical treatment of spectral properties and signal — idler intensity correlations for a double-resonant optical parametric oscillator far below threshold," Optics Communications **282**, 3518 (2009).

[103] Y. Jeronimo-Moreno, S. Rodriguez-Benavides, and A. B. U'Ren, "Theory of cavity-enhanced spontaneous parametric downconversion," Laser Physics **20**, 1221 (2010).

[104] L. L. Sánchez-Soto, J. J. Monzón, and G. Leuchs, "The many facets of the fabry–perot," European Journal of Physics **37**, 064001 (2016).

[105] F. Wolfgramm, "Atomic quantum metrology with narrowband entangled and squeezed states of light," PhD dissertation, UPC - Universitat Politecnica de Catalunya (2012).

[106] A. Siegman, Lasers (University Science Books, 1986).

[107] K.-H. Luo, H. Herrmann, S. Krapick, B. Brecht, R. Ricken, V. Quiring, H. Suche, W. Sohler, and C. Silberhorn, "Direct generation of genuine single-longitudinal-mode narrowband photon pairs," New Journal of Physics **17**, 073039 (2015).

[108] E. Pomarico, B. Sanguinetti, C. I. Osorio, H. Herrmann, and R. T. Thew, "Engineering integrated pure narrow-band photon sources," New Journal of Physics **14**, 033008 (2012).

[109] R. C. Eckardt, C. D. Nabors, W. J. Kozlovsky, and R. L. Byer, "Optical parametric oscillator frequency tuning and control," J. Opt. Soc. Am. B **8**, 646 (1991).

[110] A. Henderson, M. Padgett, F. Colville, J. Zhang, and M. Dunn, "Doubly-resonant optical parametric oscillators: tuning behaviour and stability requirements," Optics Communications **119**, 256 (1995).

[111] K. Kato and E. Takaoka, "Sellmeier and thermo-optic dispersion formulas for KTP," Appl. Opt. **41**, 5040 (2002).

[112] A. Eckstein, G. Boucher, A. Lemaître, P. Filloux, I. Favero, G. Leo, J. E. Sipe, M. Liscidini, and S. Ducci, "High-resolution spectral characterization of two photon states via classical measurements," Laser & Photonics Reviews **8**, L76 (2014).

[113] A. M. Brańczyk, T. C. Ralph, W. Helwig, and C. Silberhorn, "Optimized generation of heralded Fock states using parametric down-conversion," New Journal of Physics **12**, 063001 (2010).

[114] P. Palittapongarnpim, A. MacRae, and A. I. Lvovsky, "Note: A monolithic filter cavity for experiments in quantum optics," Review of Scientific Instruments **83**, 066101 (2012).

[115] A. Ahlrichs, C. Berkemeier, B. Sprenger, and O. Benson, "A monolithic polarization-independent frequency-filter system for filtering of photon pairs," Applied Physics Letters **103**, 241110 (2013), https://doi.org/10.1063/1.4846316 .

[116] C. J. Foot et al., Atomic physics, Vol. 7 (Oxford University Press, 2005).

[117] D. A. Steck, "Rubidium 87 d line data," (2001).

[118] R. J. Glauber, "The quantum theory of optical coherence," Phys. Rev. **130**, 2529 (1963).

[119] M. O. Scully and M. S. Zubairy, Quantum Optics (Cambridge University Press, 1997).

[120] P. J. Mosley, J. S. Lundeen, B. J. Smith, and I. A. Walmsley, "Conditional preparation of single photons using parametric downconversion: a recipe for purity," New Journal of Physics **10**, 093011 (2008).

[121] M. Förtsch, J. U. Fürst, C. Wittmann, D. Strekalov, A. Aiello, M. V. Chekhova, C. Silberhorn, G. Leuchs, and C. Marquardt, "A versatile source of single photons for quantum information processing," Nature Communications **4**, 1818 (2013).

[122] R. Loudon, The Quantum theory of Light (New York: Oxford University Press, 1983).

[123] S. Bettelli, "Comment on "coherence measures for heralded single-photon sources"," Phys. Rev. A **81**, 037801 (2010).

[124] S. Fasel, O. Alibart, S. Tanzilli, P. Baldi, A. Beveratos, N. Gisin, and H. Zbinden, "High-quality asynchronous heralded single-photon source at telecom wavelength," New Journal of Physics **6**, 163 (2004).

[125] E. Bocquillon, C. Couteau, M. Razavi, R. Laflamme, and G. Weihs, "Coherence measures for heralded single-photon sources," Phys. Rev. A **79**, 035801 (2009).

[126] F. Wolfgramm, Y. A. de Icaza Astiz, F. A. Beduini, A. Cerè, and M. W. Mitchell, "Atom-resonant heralded single photons by interaction-free measurement," Phys. Rev. Lett. **106**, 053602 (2011).

[127] P. Sekatski, N. Sangouard, F. Bussières, C. Clausen, N. Gisin, and H. Zbinden, "Detector imperfections in photon-pair source characterization," Journal of Physics B: Atomic, Molecular and Optical Physics **45**, 124016 (2012).

[128] V. Prakash, A. Sierant, and M. W. Mitchell, "Autoheterodyne characterization of narrow-band photon pairs," Phys. Rev. Lett. **127**, 043601 (2021).

[129] L. Mandel, "Photon interference and correlation effects produced by independent quantum sources," Phys. Rev. A **28**, 929 (1983).

[130] P. C. Humphreys, B. J. Metcalf, J. B. Spring, M. Moore, X.-M. Jin, M. Barbieri, W. S. Kolthammer, and I. A. Walmsley, "Linear optical quantum computing in a single spatial mode," Phys. Rev. Lett. **111**, 150501 (2013).

[131] A. Rubenok, J. A. Slater, P. Chan, I. Lucio-Martinez, and W. Tittel, "Real-world two-photon interference and proof-of-principle quantum key distribution immune to detector attacks," Phys. Rev. Lett. **111**, 130501 (2013).

[132] B. Bell, S. Kannan, A. McMillan, A. S. Clark, W. J. Wadsworth, and J. G. Rarity, "Multicolor quantum metrology with entangled photons," Phys. Rev. Lett. **111**, 093603 (2013).

[133] M. Liscidini and J. E. Sipe, "Stimulated emission tomography," Phys. Rev. Lett. **111**, 193602 (2013).

[134] T. Jeong and H. S. Moon, "Joint spectral intensity of entangled photon pairs from a warm atomic ensemble via stimulated emission beat interferometry," Opt. Lett. **45**, 2668 (2020).

[135] I. Jizan, B. Bell, L. G. Helt, A. C. Bedoya, C. Xiong, and B. J. Eggleton, "Phase-sensitive tomography of the joint spectral amplitude of photon pair sources," Opt. Lett. **41**, 4803 (2016).

[136] Z. Y. Ou and L. Mandel, "Observation of spatial quantum beating with separated photodetectors," Phys. Rev. Lett. **61**, 54 (1988).

[137] R.-B. Jin and R. Shimizu, "Extended Wiener-Khinchin theorem for quantum spectral analysis," Optica **5**, 93 (2018).

[138] Y. Okawa, F. Omura, Y. Yasutake, and S. Fukatsu, "Photon heterodyning," Opt. Express **25**, 20156 (2017).

[139] M. Scholz, L. Koch, and O. Benson, "Analytical treatment of spectral properties and signal — idler intensity correlations for a double-resonant optical parametric oscillator far below threshold," Optics Communications **282**, 3518 (2009).

[140] N. Maring, D. Lago-Rivera, A. Lenhard, G. Heinze, and H. de Riedmatten, "Quantum frequency conversion of memory-compatible single photons from 606 nm to the telecom c-band," Optica **5**, 507 (2018).

[141] B. Korzh, Q.-Y. Zhao, J. P. Allmaras, S. Frasca, T. M. Autry, E. A. Bersin, A. D. Beyer, R. M. Briggs, B. Bumble, M. Colangelo, G. M. Crouch, A. E. Dane, T. Gerrits, A. E. Lita, F. Marsili, G. Moody, C. Peña, E. Ramirez, J. D. Rezac, N. Sinclair, M. J. Stevens, A. E. Velasco, V. B. Verma, E. E. Wollman, S. Xie, D. Zhu, P. D. Hale, M. Spiropulu, K. L. Silverman, R. P. Mirin, S. W. Nam, A. G. Kozorezov, M. D. Shaw, and K. K. Berggren, "Demonstration of sub-3 ps temporal resolution with a superconducting nanowire single-photon detector," Nature Photonics **14**, 250 (2020).

[142] C. K. Law, I. A. Walmsley, and J. H. Eberly, "Continuous frequency entanglement: Effective finite Hilbert space and entropy control," Phys. Rev. Lett. **84**, 5304 (2000).

[143] A. F. Abouraddy, T. M. Yarnall, and G. Di Giuseppe, "Phase-unlocked Hong-Ou-Mandel interferometry," Phys. Rev. A **87**, 062106 (2013).

[144] P. G. Kwiat and H. Weinfurter, "Embedded Bell-state analysis," Phys. Rev. A **58**, R2623 (1998).